POLITECNICO DI TORINO

Department of Structural, Geotechnical and Building Engineering

Master's Degree Program
Civil Engineering

Master's Degree Thesis

Scouring Effects on Dynamic Response of Caisson Foundations

Politecnico di Torino

Academic Advisors
Prof. Sebastiano Foti
Ph.D. Andrea Ciancimino
Ph.D. Mauro Aimar

Candidate
Marlio Molina Manrique

A / Y 2022-2023

ACKNOWLEDGEMENTS

I would like to express my deep gratitude to the numerous individuals and institutions who have played an invaluable role in the completion of this thesis. This endeavor would not have been possible without their unwavering support, guidance, and contributions.

My deepest appreciation goes to my academic advisor, Professor Sebastiano Foti. Your mentorship, dedication, and extensive knowledge have been indispensable throughout this research journey. Your insightful guidance has steered this work toward its successful completion.

I would also like to acknowledge my co-academic advisors, Dr. Andrea Ciancimino and Dr. Mauro Aimar. Your valuable input, feedback, and collaboration have significantly enriched this research. Your expertise and contributions have been an essential part of this academic endeavor.

My heartfelt thanks go out to my family, and in particular, to my mom, for their unwavering emotional support during these two years. Your encouragement and understanding have been my pillars of strength throughout this challenging journey.

I extend my heartfelt thanks to my colleagues and friends who have been a source of motivation, support, and camaraderie throughout this journey. Your discussions, ideas, and shared experiences have greatly enriched my academic life.

Finally, my gratitude extends to the Ministry of Science, Technology, and Innovation of Colombia for granting me the scholarship that made this experience possible. Your support has been instrumental in my academic journey.

In conclusion, I extend my gratitude to all those who have been part of this academic journey. Your contributions and support have been vital to the attainment of my master's degree.

TABLE OF CONTENTS

LIST OF FIGURES

LIST OF TABLES

ABSTRACT

Caisson foundations play a pivotal role in supporting long-span bridges. Their performance, however, is susceptible to the impacts of scouring, due to the increase in frequency and intensity of flood events related to climate change. To ensure the structural integrity of caisson-supported bridge piers during seismic events, it is crucial to examine the intricate interplay between scouring, the soil-caisson-pier system, and seismic forces.

This thesis presents a comprehensive investigation into the complex relationship between bridge pier caissons, scouring, and seismic behavior. Advanced numerical modeling, employing the OpenSees object-oriented finite element framework, forms the backbone of this study. A specific case study encompasses three scouring scenarios: No Scoured (NS), General Scoured (GS), and Local Scoured (LS). The research delves into deformation, spectral acceleration, and cumulative displacements to shed light on the diverse impacts of local and general scouring.

The caisson foundation is represented by a rigid element, while the pier is modeled using an elastic beam-column element. The compliant soil, characterized as coarse-grained gravelly soil, is simulated under fully drained conditions utilizing an elastic-plastic pressure-dependent multi-yield constitutive law.

The study firstly presents lateral pushover analyses and free vibration studies, revealing that scouring conditions significantly influence the horizontal stiffness and fundamental period of the system. Notably, the NS and GS cases exhibit a symmetrical response, while the LS case presents an asymmetric behavior, due to the morphology of the scour hole.

Dynamic transient analyses, using a variety of input motions, provide further insights into the system's response. The findings demonstrate higher cumulative displacements in scoured cases, with the LS scenario displaying distinctive trends of deck movement and caisson rotation towards the most scoured direction.

The acceleration patterns observed at the deck are intriguing and exhibit interesting trends. It increases with both input motion spectral acceleration at the pier's fundamental period, $S_e(T_{0,pier})$, and Arias Intensity (AI). Furthermore, the deck acceleration in the NS case was higher compared with the GS and LS cases, an effect attributed to a possible seismic isolation effect of scouring and soil non-linearities, clearly more pronounced in the GS case when strong ground motions were employed.

Settlement dynamics during seismic loading primarily result from soil densification, with the GS case showing higher settlements due to the lower overburden pressure in the compliant soil.

The study underscores the need for a holistic approach to design and assess bridge pier caisson-soil systems, considering various factors, such as scouring, ground motion, and soil behavior. Importantly, this research, albeit preliminary, enhances our understanding of how general and local scouring impacts the seismic behavior of caisson foundations, offering valuable insights for robust engineering practices and design considerations for critical infrastructure.

Continued research is encouraged, encompassing alternative scenarios of scour morphologies and a greater variety of input motions to further inform the design and assessment of caisson-supported structures in the face of evolving environmental and seismic challenges.

CHAPTER 1

INTRODUCTION

According to the performance-based design framework, the assessment of the seismic performance of a structure can be performed by comparing specific threshold values of earthquake-induced displacements or rotations to those attained during and at the end of the seismic event (Gaudio & Rampello, 2016). In the case of a bridge, its performance must be evaluated from the hydraulic, structural and geotechnical points of view (Ciancimino et al., 2022a) and its stability and functionality, which can evolve during the service life because of either structural damage or ageing and change in the supporting conditions, must be guaranteed (Alampalli & Ettouney, 2008b).

Among the factors that affect the supporting conditions of bridge piers, scouring stands out as the primary cause of bridge failures in the United States, accounting for approximately half of these failures (Klinga & Alipour, 2015). Therefore, its study and monitoring are of paramount importance, especially in cases where the magnitude of scouring cannot be defined a priori because the scour hole has been filled with less resistant infill materials, which compromise the structural integrity of the foundation system (Foti & Sabia, 2011).

The hydraulic processes responsible for foundation scour are nowadays well understood in the aftermath of flood events (Chiew, 1992). Several experimental and numerical studies have been conducted to enhance the design of foundation shapes, such as skirted caissons, with the aim of preventing scouring phenomena (Wei et al., 2022) and identifying the most efficient cross-sections for reducing local scour (Tariq et al., 2022). However, the detrimental effects on the mechanical performance and failure mechanisms of scoured foundations have not yet been fully investigated (Ciancimino et al., 2022a)

Caisson foundations are typically adopted for long-span bridges in seismic areas, where high horizontal forces are expected (Gaudio & Rampello, 2021). Because of this, it is important to study the effects of scouring on the mechanical performance of these critical infrastructures, under either static or dynamic conditions. Nowadays, in the state of practice, this assessment is commonly performed through numerical analyses (Wang et al., 2014a), including simplified lumped-parameter models (e.g., Klinga & Alipour, 2015) and finite element models (e.g., Ciancimino et al., 2022a & Occelli, 2004).

However, studies using physical modeling or centrifuge tests (e.g., Ciancimino et al., 2022b) and in-situ seismic or pseudo-dynamic tests on exiting pier-caisson systems (Chang et al., 2014), combined with numerical models, have been carried out to assess the effects of scouring on caisson foundations. All of them confirm the detrimental or positive effects that scouring can

have on the seismic response of the structure, depending on the scouring morphology and magnitude (Chortis et al., 2020).

Scouring on caisson foundations leads to a significant reduction in the bearing and lateral capacity of the footing due to the loss of the surrounding compliant soil (Lin et al., 2012). It also results in the accumulation of permanent settlements and rotations after seismic shaking (Ciancimino et al., 2022a). However, these effects vary depending on factors such as the type, shape, and depth of the scour hole (Chortis et al., 2020) and the overconsolidation characteristics of the remaining soil (Qi et al., 2016). Experimental studies conducted by Ciancimino et al. (2022b); & Qi et al. (2016) have demonstrated that the effects of general and local scouring are notably different. In general, general scouring affects both sidewall and base resistance mechanisms, while local scouring exhibits strong axial asymmetry and primarily affects sidewall resistance. The morphology of the scour hole is particularly relevant in the context of local scouring.

This study is dedicated to the assessment of seismic response in a specific case study. It employs dynamic analysis via the OpenSees finite element framework, incorporating real ground motion records. The primary objective is to investigate and provide new insights into the complex interplay between the pier, caisson foundation, and soil under three distinct conditions: unscoured, locally scoured, and generally scoured. The study seeks to assess the resulting impact on pier behavior and response.

Firstly, a brief review of the current state of the art (Chapter 2) and an introduction to the case study (Chapter 3) are provided. Secondly, the OpenSees object-oriented finite element framework (Chapter 4) and the elastic-plastic multi yield pressure-dependent (PDMY) soil constitutive law (*Chapter 5*), which is used to account for soil nonlinearity in the soil-caisson-structure interaction (as discussed in Klinga & Alipour, 2015) are introduced. Thirdly, a validation stage against literature results of the PDMY model is performed and presented, including all the components of the soil model (i.e., the Joyner & Chen, 1975 approach, Rayleigh damping, and CFL condition), in Chapter 6. Fourthly, the full soil-structure model, including a simple rigid-link procedure to simulate the soil-structure interface, is presented in Chapter 7. Lastly, the results of the dynamic analyses are presented and discussed in Chapter 8.

The main results of this research underscore the critical influence of scouring conditions on the seismic performance of bridge pier caisson foundations, with notable distinctions between local and general scouring. The lateral pushover and free vibration analyses demonstrate that scouring significantly alters the system's horizontal stiffness and fundamental period. The dynamic transient analyses using input motions reveal a distinct response for unscoured, locally scoured, and generally scoured scenarios, with cumulative displacements notably higher in scoured cases. The study confirms an isolation effect of scouring, consistently resulting in lower deck accelerations, a phenomenon well-documented in the literature. Settlement dynamics during seismic loading predominantly results from soil densification, with general scouring causing higher settlements due to reduced overburden pressure in the compliant soil. These findings emphasize the need for a holistic approach to design and assess bridge pier caisson-soil systems, considering various factors such as scouring, ground motion characteristics, and soil behavior, ultimately contributing to robust engineering practices and design considerations for critical infrastructure.

CHAPTER 2

STATE OF THE ART

Defining soil-structure interaction (SSI) or structure-soil-structure interaction (SSSI) is challenging due to its intricate nature and the multifaceted problems inherent in its theory. This complexity encompasses the soil response to external dynamic or static loading, the propagation of ground-borne vibrations induced by earthquakes or other sources, and the static and dynamic stiffness of foundations embedded in compliant soil. Kinematic and inertial interactions between the soil and supported structures further contribute to the intricate nature of SSI (Kausel, 2010). As eloquently expressed by Lou et al. (2011):

> "*SSSI is an interdisciplinary field of endeavor, which lies at the intersection of soil and structural mechanics, soil and structural dynamics, earthquake engineering, geophysics and geomechanics, material science, computational and numerical methods, and diverse other technical disciplines*".

In the seismic context, SSI has been found to significantly amplify seismic actions in structures, particularly when considering the depth of embedded foundations, in comparison with a fixed-base structure (e.g., El Hoseny et al., 2023). Traditional SSI analyses often treat shallow footings or embedded foundations as massless in coupled analyses (e.g., Gazetas, 1991) due to their relatively small mass compared to the superstructure. However, when studying caisson foundations, this assumption may not hold true. Caisson foundations supporting piers are massive embedded substructures, and their inertial contribution plays a crucial role in understanding the response of the coupled soil-caisson-pier system. Therefore, both the kinematic interaction with compliant soil and the inertial interaction of both substructure and superstructure must be considered (e.g., Tsigginos et al., 2008), especially when the compliant soil is under scoured conditions.

The subsequent sections of this chapter provide a concise review of SSI history, analysis approaches for coupled SSI, with a particular focus on the significance of SSI in understanding caisson foundation responses. Additionally, the current state of the art regarding scouring effects on foundations is introduced.

2.1. Addressing the soil-structure interaction history

Origins of soil-structure interaction (SSI) can be traced back to the late 19th century with the study of elastoplastic. Some important authors that contributed with the development of analytical solutions were the mathematicians Gabriel Lamé, and Émile Clapeyron who addressed the elastic half-space problem, which solutions for static and time-varying concentrated forces were given later by William Thomson (also known as Lord Kelvin) and

Gabriel Stokes, respectively, being the Stokes solution today a cornerstone not only in the SSI but also in other fields, such as geophysics and acoustics (Kausel, 2010).

Moving onto the contemporary era, the SSI development have been marked by the triumphal entry of powerfull digital computers together with versatile numerical methods (i.e., finite element methods – FEM) which change radically the research paradigm previously focused on purely analytical methods (Kausel, 2010). However, because of the computational demands of direct approaches (i.e., FEM), researchers have been moving forward simpler and reliable methods that make easier the design approaches (de Klerk et al., 2008; Lesgidis et al., 2015, 2018).

2.2. Available analysis approaches for coupled soil-structure interaction

Unlike the static analysis, in the dynamic analysis the coupled soil-structure system is subjected to time-varying excitation generating accelerations which give rise to inertia forces. As a consequence, both the stiffness and mass distribution of the system in addition to the load characteristics affect the dynamic response of the system (Andersson, 2021). Because of this, during earthquake shaking or any other dynamic loading (e.g., ocean waves, vehicles movement, etc.), foundation response depends on the nature and deformability of the supporting ground, the geometry and inertia of both the foundation and superstructure, and the nature of the dynamic excitation (Gazetas, 1991b).

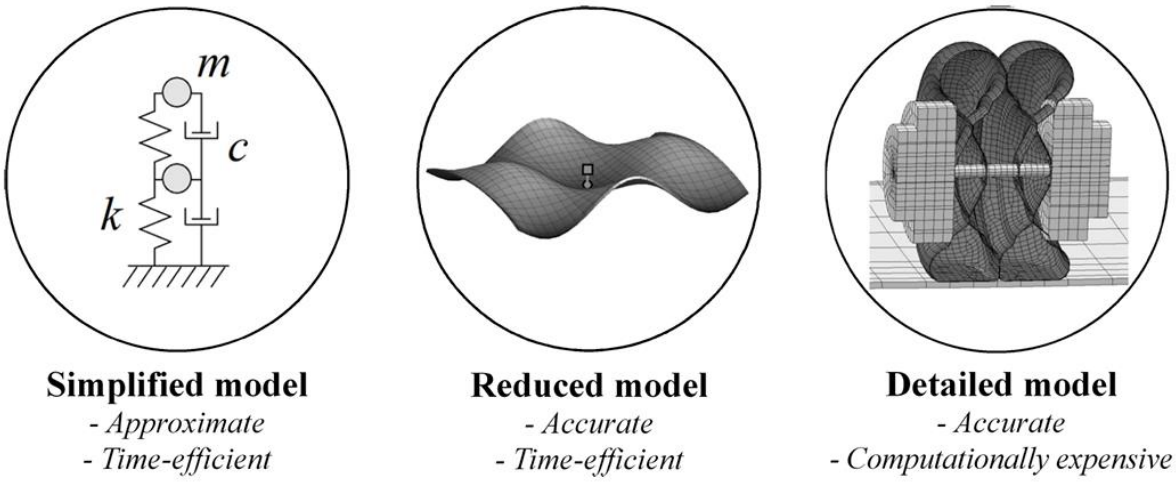

Figure 1. Principal differences between various models (taken from Andersson, 2021)

Looking at the literature, the methods currently available and more commonly used for dynamic soil-structure interaction analysis in the time domain can be classified into three groups (*Figure 1*): simplified modeling (i.e., lumped-parameter models), reduced modeling (i.e., modified-Newmark and macro-element formulations) and detailed modeling (i.e., 3D FEM direct nonlinear or substructure linear approaches) (Gaudio & Rampello, 2021). The one to choose will depend on the requested accuracy of the outputs (mostly dependent on the importance of the structure and the consequences of its loss of functionality) and available computational resources (Andersson, 2021).

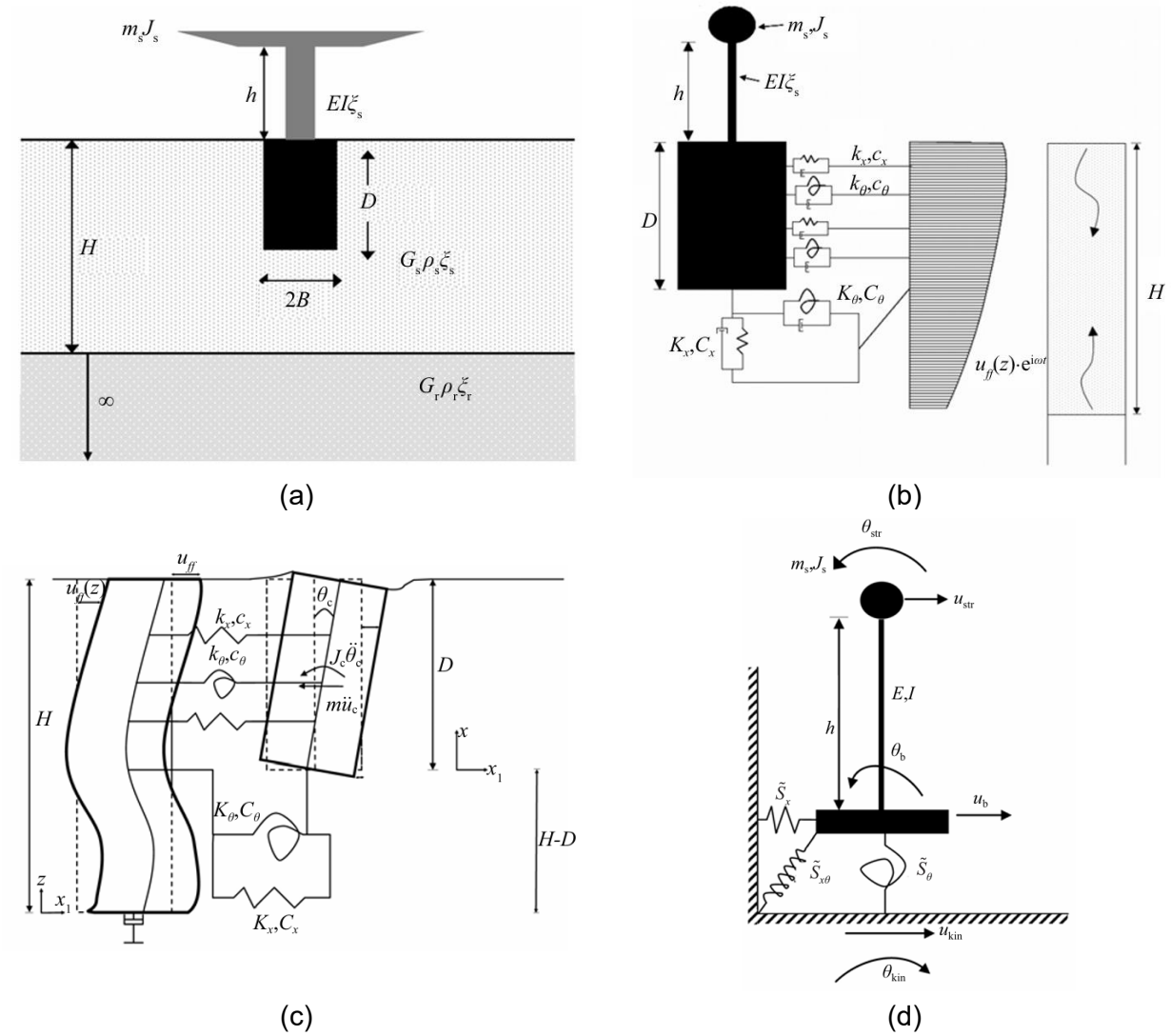

Figure 2. Winkler multi-spring-and-dashpot model; (a) bridge caisson-soil system; (b) proposed model; (c) kinematic interaction model; (d) inertial interaction model (taken from Tsigginos et al., 2008)

2.2.1. Simplified Models

Simplified models or lumped-parameter models mimic the soil-structure interaction through both nonlinear and linear springs, and viscous dashpots located at the base of the superstructure. In this way, the soil-foundation compliance is reproduced via dynamic impedance functions (Gaudio & Rampello, 2021).

The accuracy of lumped-parameters models in predicting the seismic response of bridge piers supported on piles have been assessed through several studies, using springs and dashpots of different complexity (Lesgidis et al., 2015; González et al., 2019). Although the results of these parametric studies have demonstrated a good degree of confidence when are compared with finite element (FE) analysis (Sextos et al., 2003; Sieber et al., 2020), some issues have been found regarding to the excitation frequency dependency of the impedance functions (Gaudio & Rampello, 2021).

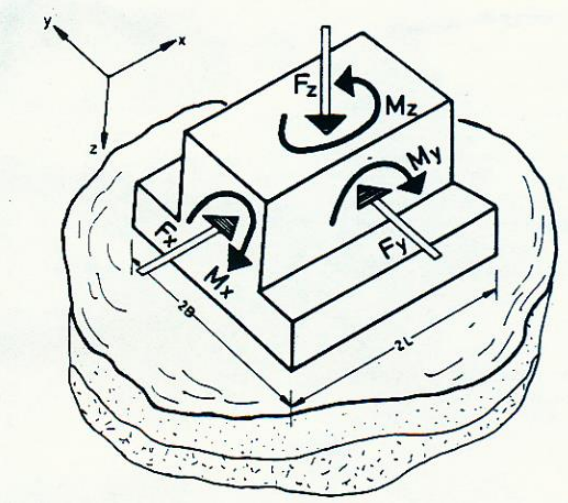

Figure 3. Rigid-massless foundation block with its six degrees of freedom (taken from Gazetas, 1991)

Table 1. Dynamic Stiffnesses and Dashpot Coefficients for Surface Foundations on Homogeneous Stratum Over Bedrock (taken from Gazetas, 1991)

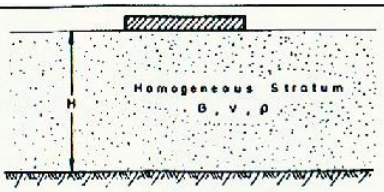

Foundation Shape		*Circular Foundation of Radius* $B = R$	*Rectangular Foundation* $2B$ *by* $2L$ $(L > B)$	*Strip Foundation* $2L \to \infty$
Static stiffnesses, K	Vertical, z	$K_z = \frac{4GR}{1-\nu}\left(1 + 1.3\frac{R}{H}\right)$	$K_z = \frac{2GL}{1-\nu}\left[0.73 + 1.54\left(\frac{B}{L}\right)^{3/4}\right]\left(1 + \frac{\frac{B}{H}}{0.5 + \frac{B}{L}}\right)$	$\frac{K_z}{2L} \simeq \frac{0.73G}{1-\nu}\left(1 + 3.5\frac{B}{H}\right)$
	Lateral, y	$K_y = \frac{8GR}{2-\nu}\left(1 + 0.5\frac{R}{H}\right)$	.	$\frac{K_y}{2L} \simeq \frac{2G}{2-\nu}\left(1 + 2\frac{B}{H}\right)$
	Lateral, x	$K_x = K_y$	.	—
	Rocking, rx	$K_{rx} = \frac{8GR}{3(1-\nu)}\left(1 + 0.17\frac{R}{H}\right)$	.	$\frac{K_{rx}}{2L} = \frac{\pi GB^2}{2(1-\nu)}\left(1 + 0.2\frac{B}{H}\right)$
	Rocking, ry	$K_{ry} = K_{rx}$	.	—
	Torsional, t	$K_t = \frac{16}{3}GR^3\left(1 + 0.10\frac{R}{H}\right)$	.	—
Dynamic stiffness coefficients, $k(\omega)$	Vertical, z	$k_z = k_z(H/R, a_0)$ is obtained from Graph III-1	$k_z = k_z(H/B, L/B, a_0)$ is plotted in Graph III-2 for rectangles and strip	
	Horizontal, y or x	$k_y = k_y(H/R, a_0)$ is obtained from Graph III-1	.	$k_y = k_y(H/B, a_0)$ is obtained from Graph III-3
	Rocking, rx or ry Torsional	$k_\alpha(H/R) \simeq k_\alpha(\infty)$ $\alpha = rx, ry, t$	.	$k_{rx}(H/R) \simeq k_{rx}(\infty)$
Radiation dashpot coefficients, $C(\omega)$	Vertical, z	$C_z(H/B) \simeq 0$ at frequencies $f < f_c$, regardless of foundation shape $C_z(H/B) \simeq 0.8C_z(\infty)$ at $f \geq 1.5f_c$ At intermediate frequencies: interpolate linearly. $f_c = \frac{V_{Le}}{4H}$, $V_{Le} = \frac{3.4V_s}{\pi(1-\nu)}$		
	Lateral, y or x	$C_y(H/B) \simeq 0$ at $f < \frac{1}{3}f_s$; $C_y(H/B) \simeq C_y(\infty)$ at $f > \frac{1}{3}f_s$ At intermediate frequencies: interpolate linearly. $f_s = V_s/4H$. Similarly for C_x		
	Rocking, rx or ry	$C_{rx}(H/B) \simeq 0$ at $f < f_c$; $C_{rx}(H/B) \simeq C_{rx}(\infty)$ at $f > f_c$. Similarly for C_{ry}		
	Torsional, t	$C_t(H/B) \simeq C_t(\infty)$		

Table 2. Dynamic Stiffnesses and Dashpot Coefficients for Foundations Embedded in Homogeneous Stratum Over Bedrock (taken from Gazetas, 1991)

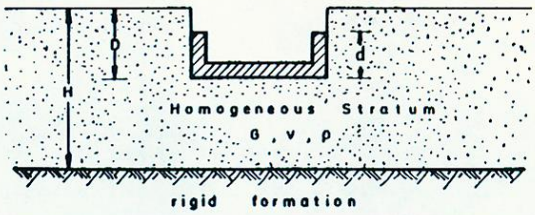

Foundation Shape		Circular Foundation of Radius R	Strip Foundation
Static stiffnesses, K	Vertical	$K_{z,emb} \simeq K_{z,sur}\left(1+0.55\frac{d}{R}\right)\left[1+\left(0.85-0.28\frac{D}{R}\right)\frac{D}{H-D}\right]^{\dagger}$	$K_{z,emb} \simeq K_{z,sur}\left[1+0.2\left(\frac{d}{B}\right)^{2/3}\right]\left(1+3.5\frac{B}{H-D}\right)$
	Horizontal, y or x	$K_{y,emb} \simeq K_{y,sur}\left(1+\frac{d}{R}\right)\left(1+1.25\frac{D}{H}\right)^{\dagger}$	$K_{y,emb} \simeq K_{y,sur}\left(1+0.5\frac{d}{B}\right)\left(1+1.5\frac{D}{H}\right)$
	Rocking, rx or ry	$K_{rx,emb} \simeq K_{rx,sur}\left(1+2\frac{d}{R}\right)\left(1+0.65\frac{D}{H}\right)$	$K_{rx,emb} \simeq K_{rx,sur}\left(1+\frac{d}{B}\right)\left(1+0.65\frac{D}{H}\right)$
	Coupled swaying–rocking	$K_{yrx,emb} \simeq \frac{1}{2}dK_{y,emb}$	$K_{yrx,emb} \simeq \frac{1}{2}dK_{y,emb}$
	Torsional	$K_{t,emb} \simeq K_{t,sur}\left(1+2.67\frac{d}{R}\right)$	—
Dynamic stiffness coefficients, $k(\omega)$		The relationships between k_{emb} and k_{sur} follow approximately the same pattern as those between embedded and surface foundation on a homogeneous halfspace. Therefore, use the results of Table 15.2 as a first approximation.	
Radiation dashpot coefficients, $C(\omega)$		C_{emb} exceeds C_{sur} by an amount that depends on the geometry of the sidewall–soil contact surface and is practically independent of the presence or absence of a rigid base at shallow depths. Therefore, use the results of Table 15.2, but with C_{sur} corresponding to the layered profile and thus obtained according to Table 15.3 (approximate guideline).	

* Sources are listed in the text.
† $K_{z,sur}$, $K_{y,sur}$, ... are the stiffnesses for the corresponding surface foundations, and can be obtained from Table 15.3.

In the case of bridge piers on rigid caisson foundations, Tsigginos et al., (2008) proposed a dynamic Winkler multi-spring-and-dashpot model (*Figure 2*), using the solutions provided by (Assimaki, 1998; Chatzigiannelis, 1999; Gerolymos & Gazetas, 2006), to study the seismic response of these type of bridge caisson-soil systems. Comparison with FE analysis and other available solutions demonstrated the reliability of the model. An important finding of this study was the increase of the fundamental period and damping ratio of the structure due to soil-structure interaction.

2.2.1.1. Gazetas solution

In 1991, Professor *George Gazetas* introduced an engineering procedure for estimating both static and dynamic springs and dashpot coefficients of flexibly-supported foundations, The method relies on straightforward algebraic formulas and dimensionless charts, assuming an elastic isotropic infinite half-space for either infinite or finite depth. It was designed to be applicable to various foundation types, including surface shallow foundations, embedded foundations, and piles. The approach builds upon the prior work of Gazetas & Tassoulas (1987a, 1987b) and Gazetas, 1991a).

Figure 3 displays a rigid-massless block with its six degrees of freedom, considered in the Gazetas (1991) solution. *Table 1 & Table 2* show the solutions for surface and embedded

foundations in homogeneous stratum over bedrock, respectively. Notice that the solutions for embedded foundations are linked to the surface foundation solutions, and unlike the uncoupled vertical and tortional stiffnesses, the horizontal and rocking stiffnesses are coupled (Gazetas, 1991b).

In addition, in his work, *Gazetas* shows how to estimate the soil parameters to compute the spring and dashpot coefficients from field geotechnical tests.

2.2.2. Advanced reduced-order models

Because of the high computation demand of 3D nonlinear FE analysis, advanced reduced-order models have been proposed as an alternative, using for instance Modified-Newmark (Gorini & Callisto, 2019) and Macro-Element formulations (Lesgidis et al., 2018) or dynamic substructuring (Andersson, 2021) to model coupled soil-structure dynamic systems. However, most of these approaches have been developed either for shallow (e.g., Nova & Montrasio, 1991) or pile foundations (Varun, 2010), where the foundation inertial forces are typically neglected (*Figure 4*). Instead, these forces should be considered for caisson foundations, being much more massive and rigid than the surrounding foundation soil (Gaudio & Rampello, 2020). Remarkably, there has been limited research specifically tailored to caisson foundations (Gaudio & Rampello, 2021).

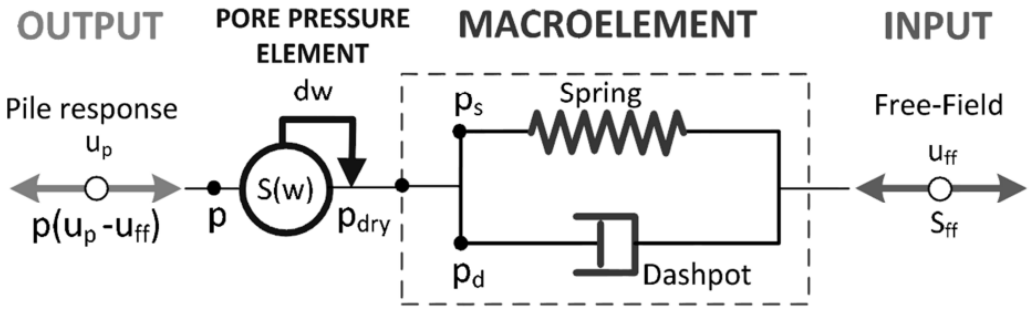

Figure 4. Macro-element formulation for pile foundations in liquefiable soils (taken from Varun, 2010)

2.2.2.1. Substructure approach

Prior to introduce the substructure approach, it is important to understand what kinematic and inertial interaction are in the context of SSI. The first, delineates the disparity in structural response when subjected to free-field ground motion, both in the absence and presence of the scattering effect induced by the structure. This phenomenon's magnitude is contingent upon various factors, including the structure's geometry, foundation size and embedment, the kinematics of the incident free-field motion, and the angle of incidence of seismic waves (Kotronis et al., 2013). On the other hand, the latter, delves into the response of the entire soil–foundation–structure system to the excitation induced by D'Alembert forces, associated with the acceleration of the superstructure due to kinematic interaction (Mylonakis et al., 2006).

The substructure approach, commonly known as the indirect method, is extensively employed for assessing the seismic performance of structures supported by caisson foundations, owing to its simplicity and computational efficiency (e.g., Conti & Di Laora, 2022). Within this framework, reduced-order modeling assumes a pivotal role, as highlighted by Andersson, 2021.

In this approach, the intricate SSI problem (*Figure 5a*) is simplified by breaking down the superstructure-foundation-soil system into two subsystems (*Figure 5b*). The response of each subsystem is then independently determined, focusing on the kinematic and inertial effects of the soil-structure interaction problem, typically in the frequency domain. Subsequently, the superposition theorem is applied to combine these responses and obtain the overall system response (Mylonakis et al., 2006).

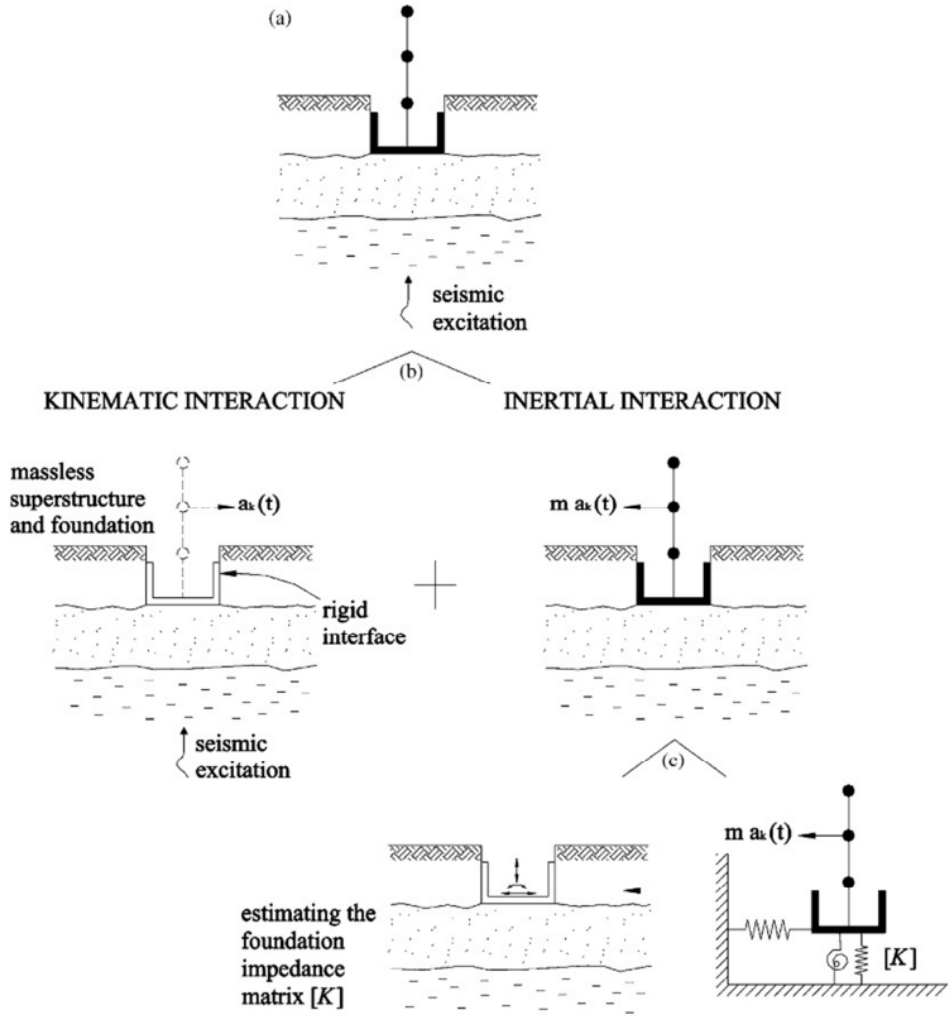

Figure 5. Substructure approach; (a) superstructure-foundation-soil system, (b) decomposition of the system into kinematic and inertial response, (c) two-step analysis of inertial interaction (taken from Mylonakis et al., 2006)

This approach allows to easily account for the majority of peculiar aspects of dynamic soil-structure interaction, such as the increase of fundamental period and damping ratio of the compliant-base system with respect to the fixed-base system and of kinematic interaction effects (Gaudio & Rampello, 2021).

However, it is crucial to note that this approach is limited to linear or linear-equivalent problems (Kotronis et al., 2013). Consequently, the assessment of permanent displacements is not feasible within this framework (Gaudio & Rampello, 2021). Nevertheless, it serves as a reasonable engineering approximation in scenarios where the soil response exhibits moderate non-linearity (e.g., Mylonakis et al., 1997).

2.2.3. Numerical Methods

Numerical methods, also named direct approach, both the soil volume and the structure are incorporated into a unified model (*Figure 6*), which is analyzed in a single step through one of several numerical discretization techniques such as the Finite Element Method, Spectral Element Method, Finite Difference Method, etc (Kotronis et al., 2013). This approach remains valid for both linear and nonlinear analyses, allowing for the implementation of complex constitutive laws (Gaudio & Rampello, 2016).

The 3D FE analysis have been useful to perform parametric studies and evaluate the effect of soil plasticity (Zafeirakos & Gerolymos, 2013; Gaudio & Rampello, 2019), geometry of the structure (that is pier height, embedded depth and diameters of the caisson), as well as its mass (Veletsos, 1977; Tsigginos et al., 2008). Most of these studies have been performed aiming at not only studying the soil-structure interaction phenomena but also developing simpler approaches, less time-consuming, for analyzing and design bride pier-caisson-soil systems (Tsigginos et al., 2008).

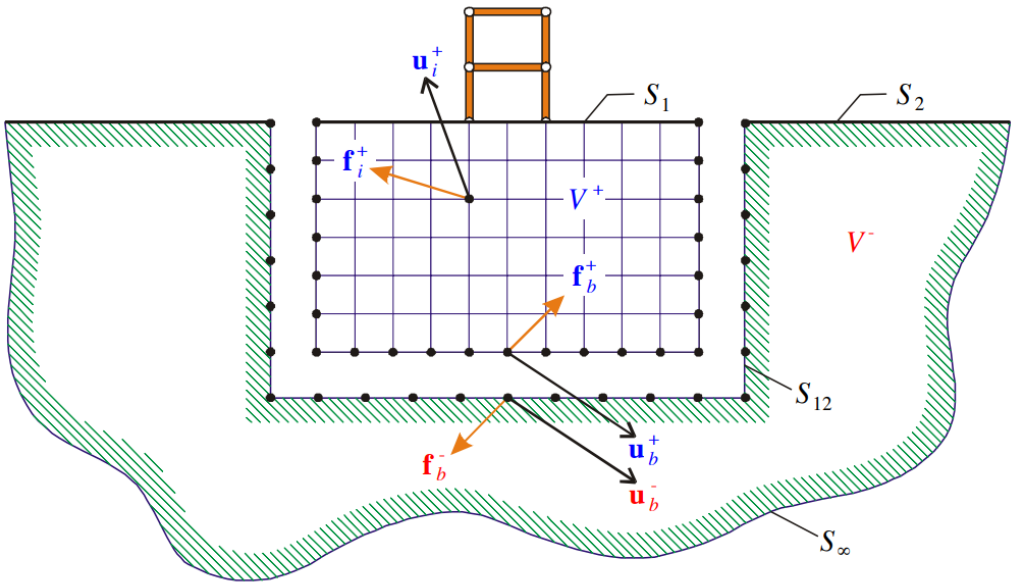

Figure 6. Direct approach and boundary conditions imposed along the artificial borders of the model to simulate the radiation of energy in a deformable, unbounded continuum (taken from Andersen, 2004)

Notably, the direct method enables the consideration of geometric nonlinearities, encompassing phenomena such as foundation uplift and gaps forming at the soil-pile shaft interface, under both static and dynamic loading conditions. However, it's important to highlight that the level of detail incorporated into the model, including these geometric nonlinearities, significantly influences the computational demand of the direct approach. Factors such as model size, the complexity of constitutive laws describing dynamic responses in soils and structural elements, the type of kinematic boundary conditions at the soil-structure interfaces, and whether the analysis is conducted under drained or undrained conditions in saturated soils all contribute to increase the overall computational demand (Kotronis et al., 2013).

2.3. Effects of scouring on pier-caisson-soil systems

Nowadays, the detrimental effects of scouring on the performance of bridge piers are well-recognized (Alampalli & Ettouney, 2008a). Nevertheless, the effects of local and general scour are notably different. This has been demonstrated through both experimental (e.g., Ciancimino et al., 2022b & Qi et al., 2016) and numerical (e.g., Ciancimino et al., 2022a) studies.

Lin et al. (2012) conducted a thorough investigation into the impact of scouring on the performance of bridge piers supported by caisson foundations during natural hazards such as severe storms or typhoons. Their study analyzed the collective influence of river flow velocity, water level, and scouring depth on both the overturning stability (*Figure 7a*) and bearing capacity (*Figure 7b*) of caisson foundations. Notably, *Figure 8* illustrates that during extreme flooding events, the adverse effects of scouring are more pronounced in the overturning stability aspect compared to the bearing capacity. These findings are instrumental in the development of warning systems and decision-making processes concerning bridge closures during periods of heavy rainfall or typhoons.

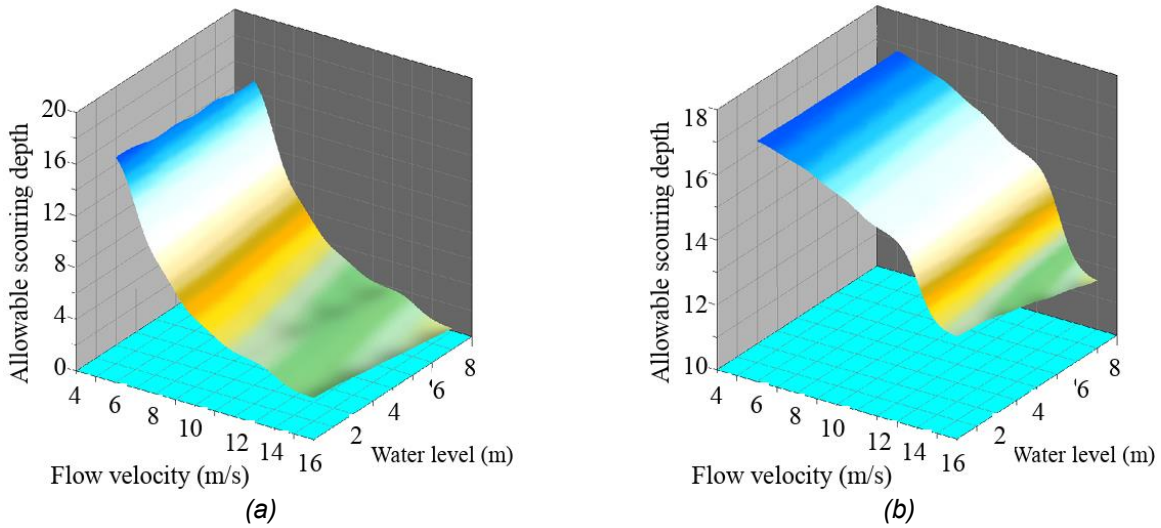

Figure 7. Failure envelopes for combined effects of flow velocity, water level and scour depth; (a) overturning stability and (b) bearing capacity (taken from Lin et al., 2012)

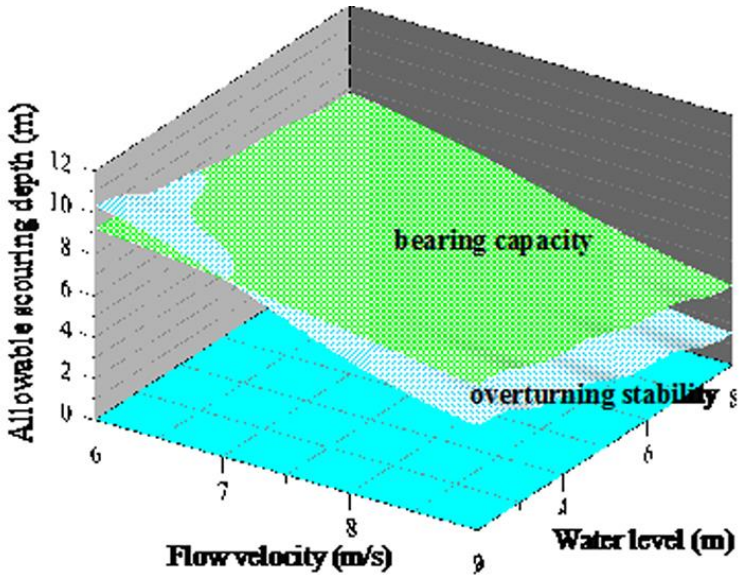

Figure 8. Failure envelope of overturning stability vs bearing capacity for scoured caisson foundations (taken from Lin et al., 2012)

However, regarding the seismic performance of scoured bridges, most of the studies have been devoted to pile foundations (e.g., Linga& Alipour, 2015; Wang et al., 2014b), using mainly lumped-parameter models where scouring is modeled via removing progressively the p-y, t-z and q-z springs. These studies have shown that the foundation type has a great impact on the seismic response of scoured foundations (Wang et al., 2014b) as well as that effects of scouring can be detrimental or not depending on the case study. For instance, Klinga & Alipour (2015) and Wang et al. (2014b) found that scouring can have an isolation effect on the foundation systems, that is the degradation of the support conditions results in a decrease in the shear force acting on the pier. In any case, the scour process decreases the lateral and rocking foundation stiffness.

The reduction in the seismic demand (isolation effect) due to the scouring can be explained also because of the increase of the fundamental period of the structure (mainly the first vibration modes are affected) with scour depth, but again the studies highlight that the relationship between period and scour depth is sensitive to the foundation type (Wang et al., 2014a).

Chang et al., (2014) investigated the seismic performance of existing bridge piers supported on caisson foundations. The in-situ pseudo-dynamic tests revealed that scouring can have a positive effect on lowering the shear force introduced to the column but also a negative effect on increasing the displacement demand on the structure depending on the ground motion characteristics.

Regarding to scouring effect on pier-caisson-soil systems, Ciancimino et al., (2022a) performed numerical simulations to analyze the effects of local and general scour via lateral and vertical pushover tests. The results provided new insights into the influence of foundation scour on the failure mechanisms developing in the surrounding soil. In this study, general scour has been shown to have a detrimental effect on both base and sidewall resistance mechanisms. Conversely, local scour just affects the latter, being strongly asymmetric because of the scour hole morphology.

CHAPTER 3

CASE STUDY

The case study consists of assessing the effect of scouring on the seismic response of a bridge pier supported on a caisson foundation (*Figure 9)* which is affected by both general and local scouring (*Figure 10*). The structural system is composed by the pier and the caisson foundation, both made of reinforced concrete. The whole system is loaded by the self-weight of two girder bridge spans with the deck composed of simply supported, isostatic, reinforced concrete beams which have a mass (M_{deck}) equal to *1440 t*.

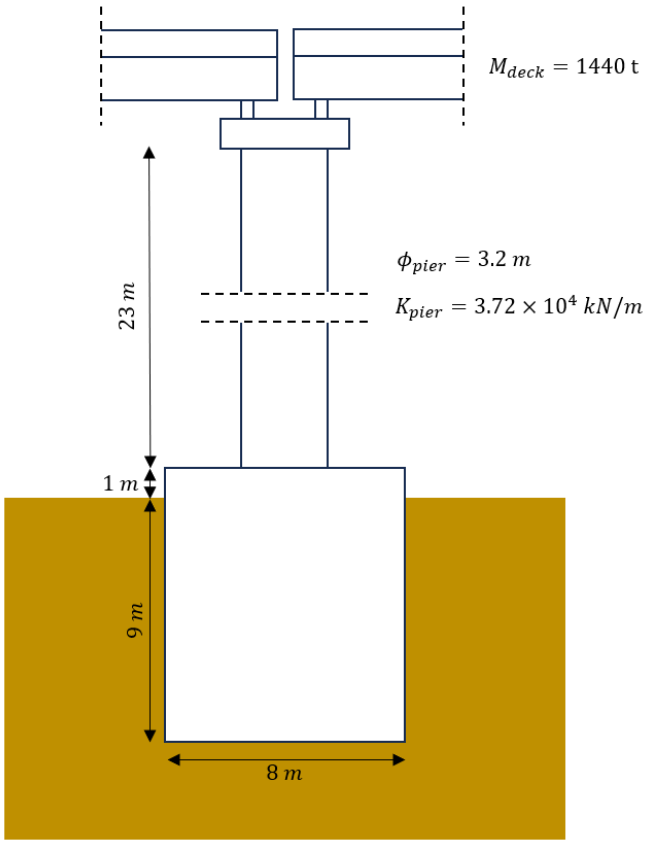

Figure 9. Unscoured foundation – Geometry and structural parameters of the case study

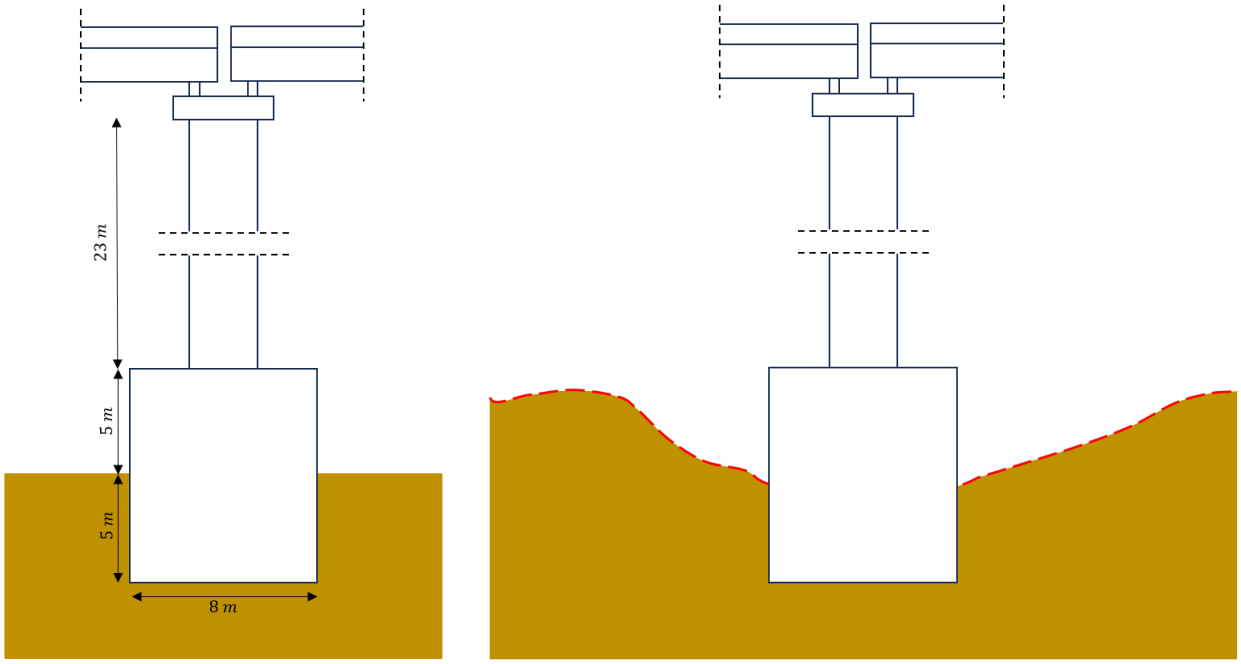

Figure 10. Scoured foundation. (a) General scouring; (b) Local scouring

The pier height (h_{pier}) is 23 m, with a circular diameter (ϕ_{pier}) equal to *3.2 m* and stiffness (K_{pier}) equal to *3.72X10^4 kN/m* (*Figure 9*). The caisson foundation height ($h_{caisson}$) is *10 m*, with a circular diameter ($\phi_{caisson}$) equal to *8 m*. Because of the huge caisson diameter ($\phi_{caisson}$) and small $h_{caisson}/\phi_{caisson}$ ratio ($= 1.25$), the caisson is assumed as infinity rigid ($K_{pier} \to \infty$).

Because the deck is assumed to be simply supported, the kinematic interaction between the deck and the pier is not explicitly considered, and the deck is simply schematized as a concentrated mass.

The caisson is founded on a soil labeled as Messina Gravels (MG) found underwater the Messina Strait. These gravels are characterized by medium relative density $D_R[\%] = 45$, void ratio $e = 0.35$, Poisson ratio $\nu = 0.2$, unit weight $\gamma = 22\ kN/m^3$ and hydraulic conductivity (k) in the order of $10^{-4}\ m/s$. The soil mechanical behavior is modeled with a pressure-dependent elastic-plastic multi-surface yielding model (PDMY Model) to account for the non-linear behavior during cyclic loading and the depth-dependent change in stiffness, typical in coarse grained soils (Mazzoni et al., 2006; Zhu, 2023). The input parameters adopted come from a calibration process performed by *Gorini (2017)* to a set of data coming from different geotechnical explorations carried out underwater the Messina Strait (e.g., Crova et al., 1993; Jamiolkowski & Lo Presti, 2002; Fioravante et al., 2012).

Three scenarios are investigated in this analysis. Firstly, the original configuration of the caisson foundation is considered, labeled as 'no scoured', with an assumed embedment depth (d) of *9.0 m* (*Figure 9*). Secondly, the caisson is subjected to general scouring, involving the removal of a *5.0 m* thick soil layer from the compliant soil, resulting in $d = 5\ m$ (*Figure 10a*). Lastly, the

caisson is influenced by local scouring (*Figure 10b*), utilizing the specific local scoured shape determined though scaled hydraulic *1g* physical modeling of the scouring phenomena conducted by Ciancimino, 2021 (*Figure 11*).

The input motions for the transient dynamic analyses have been processed and scaled by Aimar, (2018). A total of three ground motion records have been selected, as detailed in *Table 3*, and are consistent with the seismic hazard of Urbino, an Italian locality characterized by medium-seismicity. *Figure 12* to *Figure 14* display the chosen acceleration time histories, while *Figure 15* presents their corresponding response spectra.

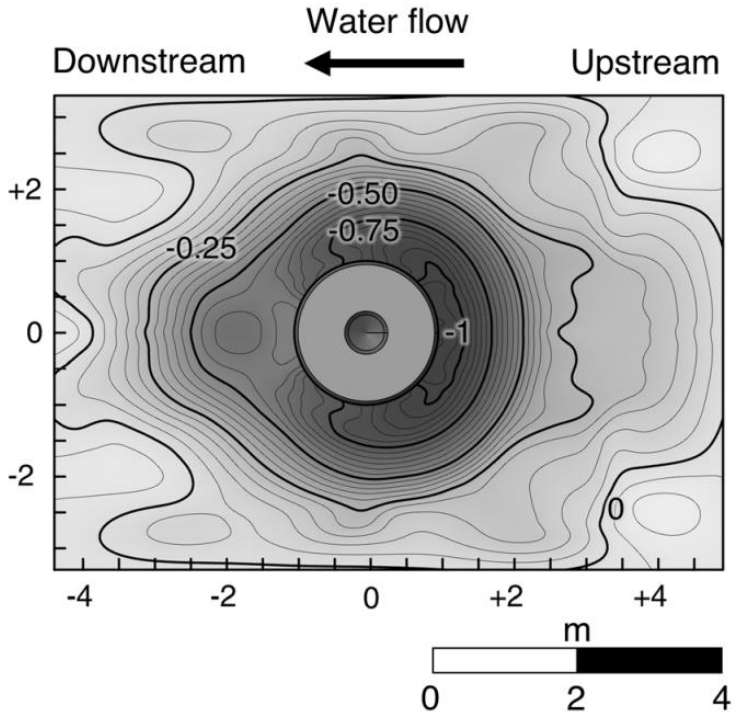

Figure 11. Morphology of the local scour hole (in prototype scale) obtained through 1 g physical modeling (taken from Ciancimino et al., 2022a)

Table 3. Selected Input Motions to use in the Dynamic Analyses

Event name	***Date***	***Network-Station***	***Component***	***Database***	***M_w***	***f_p***	***PGA [g]***	***AI [m/s]***
Central Italy	*26/10/2016*	*IT-CLO*	*EW*	*ITACA*	*5.9*	*8.33*	*0.23*	*0.38*
Northridge-01	*17/01/1994*	*CGS-Vasquez Rocks Park*	*0°*	*PEER NGA-WEST2*	*6.69*	*2.64*	*0.16*	*0.41*
Cosenza	*25/10/2012*	*IT-MRM*	*EW*	*ITACA*	*5.2*	*3.85*	*0.27*	*0.21*

M_w : earthquake magnitude
f_p : predominant frequency [Hz]
PGA : peak ground acceleration [g]
AI : Arias Intensity [m/s]

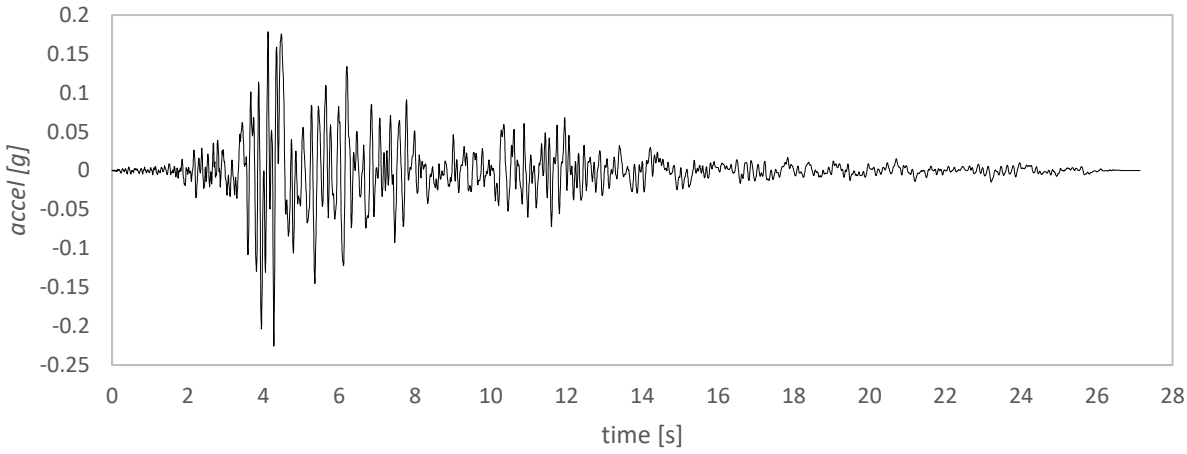

Figure 12. Central Italy – EW acceleration time-history

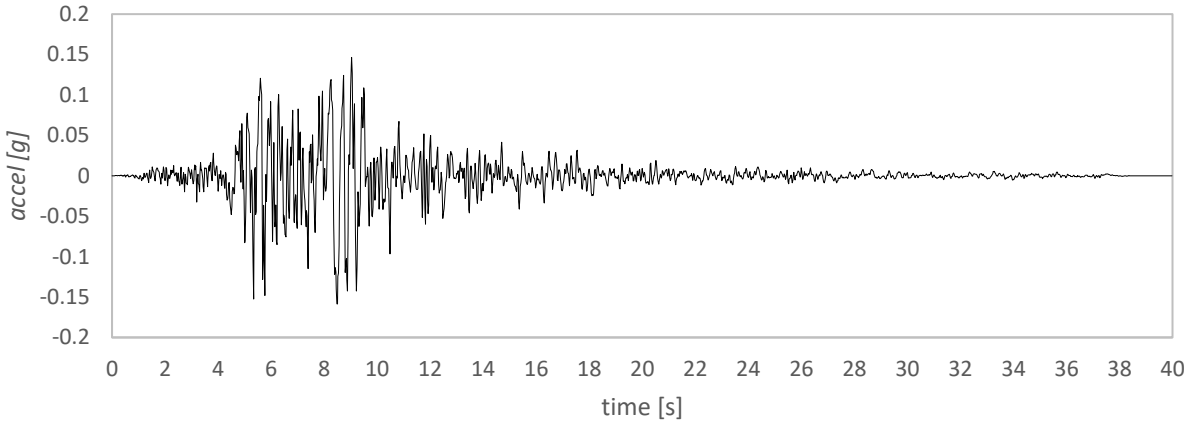

Figure 13. Northridge-01 – 0° acceleration time-history

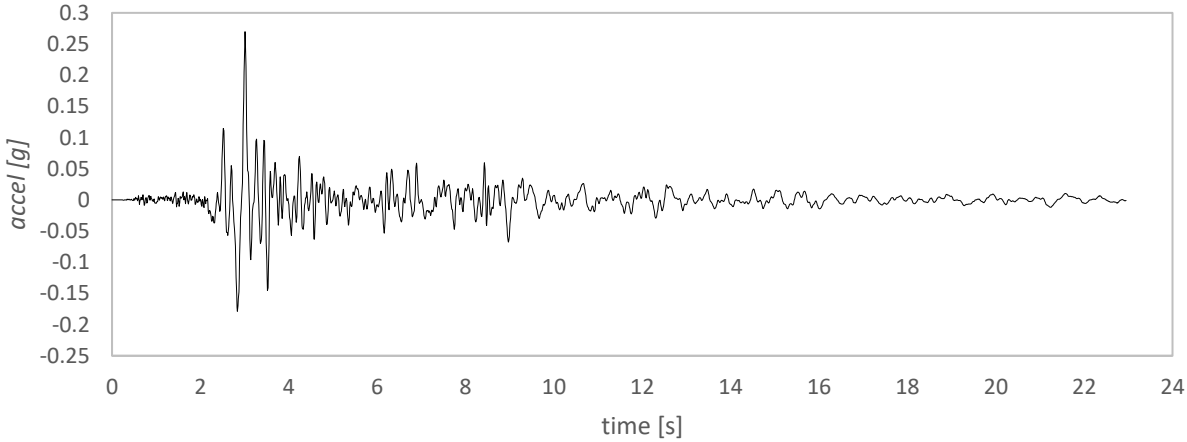

Figure 14. Cosenza – EW acceleration time-history

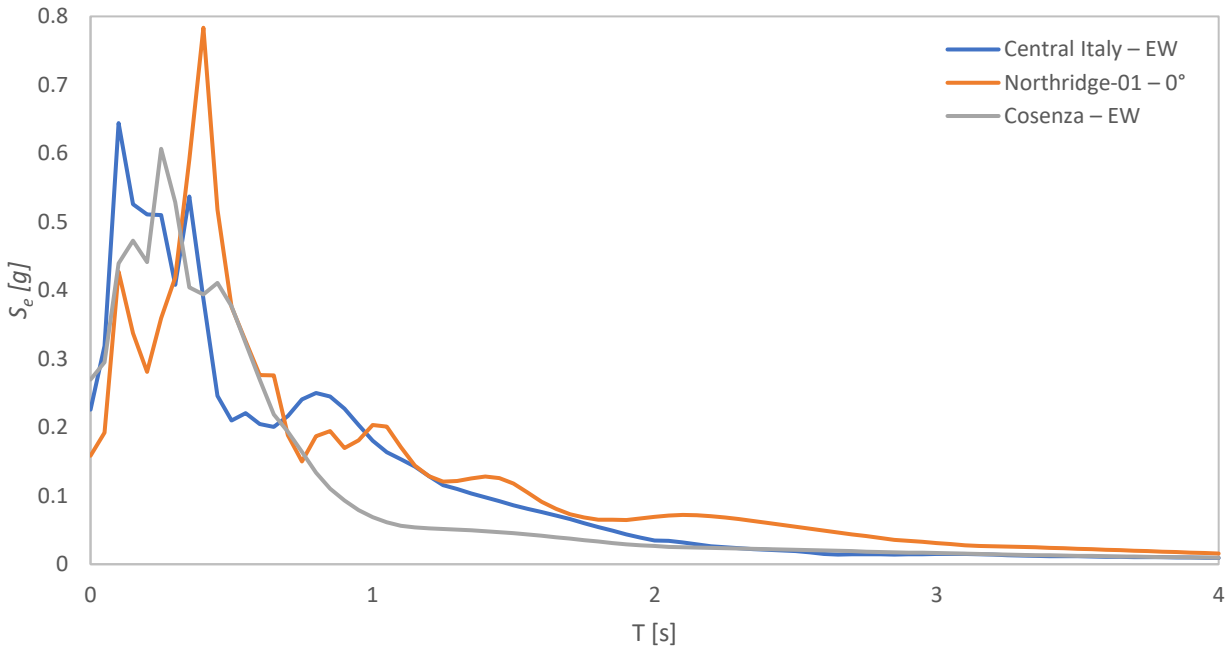

Figure 15. input motion response spectrums

CHAPTER THREE

CHAPTER 4

OPENSEES FRAMEWORK

The Open System for Earthquake Engineering Simulation (OpenSees) is an open-source software developed by the National Science Foundation (NSF) and the Pacific Earthquake Engineering Research Center (PEER) for researching and application purposes on modeling and simulation of structural and geotechnical systems that help to understand their behavior and performance during earthquakes (Mazzoni et al., 2010). Although, its capabilities have been extended for parameter updating and sensitivity analysis, fire simulation, fluid-structure interaction (FSI analysis), useful for Tsunami engineering problems (Mazzoni et al., 2006; Zhu et al., 2018) and parallel computation (Mckenna & Fenves, 2008).

OpenSees is an open-source interpreter with an object-oriented framework for finite element analysis (Mazzoni et al., 2006). Since its inception in 1997, by Frank McKenna on his Ph.D thesis at the University of California at Berkeley, OpenSees have been in continuous development and several modifications have been performed to the framework by the open-source community (Kamath & Jiang, 2015) to keep it updated with the state-of-the-art of finite element models and solution algorithms for nonlinear dynamic analysis of structural and geotechnical systems (Zhu et al., 2018).

4.1. OpenSees Abstractions

The OpenSees framework (object-oriented) is comprised of a set of modules (*Figure 16*), each of them associated with a C++ procedure linked to FORTRAN libraries for solving linear systems of equations (Mazzoni et al., 2006). The main abstractions are:

- *ModelBuilder:* to build the finite element model
- *Analysis*: to specify and run the analysis procedure,
- *Recorder:* to select the quantities to be monitored during the analysis
- *Domain:* to contain and link all the model objects

4.1.1. ModelBuilder

A finite element model (FEM) consists of Nodes, Elements, Constraints and Loads (McKenna, 1997). The ModelBuilder allows to build these objects and add them to the domain (*Figure 16*) and define the spatial dimension of the subsequent nodes to be added on the number of

degrees-of-freedom (DOFs) at each node (Mazzoni et al., 2006). In total there are 5 classes (type of comands) to define the model (*Figure 17*).

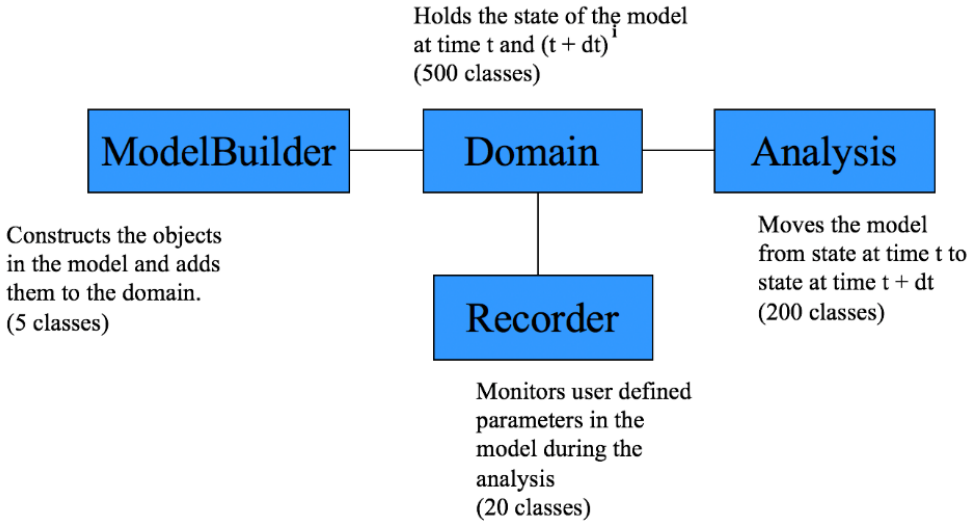

Figure 16. OpenSees Abstractions (Mazzoni et al., 2006)

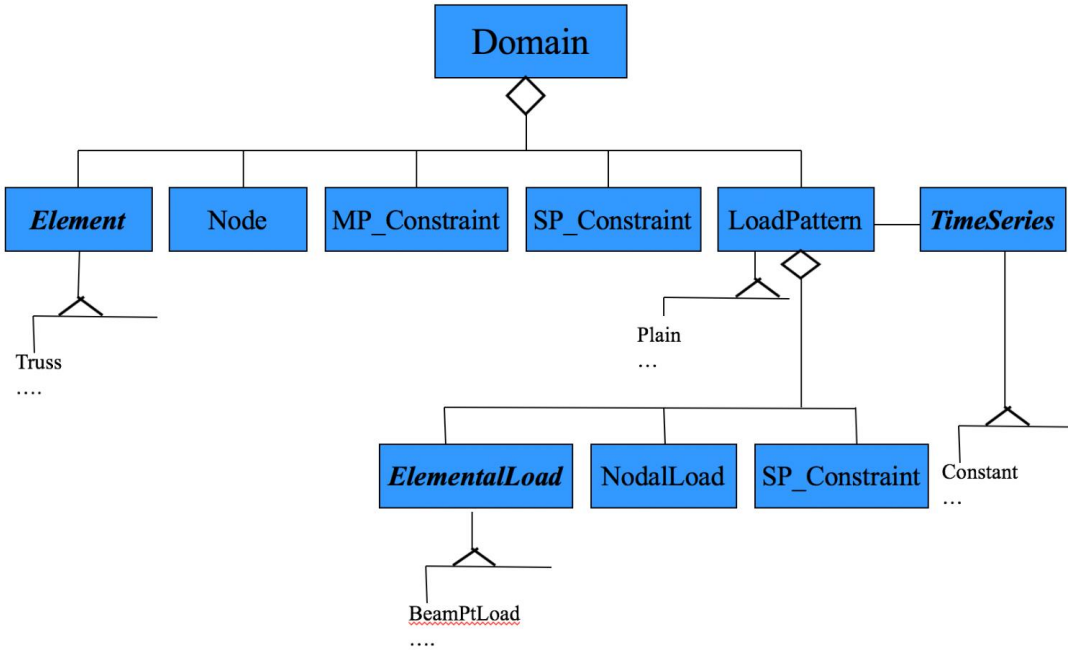

Figure 17. OpenSees Model (Mazzoni et al., 2006)

The node object defines discrete points into the FEM which function is to store their coordinates, response (displacement, velocity and acceleration at each DOF) and unbalanced load information within the domain (McKenna, 1997).

Different types of elements can be created and added to the domain (e.g., ZeroLength Element, Elastic Beam Column Element, Brick Element). Nodes are compulsory to size the elements in the space. The input data and associated objects required to define the mechanical behavior depends on the element type. For example, a brick element (useful to simulate continuum elements) requires a nDMaterial object which represents the stress-strain relationship at its Gauss-Point. Instead, an Elastic Beam Column Element requires a SectionForceDeformation object (to represent the stress-strain relationship) and a Coordinate-Transformation object (to transform the beam element stiffness and resisting force from the basic system to the global-coordinate system) (Mazzoni et al., 2006).

The constraints into the model can be defined using SP_Constraints (Single Point Constraints) for specifying the boundary condition at a node for a specific DOF, that can be constant or time varying, or using MP_Constraints for specifying the relationship between the response of a set of DOFs at one node (the constrained node or slave node) in relation to the response of the DOFs at another node (the retained node or master node) (McKenna, 1997; Mazzoni et al., 2006).

On a Finite Element Model, loads can be nodal (acting on the nodes) or element loads (acting on the elements), which can be due to body forces, surface tractions, initial stresses and/or temperature gradients (McKenna, 1997). In OpenSees the LoadPattern object is used to assign load or motion patterns to the model and add them to the Domain (*Figure 18*); this contains the load (or motion pattern) object (ElementLoad, NodalLoad or SP_Constraint) and the associated TimeSeries object which represents the relationship between the time in the domain, t, and the load factor applied to the loads, λ, into the load pattern (*i.e.*, $\lambda = F(t)$) (Mazzoni et al., 2006).

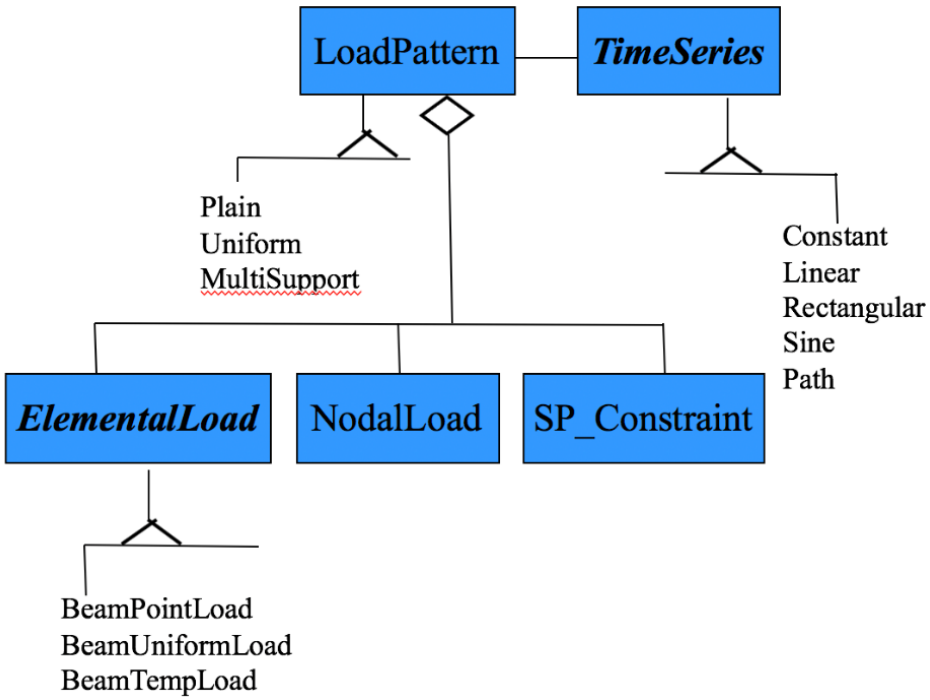

Figure 18. OpenSees Loads Abstractions (Mazzoni et al., 2006)

4.1.2. Analysis

The analysis command is responsible for moving the model along from one converged state at time t to another state at time $t + dt$ through a number of trial steps (Mazzoni et al., 2006). This is an object composed by the aggregation of different component objects (classes) which define the type of analysis (simple linear static analysis, transient non-linear analysis or eigenvalue analysis) and how this is performed, that is the way how the system of equations is defined, stored, and solved during each time step (McKenna, 1997). This system governs the equilibrium and kinematics of the finite-element method and is formed by nonlinear ordinary differential equations (ODEs) (Mckenna et al., 2010).

There are six different classes required to define an analysis object (*Figure 19*):

- *Constrain Handler* - sets out how the constraint equations are enforced into the analysis and how it handles the boundary conditions or imposed displacements
- *DOF Numberer* - defines the mapping between equation numbers and the DOFs at the nodes in the system of equations
- *SystemOfEqn & Solver* - sets out how the system of equations is stored and solved during each time step
- *Convergence Test* - detects when convergence has been achieved on the system of equations at each time step
- *Solution Algorithm* - specifies the sequence of steps taken to solve the non-linear equation at the current time step
- *Integrator* - defines the equations to solve, the predictive step and updates the response at the nodes given the solution to the system of equations (Mazzoni et al., 2006).

All these objects can be defined from the different algorithms available in the OpenSees framework (*Figure 19).* The algorithm to choose for each analysis object depends on the type of problem to solve.

4.1.3. Domain

The Domain object is a container responsible for holding all the components (objects) of the Finite Element Model (i.e., Nodes, Elements, Constraints and Loads) and for providing access to the Analysis and Recorder objects to them (*Figure 20*), that is the Domain is associated directly with the ModelBuilder and Analyisis objects (McKenna, 1997).

4.1.4. Recorder

The recorder objects are used for monitoring the state of a domain component (e.g., node, element, etc.) during an analysis and write this information into a file (.txt file) or database in time history format for being post-processed easily (Mazzoni et al., 2006).

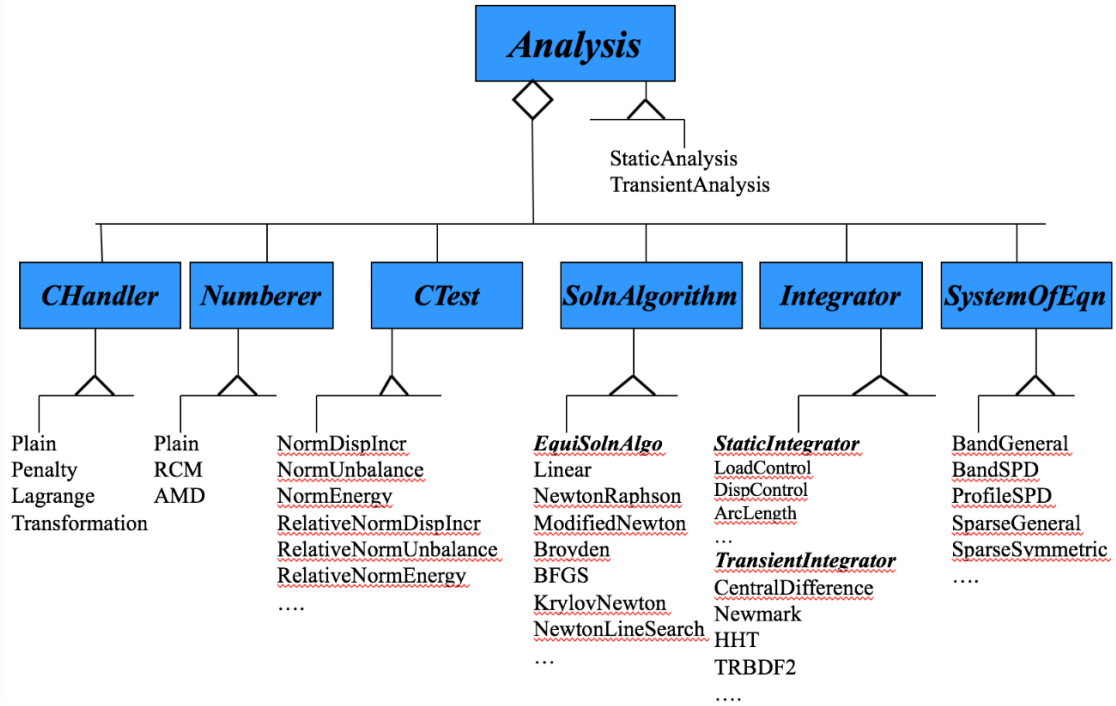

Figure 19. Opensees Analysis Abstraction (Mazzoni et al., 2006)

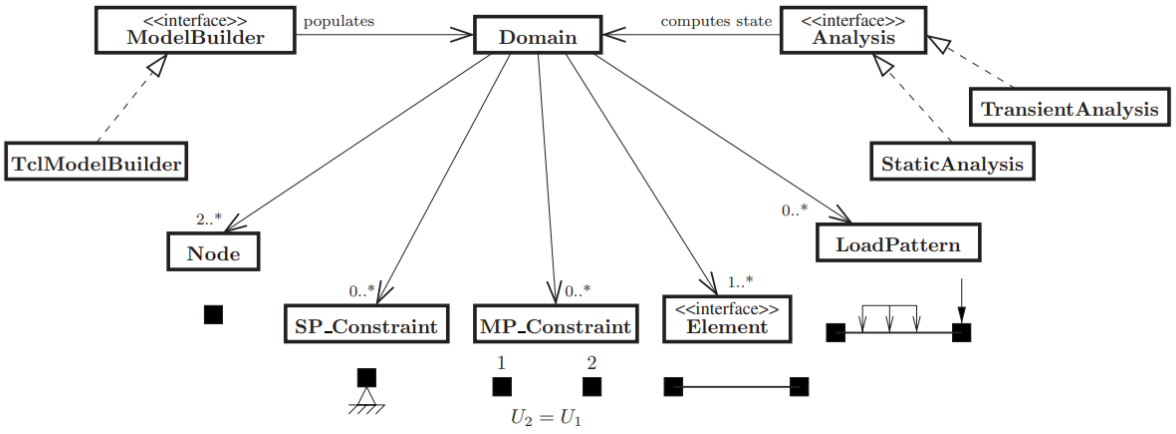

Figure 20. OpenSees framework using the unified modeling language notation (Mckenna et al., 2010)

4.2. OpenSeesPy

Since the conception of OpenSees, Tcl has been the primary scripting language to which the model building and analysis modules are linked (Zhu et al., 2018). Aiming at providing users with different scripting language options, OpenSeesPy was created and launched on 2018 by

Minijie Zhu (Research Associate at the Oregon State University) as a Python module. With this new interface for the OpenSees framework, the user can take advantage of using the Python scripting language (simpler than Tcl) and its libraries for pre-processing and post-processing the input and output data like *vfo* (Visualization for OpenSees) and *opsivs* specially developed for this purpose (Zhu, 2023).

CHAPTER 5

PDMY CONSTITUTIVE MODEL

The PressureDependMultiYield (PDMY) is one of the UC San Diego soil models developed for simulating linear and nonlinear, dry, drained and undrained soil response of pressure sensitive soil materials (e.g., cohesionless soils) under general 2D and 3D static and cyclic loading conditions (Yang et al., 2008).

In this elastic-plastic model, elasticity is assumed as linear and isotropic, and plasticity, responsible of nonlinearity and anisotropic behavior, is formulated based on the multi-surface (nested surfaces) concept, with a purely deviatoric kinematic hardening rule and a non-associative flow rule to reproduce dilatancy effect (shear induced volume contraction or dilation), and conical yield surfaces in the principal stress space (Drucker-Prager type - *Figure 21*) (Yang et al., 2003).

A brief description of the constitutive model, in terms of yield function, hardening rule, flow rule and shear stress-strain response, is presented in this chapter.

5.1. Yield Function

The yield function is given in the domain $p' \geq 0$ by:

$$f = \frac{3}{2}\left[\boldsymbol{s} - \left(p' + p'_0\right)\boldsymbol{\alpha}\right] : \left[\boldsymbol{s} - \left(p' + p'_0\right)\boldsymbol{\alpha}\right] - M^2\left(p' + p'_0\right)^2 = 0 \qquad \textbf{Eq. 1}$$

where:

$\boldsymbol{s} = \boldsymbol{\sigma}' - p'\boldsymbol{\delta}$

$\boldsymbol{s} = deviatoric\ stress\ tensor$

$\boldsymbol{\sigma}' = effective\ Cauchy\ stress\ tensor$

$\boldsymbol{\delta} = second - order\ identity\ tensor$

$p' = mean\ effective\ stress$

$p'_0 = 1.0\ kPa\ (small\ positive\ constant\ used\ for\ keeping\ the\ yield\ surface\ finite\ at\ p' = 0)$

$\boldsymbol{\alpha} = second - order\ deviatoric\ tensor\ (defines\ the\ yield\ surface\ center\ in\ deviatoric$

$stress\ subspace)$

$M = yield\ surface\ size$

: $denotes\ a\ doubly\ contracted\ tensor\ product$

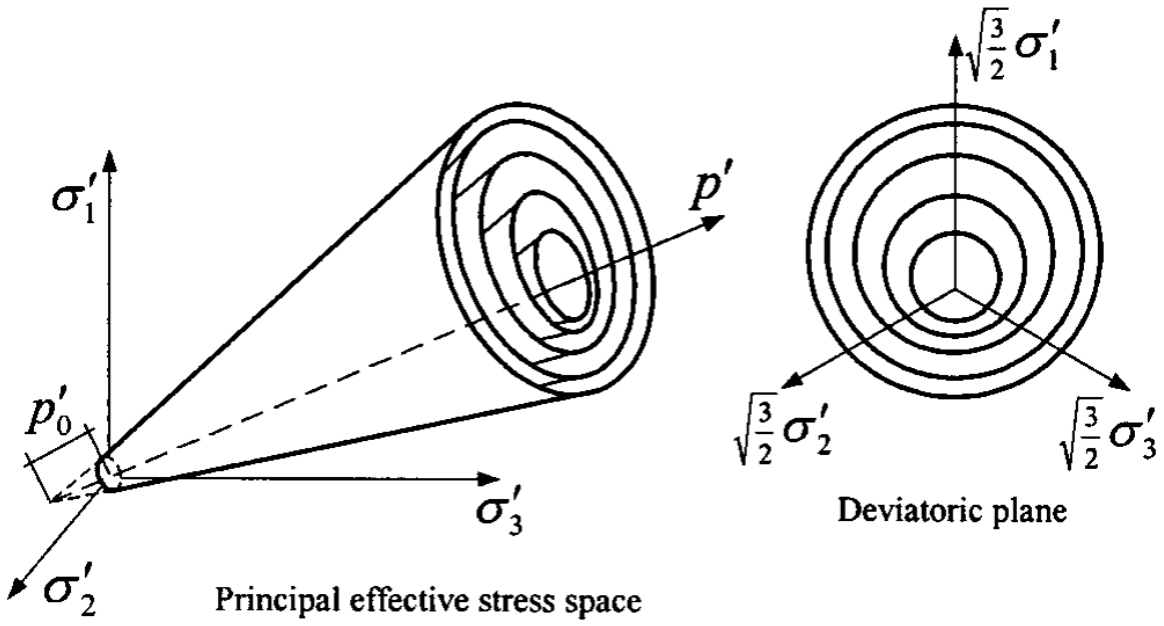

Figure 21. Drucker-Prager conical yield surfaces in principal stress space and deviatoric plane (taken from Yang et al., 2003)

Notice that yield function (*Eq. 1*) doesn't include the third stress invariant, therefore, the Lode angle effect is not incorporated into the model, so load paths that depend strongly on this effect will not be reproduced satisfactorily (Yang et al., 2003).

The outermost yield surface (*Figure 21*) is designated as the failure surface, which size (M_f) is related directly to the friction angle φ by $M_f = (6\sin\varphi)/(3-\sin\varphi)$ (Chen & Mizuno, 1990; Yang et al., 2003).

The use of a small positive constant (p'_0) is because of numerical convenience and for avoiding ambiguity in defining the yield surface normal at the yield surface apex, this guarantee that the yield surface remains constant at $p' = 0$ (Yang et al., 2003).

5.2. Hardening rule

The model uses a purely deviatoric kinematic hardening rule to generate hysteric response, based on Mroz (1967) and Prevost (1985) models, and it includes an improvement on the surface-translation hardening rule aiming to enhance computational efficiency but keeping the Mroz (1967) concept of conjugate-point contact (Yang et al., 2003).

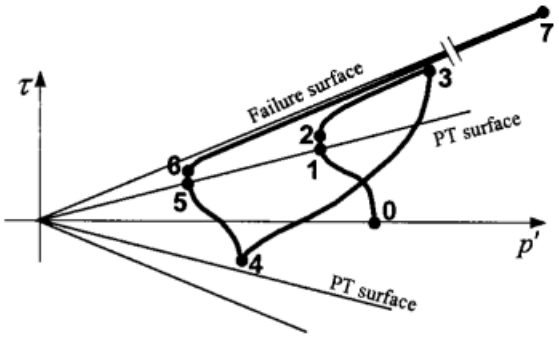

Figure 22. Dilatancy behavior and Phase transformation (PT) surface (taken from Yang et al., 2003)

5.3. Flow Rule

The non-associativity flow rule type involves just the volumetric component of the plastic flow (Yang et al., 2003), and includes the concept of the phase transformation (PT) surface (Ishihara et al., 1975) (*Figure 22*), which helps to predict the dilatancy direction (volume contraction or dilation), and the resulting increase (or decrease) on pore pressure u and decrease (or increase) on mean effective stress p', considering if the stress state is inside or outside of the PT surface.

The relative location of the stress state with respect to the PT surface is inferred from the stress ratio $\eta = \sqrt{3(\boldsymbol{s}:\boldsymbol{s})/2}(p' + p'_0)$ and the stress ratio along the PT surface η_{PT} as follows: $\eta < \eta_{PT}$ (or $\eta > \eta_{PT}$) if the stress state is inside (or outside) the PT surface. In this way, depending on the value of η and $\dot{\eta}$ (the time rate of η) the model considers the contractive/dilative behavior (dilatancy) of the material (Yang et al., 2003).

5.4. Shear Stress-Strain Response

The low-strain domain of the shear stress-strain response (elastic behavior) considers the variation of low shear-strain modulus G with confinement p' proposed by (Prevost, 1985):

$$G = G_r \left(\frac{p'}{p'_r} \right)^d \qquad \textbf{Eq. 2}$$

where p'_r is the reference mean effective confinement pressure (usually taken as 80 kPa), G_r is the low-strain shear modulus at p'_r and d is a material parameter (typically equal to 0.5 for sand (Kramer, 1996). Based on the theory of elasticity and considering that bulk modulus of the soil skeleton B follows the same confinement dependence rule of G (*Eq. 2*) then:

$$B = B_r \left(\frac{p'}{p'_r} \right)^d \qquad \textbf{Eq. 3}$$

where $B_r = 2G_r(1+\nu)/(3-6\nu)$, and ν is the Poisson ratio (Yang et al., 2003).

For non-linear shear behavior, the model uses a hyperbolic shear stress-strain backbone curve (*Figure 23*) defined on octahedral shear stress-strain plane ($\tau - \gamma$) for a given p'_r (Kondner, 1963; Duncan & Chang, 1970):

$$\tau = G_r\gamma/(1+\gamma/\gamma_r) \qquad \textbf{Eq. 4}$$

where τ and γ are the octahedral shear stress and strain, respectively (*Eq. 5* & *Eq. 6*) (Yang et al., 2008); and $\gamma_r = \tau_{max}/G_r$, in which $\tau_{max} = \lim_{\gamma\to\infty}\tau$ (*Figure 23*).

$$\tau = \frac{1}{3}\left[(\sigma_{xx}-\sigma_{yy})^2 + (\sigma_{yy}-\sigma_{zz})^2 + (\sigma_{xx}-\sigma_{zz})^2 + 6\sigma_{xy}^2 + 6\sigma_{yz}^2 + 6\sigma_{xz}^2\right]^{1/2} \qquad \textbf{Eq. 5}$$

$$\gamma = \frac{2}{3}\left[(\varepsilon_{xx}-\varepsilon_{yy})^2 + (\varepsilon_{yy}-\varepsilon_{zz})^2 + (\varepsilon_{xx}-\varepsilon_{zz})^2 + 6\varepsilon_{xy}^2 + 6\varepsilon_{yz}^2 + 6\varepsilon_{xz}^2\right]^{1/2} \qquad \textbf{Eq. 6}$$

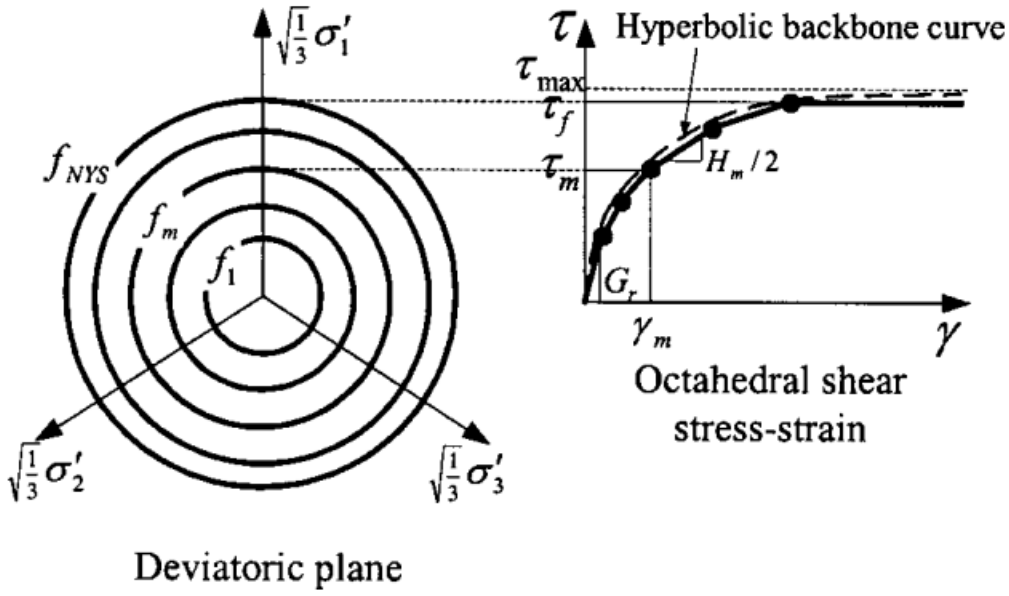

Figure 23. Hyperbolic backbone curve for soil non-linear shear stress-strain response and piecewise-linear representation in multisurface plasticity (taken from Yang et al., 2003)

In agreement with the framework of multisurface plasticity (Yu, 2007), the hyperbolic shear stress-strain backbone curve (*Eq. 4*) is discretized by N number of yield surfaces (*Figure 23*), each linear segment represents the domain of a yield surface f_m characterized by elastoplastic

shear modulus H_m (*Eq. 7*) (which follow the same confinement dependence rule expressed on *Eq. 2*) and size M_m (*Eq. 8*) where $m = 1,2,\dots,N$ (Yang et al., 2003).

$$H_m = 2(\tau_{m+1} - \tau_m)/(\gamma_{m+1} - \gamma_m) \qquad \textbf{Eq. 7}$$

$$M_m = 3\tau_m / \sqrt{2}(p'_r + p'_0) \qquad \textbf{Eq. 8}$$

5.5. Critical-state line:

The model also allows to define a straight critical-state line e_c in $e - p'$ space as follows:

$$e_c = e_\Gamma - \lambda_c \left(\frac{p_c}{p_a}\right)^\xi \qquad \textbf{Eq. 9}$$

where e_c and p_c are the critical void ratio and associated critical mean normal stress, respectively; p_a is the atmospheric pressure $(101\,kPa)$ taken as a reference pressure for convenience; and λ_c , ξ , and e_Γ are dimensionless material constant (Li et al., 1999). These parameters are optional into the model but are needed when critical-state response (e.g., in liquefaction induced flow) is anticipated (Yang et al., 2008).

5.6. PDMY input parameters

Ignoring the parameters controlling the mechanism of liquefaction-induced perfectly plastic shear strain accumulation (i.e., cyclic mobility), this means deactivating this mechanism inside the model, there are 15 input parameters required for the PDMY model, listed in *Table 4.*

Table 4. Input parameters for PDMY model

Constant	***Variable***
Saturated soil mass density	ρ_{sat}
Elasticity parameters	G_r ν
Reference mean effective pressure	p'_r
Pressure dependance coefficient	d
Peak friction angle	φ
Peak octahedral shear strain	γ_{max}
Phase transformation angle	φ_{PT}
Contraction parameter	c
Dilatancy parameters	d_1 d_2

Critical State parameters	e_0 λ_c ξ
Number of yield surfaces	N

CHAPTER 6

VALIDATION OF THE NUMERICAL MODEL

In order to validate the finite-element model, different site response analysis (1D, 2D and 3D) have been performed using first a simple isotropic elastic constitutive model and comparing the results with Strata (Kottke & Rathje, 2009), to move later into a more advanced elastic-plastic constitutive model (PDMY) to compare with the results of Gorini (2017).

6.1. Model Geometry and Boundary Conditions

6.1.1. 1D Finite Element Model

The 1D Finite Element Model is presented in *Figure 24.* The mesh was created using FourNodeQuad element objects which use a bilinear isoparametric formulation and have four integration points (*Figure 25a*) (Mazzoni et al., 2006). The vertical and horizontal size of the elements was chosen considering the highest frequency (to be well resolved) of the input motion and the minimum wave velocity in such a way the minimum wave length fits into four elements. This criterion ensures that the mesh is refined enough such that the desired aspect of the propagating waves is well captured into the analysis (Lysmer & Kuhlemeyer, 1969; Lysmer, 1978).

Two boundary conditions were defined. The first, consisted on assigning vertical constraint to the vertical displacement (y-direction) to the base nodes (interface soil-bedrock) of the soil mesh using SP-Constraints. The second, establishing equal-degree-of-freedom (equalDOF), MP_Constraints, to the lateral nodes with the same vertical coordinate. This command ties the nodes horizontally and vertically, to simulate a simple shear deformation pattern (C. McGann & Arduino, 2011).

6.1.2. 2D Finite Element Model

The 2D Finite Element Model is presented in *Figure 26.* The horizontal size of the model was assigned as 10 times the vertical size. Aiming to reduce the computational time, the FourNodeQuad element objects were changed by SSPquad element objects (*Figure 25b)*, which are four-node quadrilateral elements that use a physically stabilized single-point integration SSP (C. R. McGann et al., 2012). This means that these elements have just one Gauss Point and then the computational demand is much lower. The vertical and horizontal size

of the elements, and boundaries conditions were set following the same criteria as the 1D FEM model.

6.1.3. 3D Finite Element Model

The 3D Finite Element Model is presented in *Figure 27.* The horizontal size of the model, in *x* & *y* directions, was set equal to 10 times the vertical size. The mesh was created using SSPbrick elements (*Figure 28*), which are eight-node hexahedral elements with physically stabilized single-point-integration, this means they have just one Gauss Point. Because of this, the computational time is considerably lower compared with full integration elements (Mazzoni et al., 2006; C. McGann et al., 2011). For practical purposes and looking for decrease more the computational time, the horizontal size of the brick elements was defined as 10 times the vertical one, which was set obeying the criteria of one wave length fit into four elements, this simplification doesn't affect the results considering that shear waves travel in vertical direction.

The boundary conditions were set in the same way as the previous 1D & 2D Models, setting SP_Constraints just in the vertical direction for the base nodes, and MP_Constraints in the three degrees of freedom of lateral nodes that shares vertical coordinate and one of the two horizontal coordinates to simulate the simple shear deformation pattern (C. McGann & Arduino, 2011).

6.2. Dynamic Loading and Bedrock Impedance

The input motion was applied thought a force time history, $F(t)$, applied at the base nodes of the soil mesh (*Figure 24, Figure 26 & Figure 27*), equal to the product of the bedrock impedance (rock density, ρ, times rock shear wave velocity, V_s), the effective area of each of the base nodes, A, and the velocity time history of the input motion, $\dot{x}(t)$ (*Eq. 10)* (Joyner & Chen, 1975; Lysmer, 1978; C. McGann & Arduino, 2011).

$$F(t) = \rho\, V_s\, A\, \dot{x}(t) \qquad \textbf{Eq. 10}$$

In order to account for the finite rigidity of the underlying half-space (bedrock impedance), a Lysmer-Kuhlemeyer (1969) dashpot was incorporated at the base nodes of the soil mesh as well (*Figure 24, Figure 26 & Figure 27*). The dashpots were assigned using zeroLength elements (C. McGann & Arduino, 2011) with a coefficient, c, equal to the product of the bedrock impedance and the effective area of each of the base nodes (*Eq. 11*) (Joyner & Chen, 1975; Lysmer, 1978).

$$c = \rho\, V_s\, A \qquad \textbf{Eq. 11}$$

The use of the effective area, A, of each of the base nodes guarantees proportional loading and impedance respectively (Joyner & Chen, 1975; Lysmer, 1978; C. McGann & Arduino, 2011). Notice that unit width has been considered in the 1D and 2D FEM to compute A.

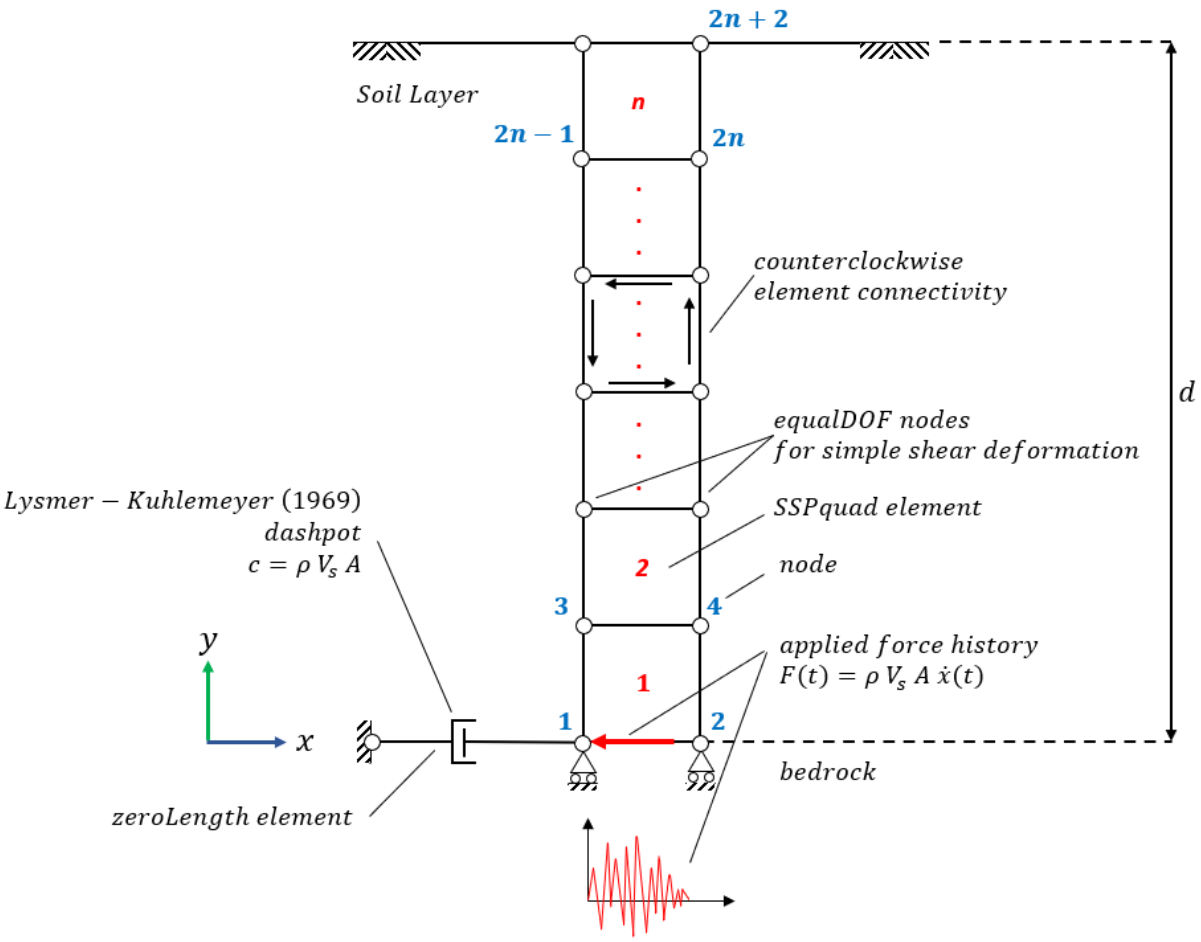

Figure 24. Schematic representation of the 1D Model. Node numbers in blue, element numbers in red (adapted from C. McGann & Arduino, 2011)

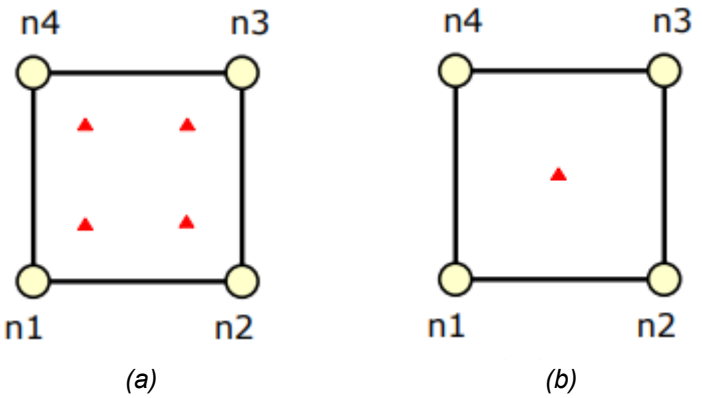

Figure 25. 2D four node solid element objects. (a). FourNode quad element, (b). SSPquad element object (taken from Arduino, 2023)

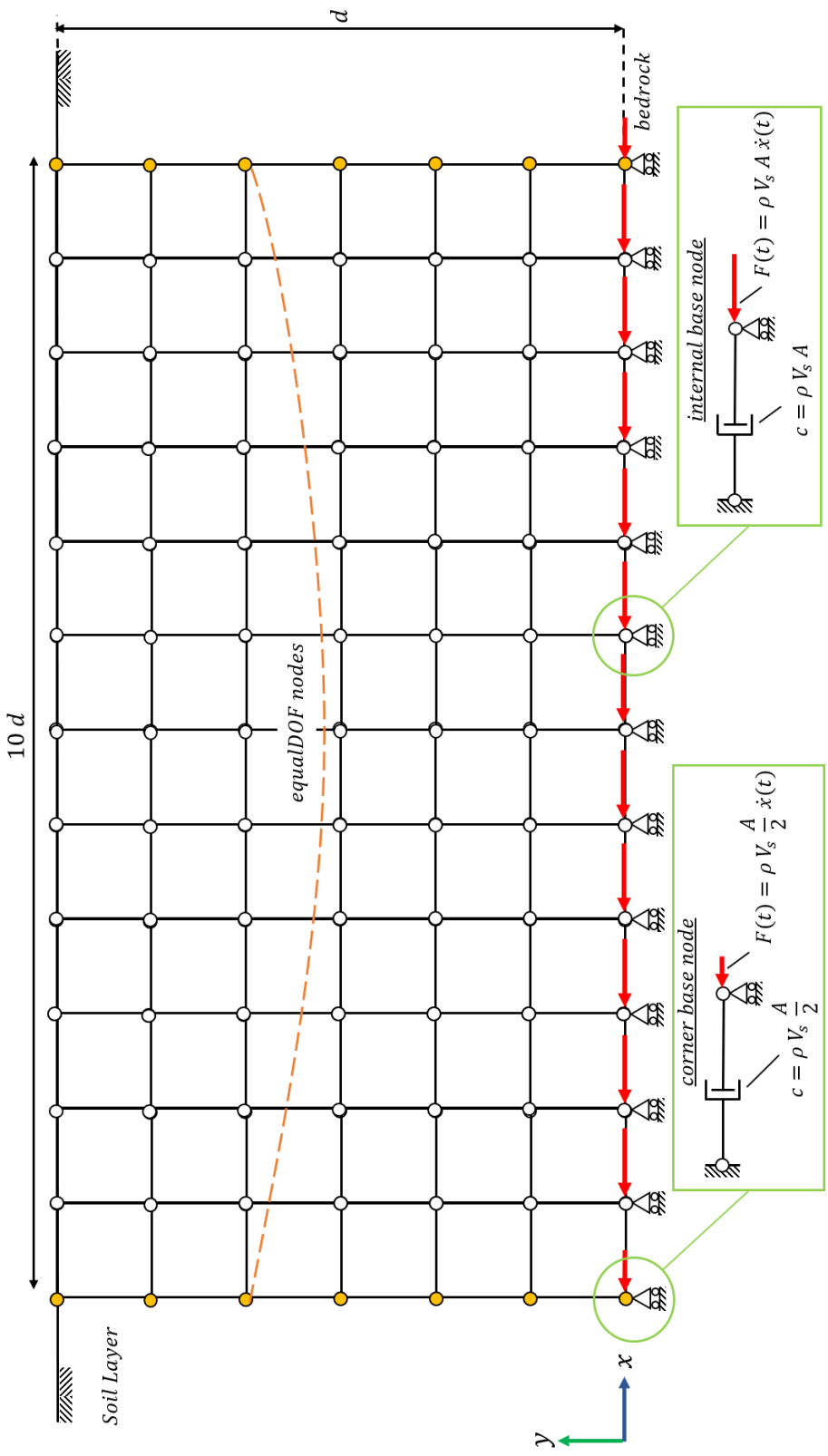

Figure 26. Schematic representation of the 2D Model

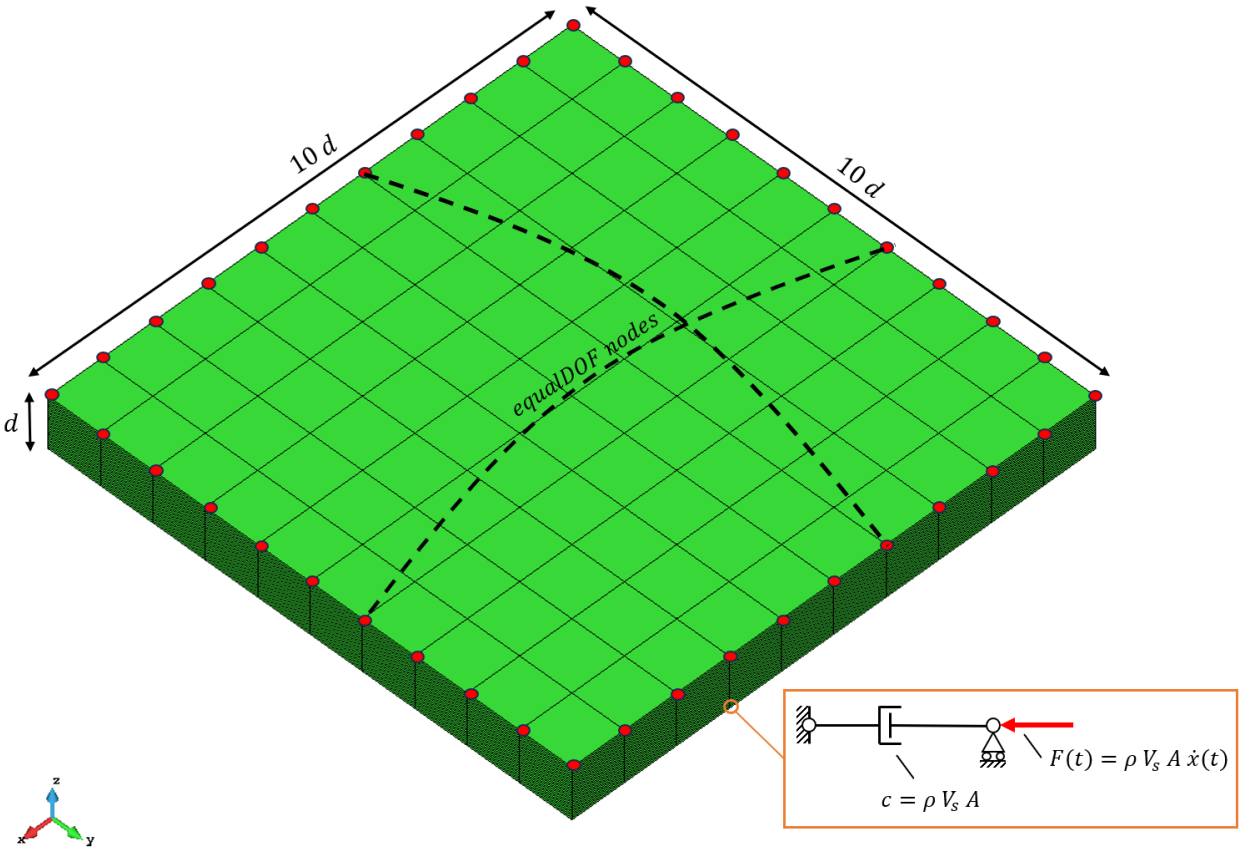

Figure 27. Schematic representation of the 3D Model

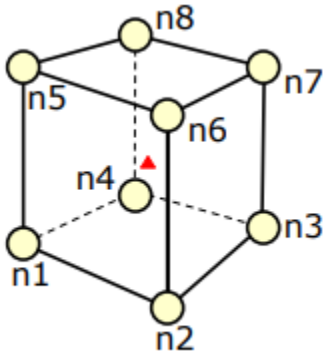

Figure 28. SSPbrick element (taken from Arduino, 2023)

6.3. Rayleigh Damping

A Rayleigh viscous proportional damping formulation (*Eq. 12*) was used to simulate the energy dissipation at low strains domain (Petrini et al., 2008).

$$\boldsymbol{C} = a_0\boldsymbol{M} + a_1\boldsymbol{K} \qquad \textbf{Eq. 12}$$

In the OpenSees framework, the Rayleigh damping formulation uses a two control frequencies approach (*Figure 29*). These two circular frequencies (ω_i , ω_j) correspond to two modes of vibration and together with the damping ratio (ξ) control the level of Reyleigh damping by computing the mass proportional (a_0) and stiffness proportional coefficients (a_1) (*Eq. 13*), which are the input parameters into the model (Charney & Asce, n.d.; Chopra, 2007). These two control frequencies are computed using the Verrucci et al., (2022) approach, presented on *Eq. 14*. This method defines the fundamental natural frequency of the soil deposit (f_0) as the first control frequency (f_1) and the second control frequency (f_2) as a function of f_0 and the predominant frequency of the input motion f_p.

$$a_0 = \xi\frac{2\omega_i\omega_j}{\omega_i + \omega_j} \quad a_1 = \xi\frac{2}{\omega_i + \omega_j}. \qquad \textbf{Eq. 13}$$

$$\begin{cases} f_1 = f_0 \\ f_2 = nf_1 \end{cases} \text{ with } n \text{ closest odd integer greater than } \frac{f_p}{f_0} \qquad \textbf{Eq. 14}$$

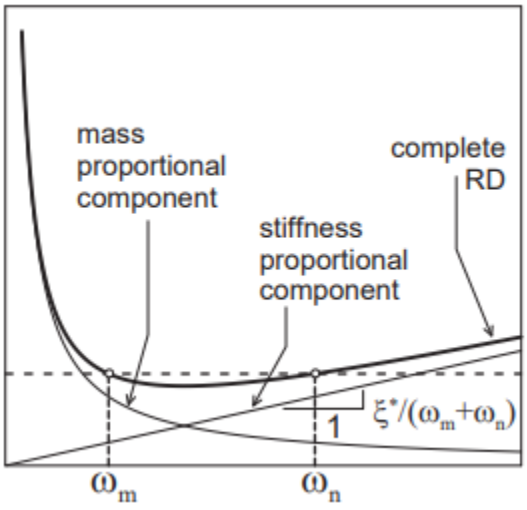

Figure 29. Rayleigh damping using Two Control Frequencies approach (taken from Verrucci et al., 2022)

6.4. Transient Analysis

The Newmark numerical integration method was chosen, to perform the transient (dynamic) analysis, using the average constant acceleration scheme (middle point rule) by setting γ and β coefficients equal to 0.5 and 0.25 respectively to ensure no numerical damping during the analysis (Newmark, 1959; C. McGann & Arduino, 2011).

Aiming to guarantee the numerical stability during the dynamic analysis, the time step (dt) was defined according to the *Courant-Friedrich-Lewy (CFL) condition* (*Eq. 15*) to ensure that time step is small enough that the fastest shear wave velocity ($V_{s,max}$) fits into the minimum mesh size element (dx_{min}) (LeVeque, 2007):

$$dt_{CFL} \leq \frac{dx_{min}}{V_{s,max}} \qquad \textbf{Eq. 15}$$

In case that the input motion time step (dt_{IM}) is smaller than the one provided by the CFL criterion (dt_{CFL}), the dt_{IM} must be use to avoid numerical problems during the simulation (*Eq. 16)* (C. McGann & Arduino, 2011).

$$dt = \min\left(dt_{CFL}; dt_{IM}\right) \qquad \textbf{Eq. 16}$$

6.5. Validation for Elastic Isotropic Model

To validate the numerical model, a site response analysis was performed using an elastic-isotropic constitutive law for the soil. The proposed problem consisted on an elastic medium (soil) underlined by a finite rigidity elastic medium (bedrock) (*Figure 30*). The objective of this first validation stage was to compare the results of the 1D, 2D and 3D FEM models with Strata (Kottke & Rathje, 2009), which implements a linear visco-elastic model based on analytical solutions. The depth of the soil deposit, d, was set equal to 20 m. The mechanical parameters of the elastic overlaying and underlaying mediums are presented on *Table 5*.

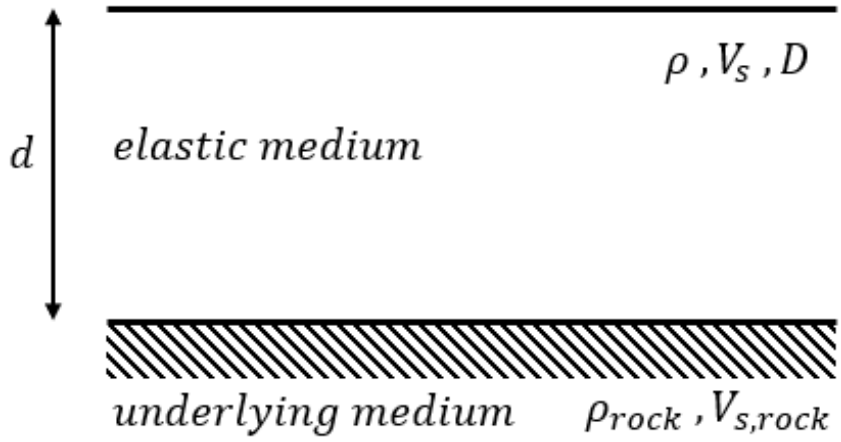

Figure 30. Elastic Soil and Underlying Bedrock Mediums

Table 5. Soil and Bedrock Geotechnical parameters for Elastic Constitutive Law

Medium	$\rho\ \left[\frac{Mg}{m^3}\right]$	$V_s\ \left[\frac{m}{s}\right]$	$\nu\ [-]$	$\xi\ [\%]$
Soil	*1.7*	*300*	*0.2*	*2.0*
Bedrock	*2.5*	*900*	-	-

$\rho: density$

$V_s: shear\ wave\ velocity$

$\nu: Poisson\ ratio$

$\xi: damping\ ratio$

6.5.1. Static (gravitational) Loading

In order to assess the stress state of the soil, prior to the dynamic horizontal loading, a static or gravitational loading step must be performed (consolidation step). The results of this first step for the 1D, 2D & 3D FEM models, are presented and compared, in terms of displacements and stresses, with the analytical solutions (*Eq. 17 & Eq. 18*) on *Table 6*.

$$\varepsilon_v = \frac{1}{E}\left(\sigma_v - \nu(2\sigma_h)\right) \qquad \textbf{Eq. 17}$$

$$\Delta_v = \varepsilon_v * H \qquad \textbf{Eq. 18}$$

Table 6. Gravitational Loading with Elastic Law

Parameter		*Numerical 1D, 2D & 3D*	*Analytical*
disp at top [m] - Δ_v		$-8.16 * 10^{-3}$	$-8.16 * 10^{-3}$
stress at 18.59 m depth [kpa]	$\sigma_v = \gamma h$	*309.40*	*309.71*
	$\sigma_h = \frac{\nu}{1-\nu}\sigma_v$	*77.35*	*77.43*

6.5.2. Dynamic Horizontal Loading and Comparison

Looking at the PEER Ground Motion Database (Pacific Earthquake Engineering Research Center, 2023) and following one of the examples provided by C. McGann & Arduino, (2011) at the OpenSees website, the *GilroyNo1EW* acceleration time history (*Figure 31*) was selected as input motion. A brief description of the time-history record is presented on *Table 7.*

Table 7. Gilroy Event

Event Name	*Gilroy*
Year	*2002*
Recorder station	*Gilroy - Gavilan Coll.*
Magnitude	*4.9*
Mechanism	*Strike slip*
PGA [g]	*0.16*

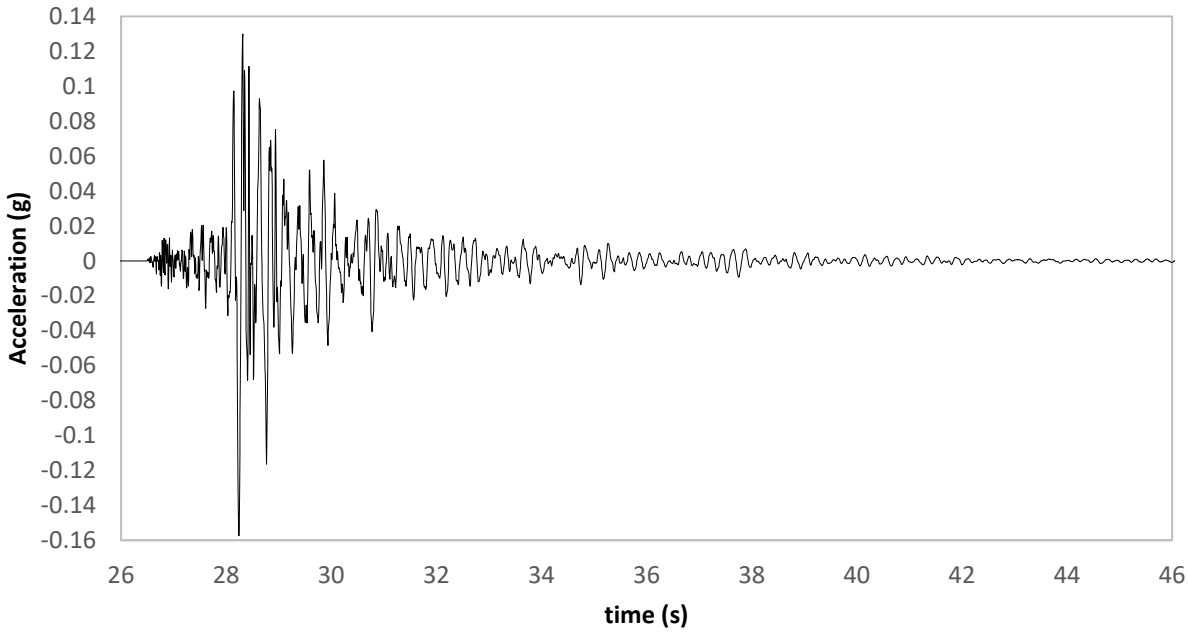

Figure 31. GilroyNo1EW acceleration time history

The results of this elastic dynamic analysis are presented and contrasted with Strata in terms of acceleration time history (*Figure 32*) and response spectra (*Figure 33*) at the ground surface (free-field condition), for the 1D, 2D and 3D models.

For visualization purposes, the acceleration time history at ground surface (*Figure 32*) is cutoff on the interest time interval (*27s – 33s*). It can be concluded, looking at response spectra (*Figure 33*) that the three OpenSees FEM model results match perfectly among them and with the Strata 1D analytical solution, there is just a slight difference in the response spectra, on the high frequency domain, that can be related to the differences on the damping formulation in the two methods (C. McGann & Arduino, 2011), constant on Strata and frequency-dependent on OpenSees.

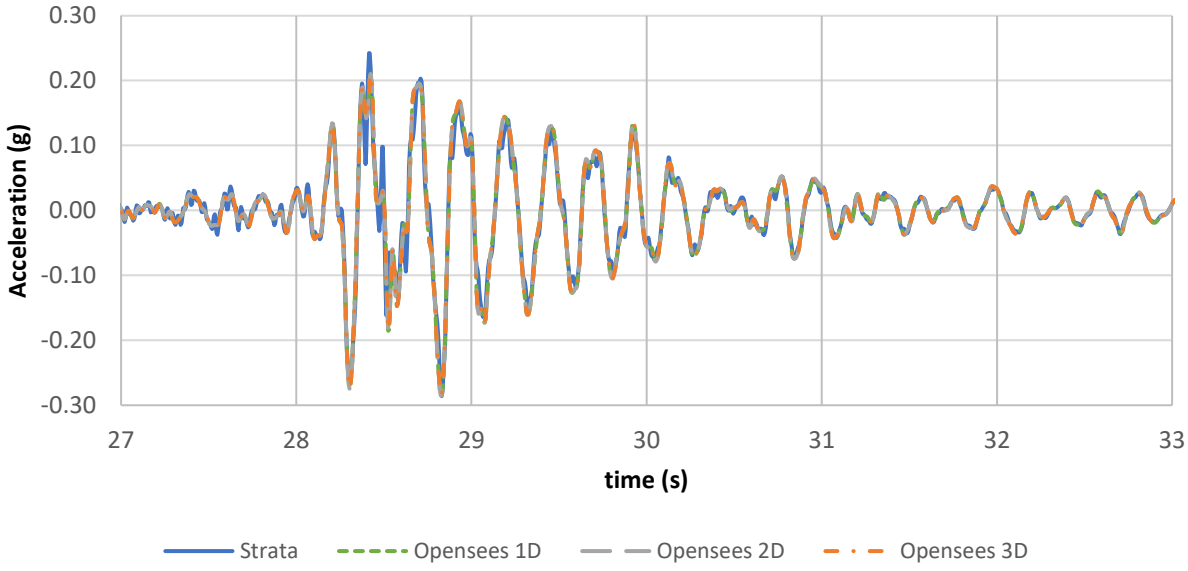

Figure 32. Acceleration time history at ground surface

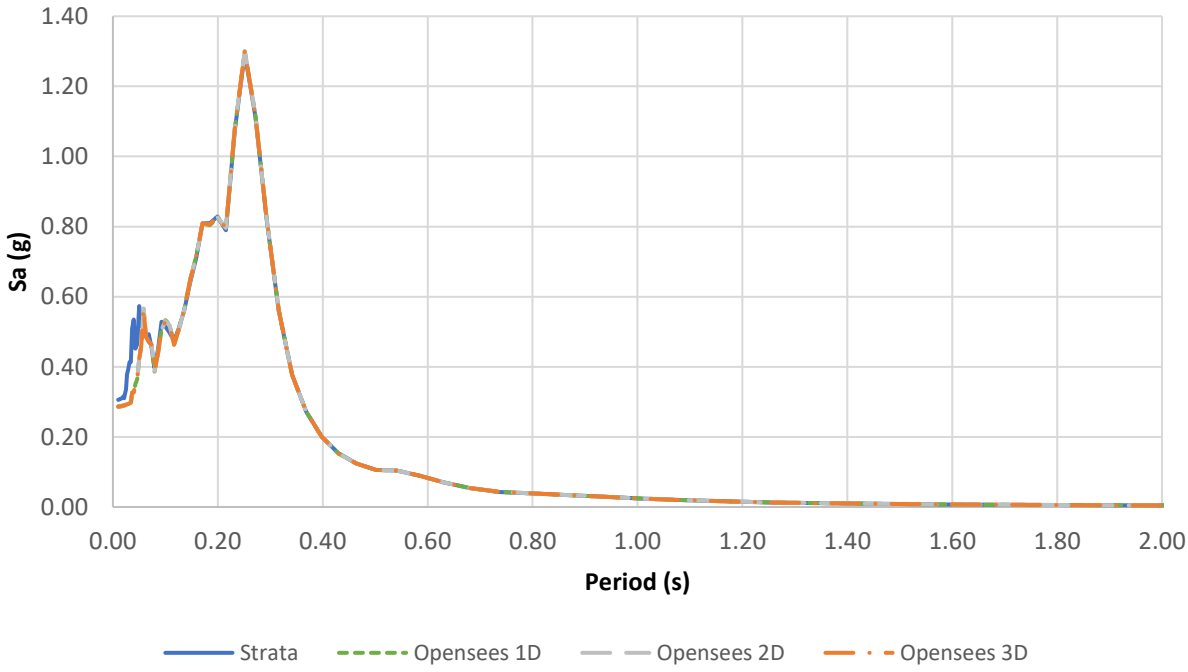

Figure 33. Acceleration response spectra at the ground surface

6.6. Validation for PDMY Model

Moving forward with a more advance elastic-plastic constitutive law that represents better the seismic response of the soil stratum under cyclic loading, the PDMY constitutive model was adopted into the numerical model.

Aiming at validating the use of the PDMY constitutive law, the 1D site response analysis reported on the PhD. Thesis of Davide Gorini (2017) was used to compare, first, the 1D FE model (*Figure 24*), and later, to proceed with the 2D and 3D FEM validation.

The PDMY input parameters, reported on *Table 8,* are the result of a calibration process performed by Gorini (2017) to a set of data coming from Messina Strait geotechnical explorations (Crova et al., 1993; Jamiolkowski & Lo Presti, 2002; Brancaleoni et al., 2010; Fioravante et al., 2012).

The geometry of the 1D site response analysis and the input motion to use are presented on *Figure 34* and *Figure 35* respectively. It is important to highlight that the input motion (*Figure 35)* comes from a deconvolution process performed by Gorini (2017) (*Figure 36*) aiming at decreasing the computational demand in his case study. A brief description of this deconvolution process is presented below.

Table 8. PDMY input parameters used by Gorini, (2017)

Constant	***Variable***	***Value***
Saturated soil mass density	$\rho\ [Mg/m^3]$	*2.243*
Elasticity	$G_r\ [kpa]$	*1.3*10⁵*
	ν	*0.2*
Reference mean effective pressure	$p'_r\ [kpa]$	*80*
Pressure dependance coefficient	d	*0.5*
Peak friction angle	$\varphi\ [\circ]$	*35.0*
Peak octahedral shear strain	γ_{max}	*0.1*
Phase transformation angle	$\varphi_{PT}\ [\circ]$	*17.0*
Contraction	c	*0.195*
Dilatancy	d_1	*0.6*
	d_2	*3.0*
Critical State	e_0	*0.0219*
	λ_c	*0.4478*
	ξ	*0.7*
Number of yield surfaces	N	*40*

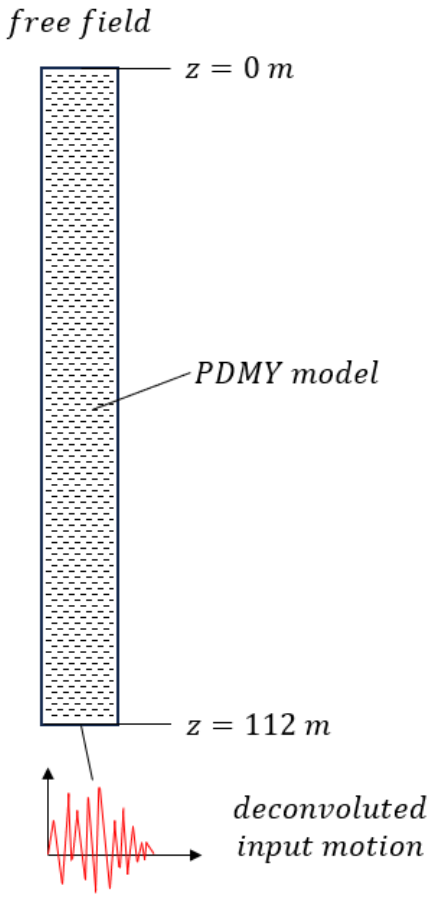

Figure 34. 1D site response analysis using deconvoluted input motion

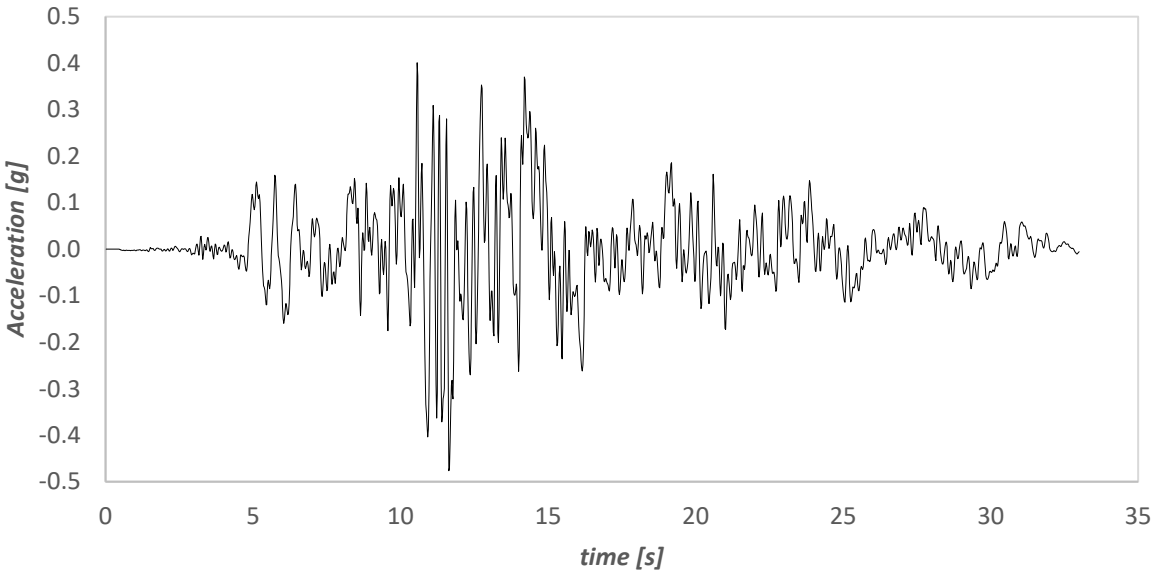

Figure 35. Deconvoluted input motion at z = 112.0 m

6.6.1. Description of Gorini deconvolution process

The *Gorini (2017)* case study involved a soil deposit with a huge depth (*475 m*) and different soil stratums with variable stiffness (*Figure 36*). So, in order to reduce the computational demand on the soil-structure interaction 3D model performed using OpenSees and the PDMY model, he decided to deconvolute the input motion at the depth z = 112 m from a 1D site response analysis using the equivalen-linear sofware MARTA (Callisto, 2020).

This deconvolution procedure was replicated in this thesis work, with Strata (Kottke & Rathje, 2009), to get the deconvoluted input motion (*Figure 35*), using the same geotechnical model (*Figure 36*), that is same shear wave velocity (V_s) profile (*Figure 37*), Modulus Reduction and Damping Curves (MRD) (*Figure 38 & Figure 39*), unit weights (γ) (*Table 9*) and input motion (*RSN143_Tabas*) (*Figure 40 & Table 10*) used by *Gorini (2017)*.

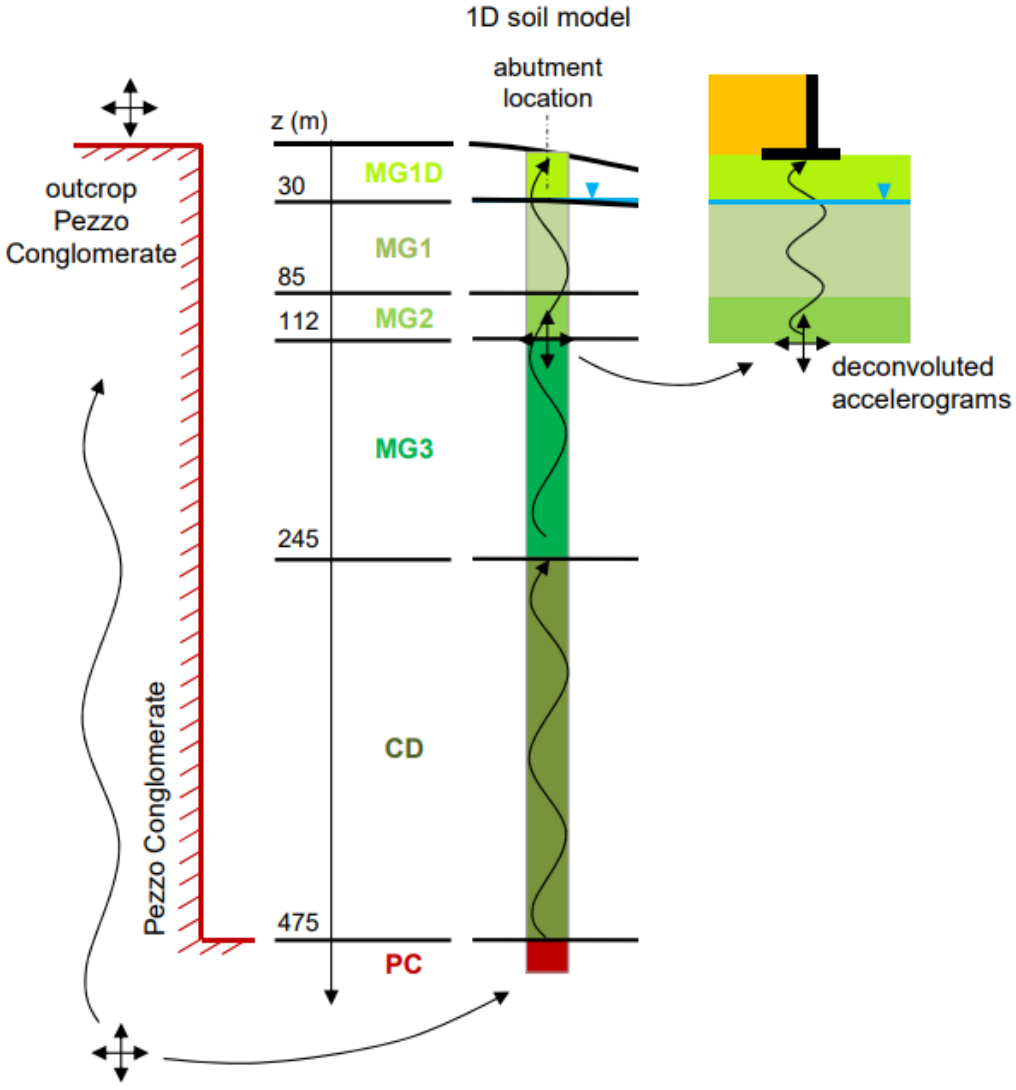

Figure 36. 1D site response analysis performed by Gorini, (2017)

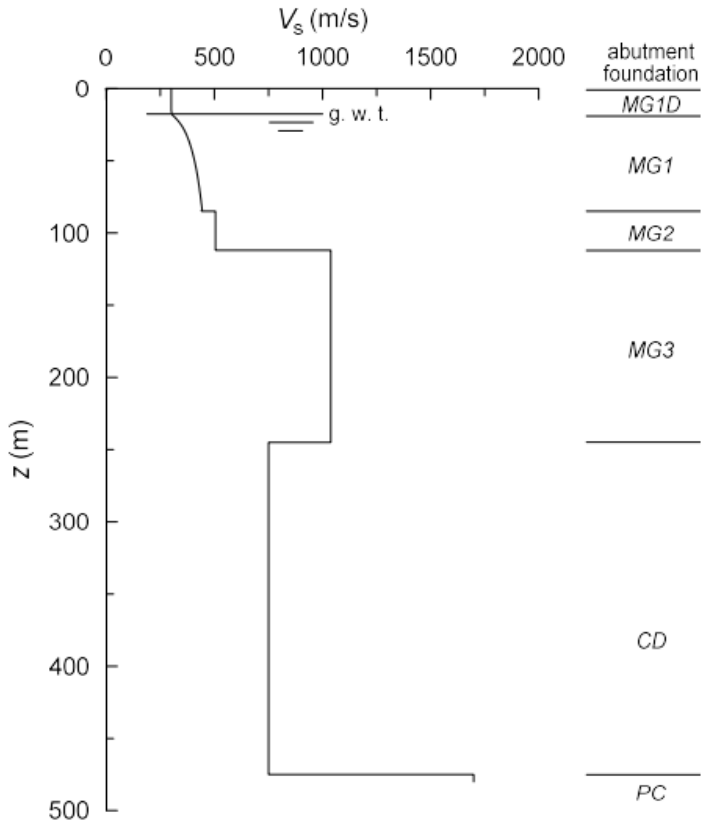

Figure 37. Vs profile of Messina Strait soil stratum

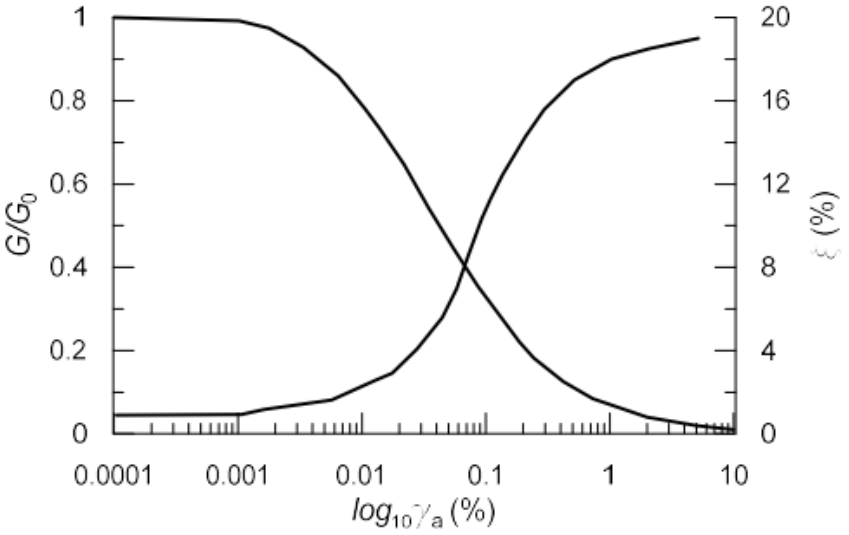

Figure 38, MRD curves adopted for the layers MG1 and MG1D of Messina Gravels (taken from Gorini, 2017)

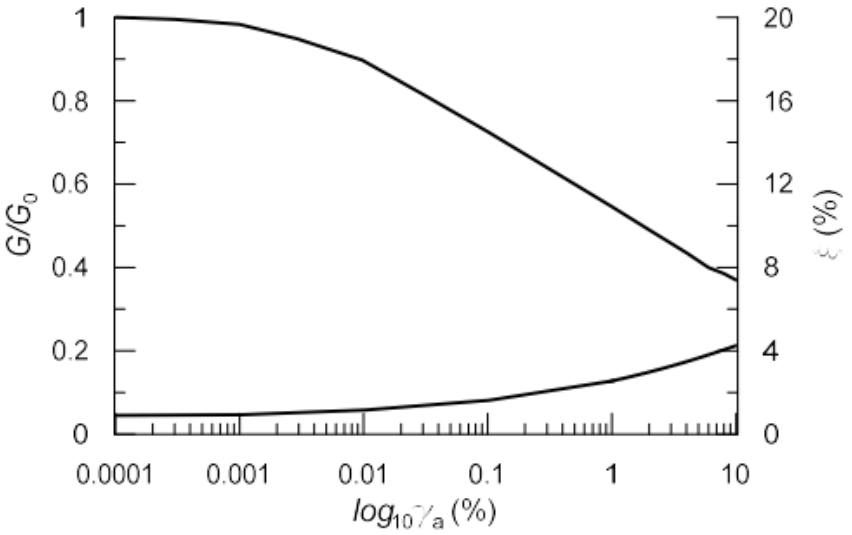

Figure 39. MRD curves adopted for the layers MG2, MG3 and CD (taken from Gorini, 2017)

Table 9. Unit weight of Messina soil stratums

Layer	***Symbol***	$\gamma\ [kN/m^3]$
Messina Gravels 1D	*MG1D*	*19.8*
Messina Gravels 1	*MG1*	*22.0*
Messina Gravels 2	*MG2*	*22.0*
Messina Gravels 3	*MG3*	*22.0*
Continental Deposits	*CD*	*22.0*
Pezzo Conglomerate	*PC*	*23.5*

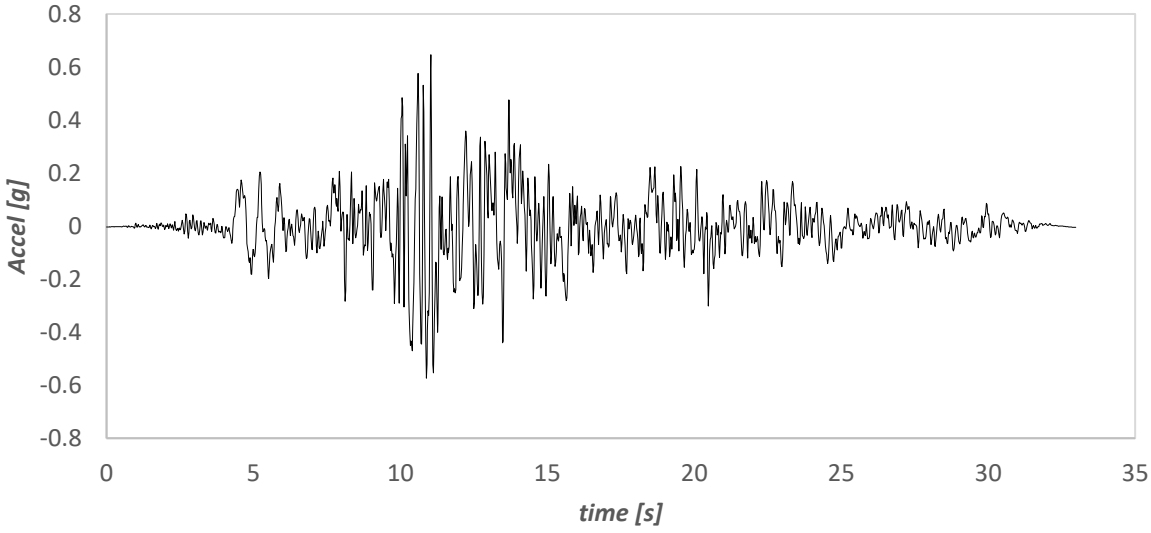

Figure 40. RSN143_Tabas input motion

Table 10. Tabas Event

Event Name	*Tabas (Iran)*
Year	*1978*
Record	*RSN143_TABAS*
Magnitude [M_w]	*7.35*
Component	*FN*
PGA [g]	*0.64*
Scaling Factor	*0.75*

6.6.2. Analysis and Comparison

Using the PDMY model with the parameters presented on *Table 8*, a soil depth $d = 112\,m$ (*Figure 34*), and the obtained deconvoluted input motion (*Figure 35*), the 1D site response analysis is performed on OpenSees. The results of the first gravitational loading step (consolidation stage) and the dynamic response at the free field surface ($z = 0\,m$), compared with the *Gorini* results, are presented on *Figure 41* and *Figure 42* respectively.

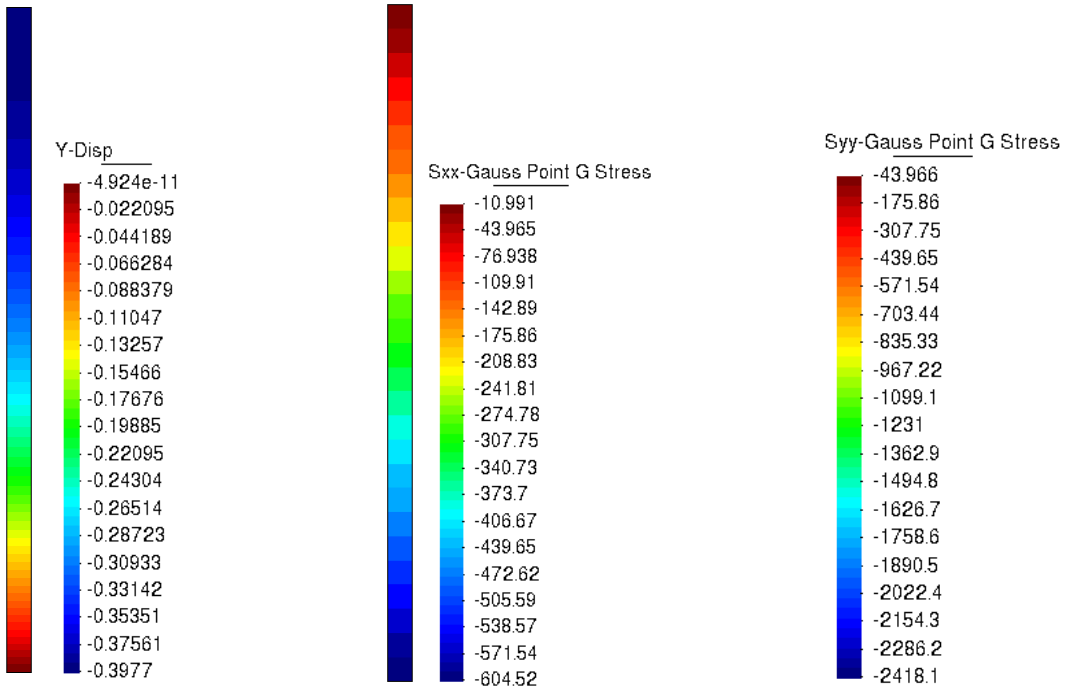

(a) *(b)* *(c)*

Figure 41. 1D gravitational loading results. (a) vertical disp y [m]; (b) horizontal stress σ_{xx}; (c) vertical stress σ_{yy} [kpa]

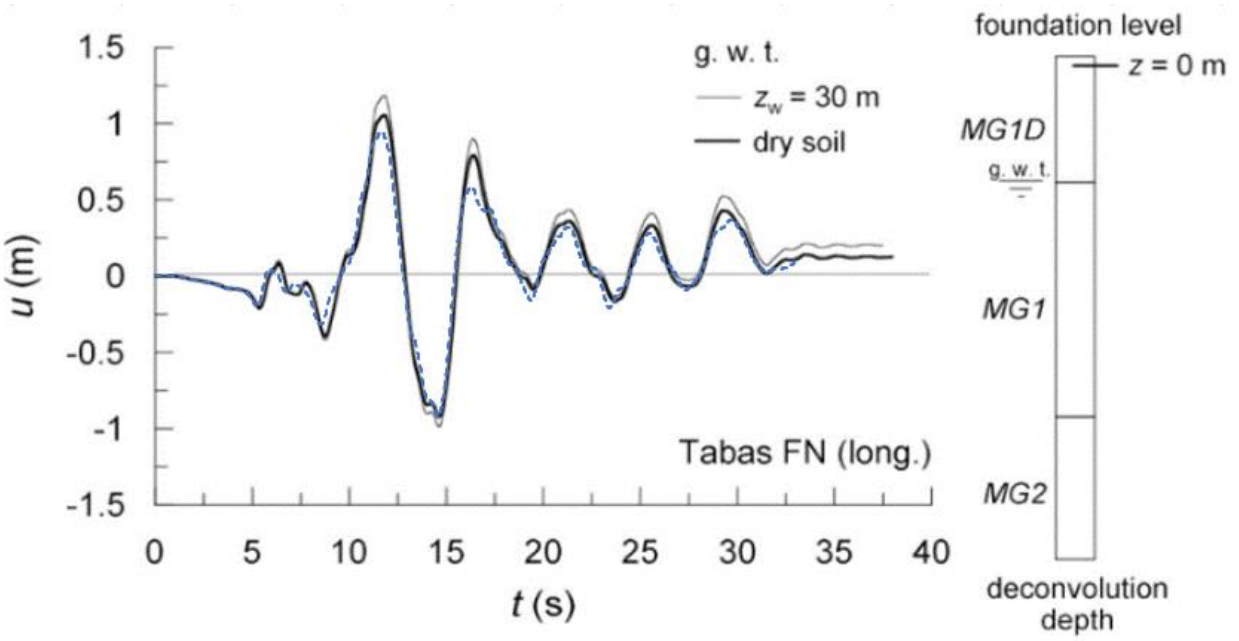

Figure 42. Comparison of displacements at z = 0 m with Gorini's 1D site response analysis (adapted from Gorini, 2017)

It is important to highlight that the Joyner & Chen (1975) approach, to mimic the finite rigidity of the underlying medium, is not used in the Gorini's 1D site response analysis. Indeed, in that case, the input motion is applied in a different way (directly as acceleration time history) assuming that the energy loss because of impedance is already assumed on the deconvoluted input motion (*Figure 36*) (D. Gorini, 2017). So, it makes sense that the displacement given by 1D model is slightly smaller than the Gorini's one (*Figure 42*).

Once the PDMY model was validated in the 1D FEM, this was implemented on the 2D and 3D FEM. The results of the first gravitational loading (*Figure 41, Figure 43 & Figure 44*), compared in *Table 11*, and the subsequent dynamic horizontal loading (*Figure 45*) are in agreement with the 1D FEM model results already validated. This means that the boundary conditions, the input motion and the PDMY constitutive law are correctly used in the three numerical models.

Table 11. Consolidation stage results comparison of the three numerical models

Parameter		*1D FEM*	*2D FEM*	*3D FEM*
disp at top [m] - Δ_v		-0.3977	-0.3977	-0.3977
stress at 112 m depth [kpa]	$\sigma_v = \gamma h$	*2418.10*	*2418.10*	*2417.90*
	$\sigma_h = \frac{\nu}{1-\nu}\sigma_v$	*604.52*	*604.52*	*604.49*

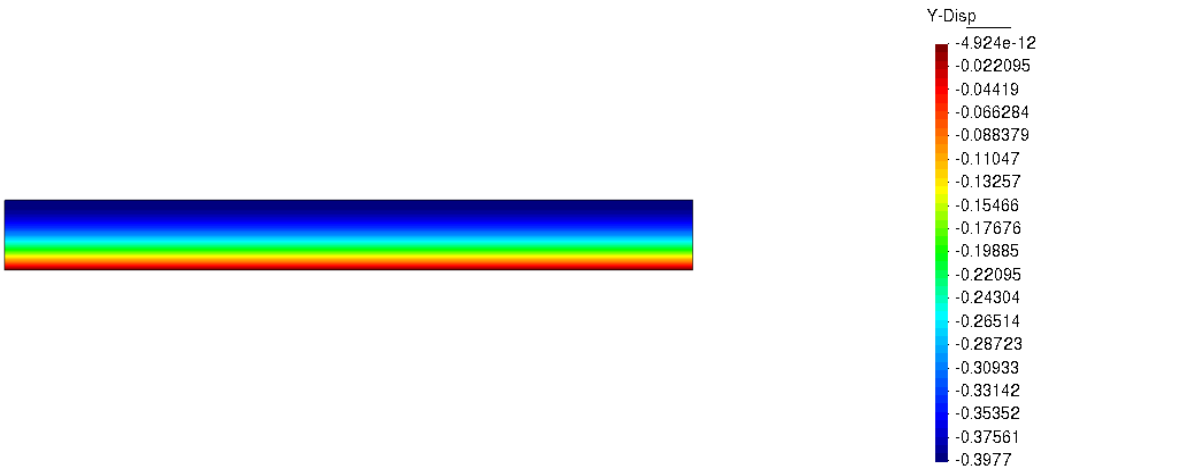

(a)

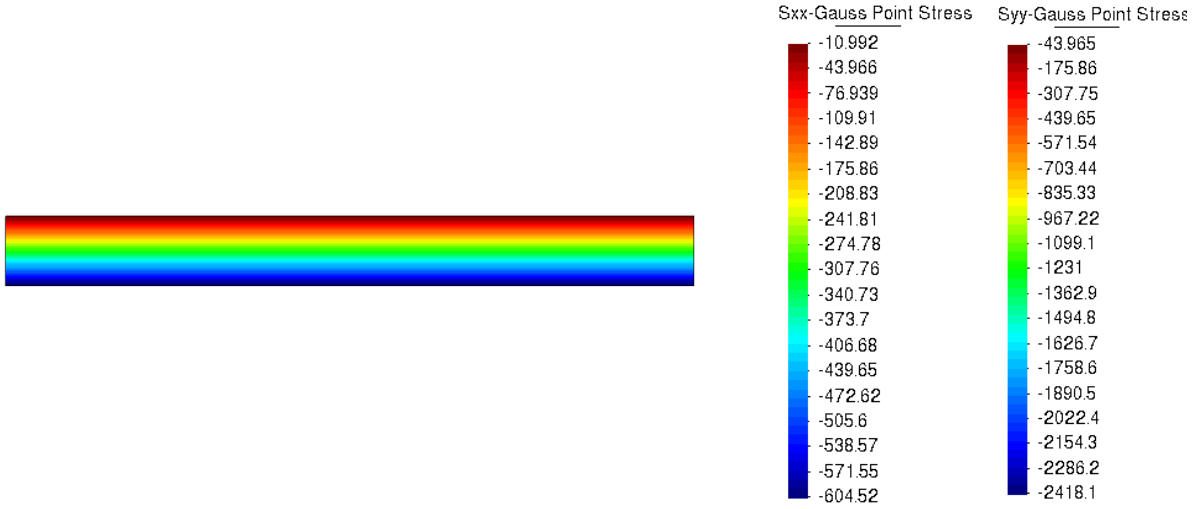

(b)

Figure 43. 2D gravitational loading results. (a) vertical disp y [m]; (b) horizontal σ_{xx} and vertical σ_{yy} stress [kpa]s

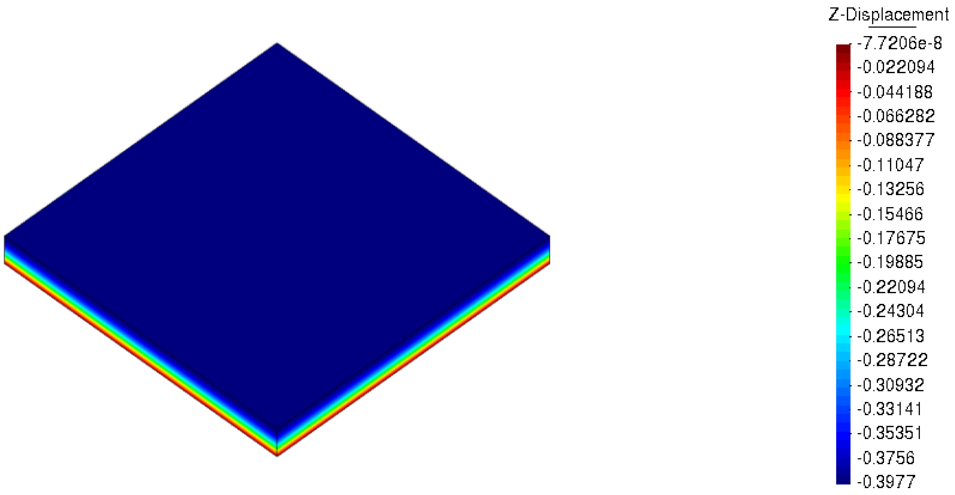

(a)

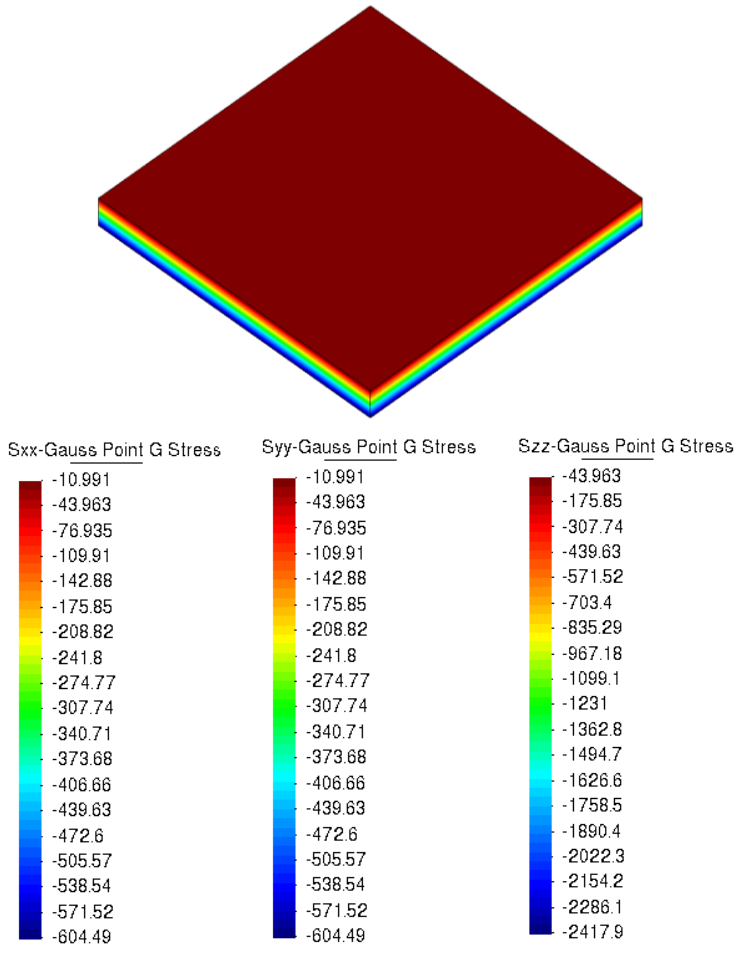

(b)

Figure 44. 3D gravitational loading results. (a) vertical disp y [m]; (b) horizontal $(\sigma_{xx}, \sigma_{yy})$ and vertical σ_{zz} stress [kpa]

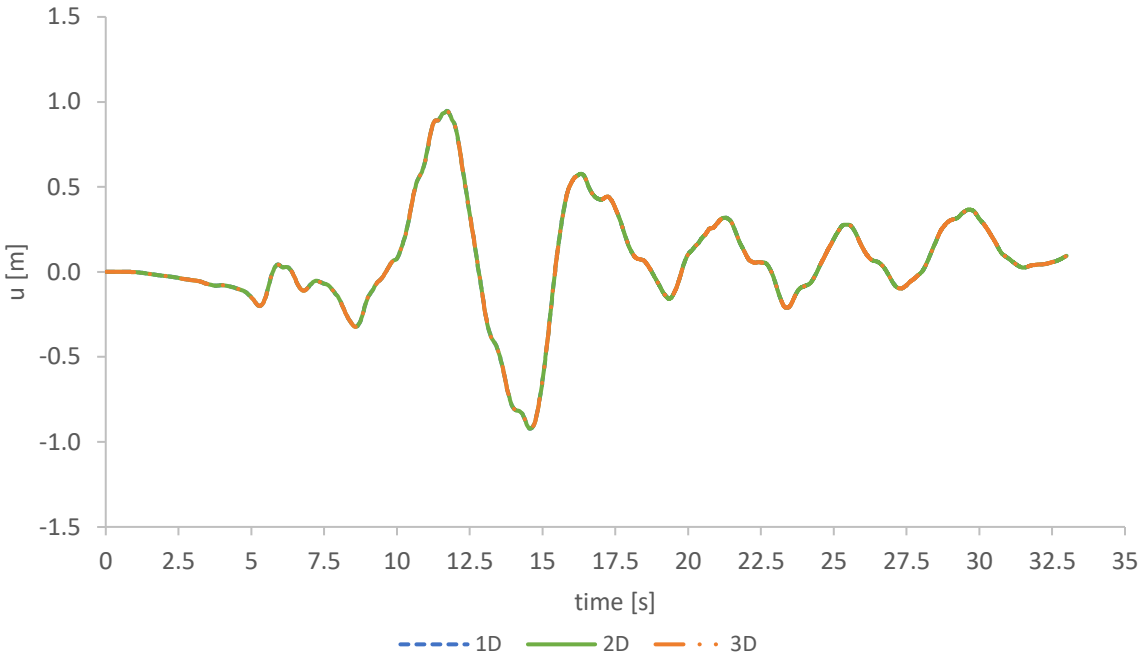

Figure 45. Comparison of displacements of 1D, 2D & 3D FEM using PDMY model

6.6.3. Assessment of soil non-linearity effects

Aiming at studying the response of the PDMY model under different cyclic shear strain ranges, the input motion [Tabas Event] (*Figure 40 & Table 10*) was scaled using 0.01, 0.05, 0.1, and 0.3 as scaling factors (SF). In this way, the transition from elastic regime to elastic-plastic regime could be analyzed and compared with the visco-elastic isotropic (EI) model already validated (*Section 6.5*).

Aiming at guaranteeing that both soil constitutive models under elastic regime are equivalent, the small-strain shear modulus profile (G_0) in the EI model (*Figure 46*) was set to follow the same pressure-dependent rule of the PDMY model (*Eq. 2*).

The analyses were performed first on Strata, using the scaled input motions [corresponding to Tabas Event] and the same geotechnical model of *Gorini (2017)* (*Figure 36*), to get the deconvoluted input motions (associated with each SF) to be used in the 1D site response analysis using the EI and PDMY models. The results are presented and contrasted in *Figure 47* and *Figure 48.*

Looking at the response spectra in *Figure 47,* it can be observed that for SF smaller or equal to 0.05, both the PDMY and EI model matches perfectly, this is because looking at the MRD curves (*Figure 38 & Figure 39*) and at the max shear strain for each SF (*Figure 48*) it can be observed that the soil elastic limit strain is around *0.01*. Such a value corresponds to an SF equal to *0.05*, so for SF smaller or equal to 0.05, the soil behaves under elastic regime. However, when larger SF are used, the soil gets out of the elastic domain and gets into the elastic-plastic domain and the two soil models' responses start to differ.

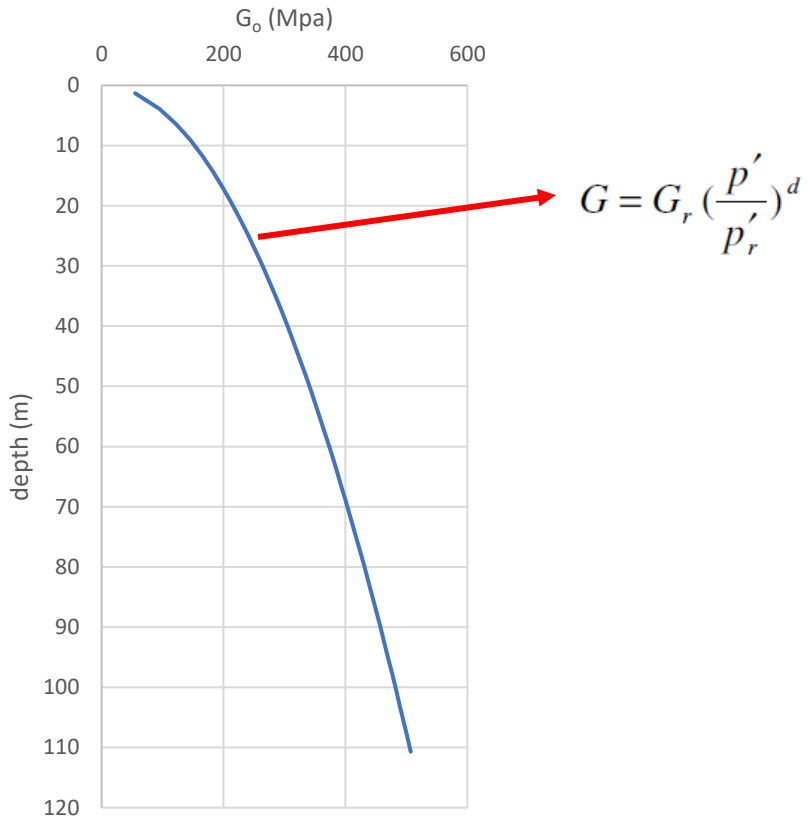

Figure 46. Shear modulus profile used in the Elastic Isotropic Model

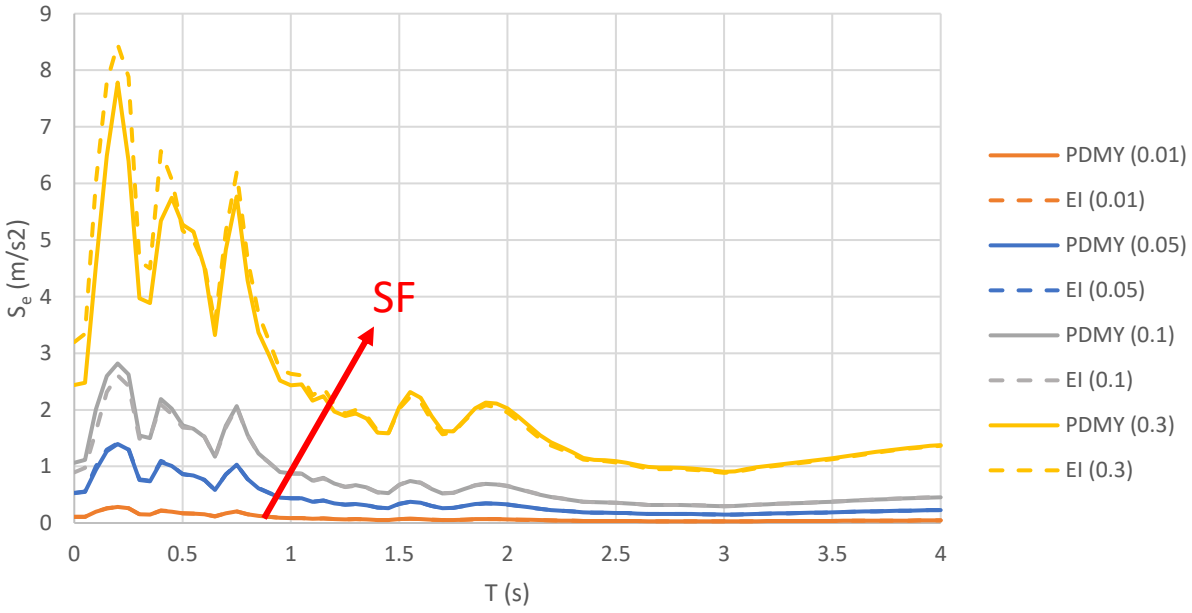

Figure 47. Response spectra at free field (z=0 m) using the PDMY model in the 1D FEM for each deconvoluted input motion associated to each SF

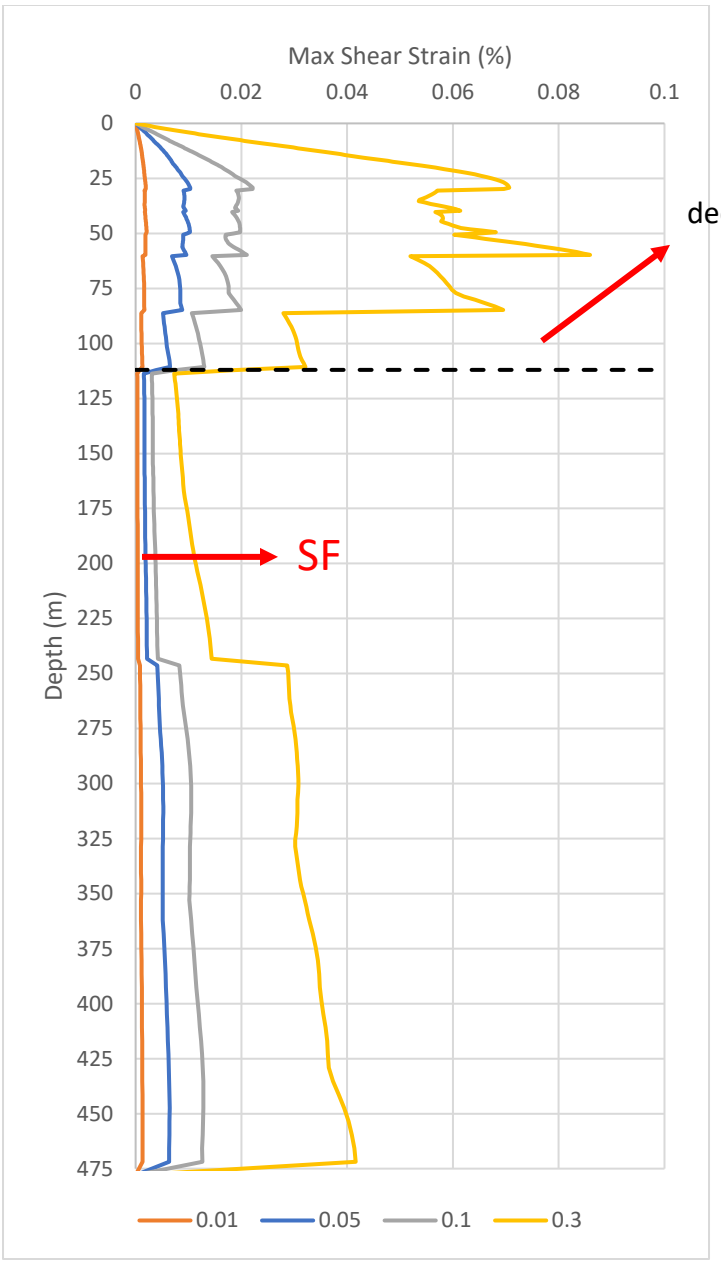

Figure 48. Max shear strain (%) ranges using different scaling factors for the input motion

CHAPTER 7

SOIL-STRUCTURE MODEL

To delve into the impact of scouring on caisson foundations' seismic response, three numerical models were created to simulate the behavior of a not scored (NS Model), general scoured (GS Model) and local scoured (LS Model) soil-caisson-pier system. A brief description of the main components of the soil-structure model encompassing the soil-structure interface, structure model, and soil model. Additionally, it sheds light on the pivotal pushover and free vibration tests that form the backbone of the seismic response analysis discussed in the subsequent chapter.

7.1. Structural Model

The structural model is divided into the caisson model and the pier model (*Figure 49*). The first modeled using rigid-link beam-type elements to consider the caisson as infinity rigid, and the latter modeled using Elastic-Beam-Column-Elements with translational elastic stiffness $K_{pier} = 3.72 * 10^4\ kN/m$.

To simplify the model, the element dynamic masses (M_{pier} & $M_{caisson}$) and the bridge deck mass (M_{deck}), useful for the computation of the eigenvalues and perform the transient analysis (Mazzoni et al., 2006; Zhu, 2023), were defined using nodal mass and applied into the element centroid, in the case of the caisson and pier elements, and in the upper node in the case of the deck (*Figure 49*). The values of the dynamic masses are presented on *Table 12*.

The element self-weight loads were defined in the vertical downward direction multiplying the element gravitational mass (M_{pier} & $M_{caisson-buoyant}$) by *g* (9.8 *m/s*^{2}) and applied like the dynamic masses in the element centroid. Because the caisson is placed below the water table and drained analysis is performed, then the buoyant unit-weight ($\gamma' = \gamma - \gamma_w$) is used to compute the caisson buoyant self-weight. This assumption is just valid for the gravitational loading and not valid for dynamic loading which uses the total caisson mass ($M_{caisson}$) in the dynamic analysis. The deck gravitational load was defined in a similar way, multiplying the deck mass (M_{deck}) by *g*, and applied in the upper node like the deck dynamic mass.

Table 12. Masses of the structural elements

Parameter	*Value*
M_{pier}	*462.44 Mg*
$M_{caisson}$	*1256.64 Mg*
$M_{caisson-buoyant}$	*753.98 Mg*
M_{deck}	*1440 Mg*

For simplicity, the P-δ second-order (nonlinear) effect, induced by the gravitational loads of the pier and the deck, is omitted from the model to streamline computational demands. It's worth noting, as will be discussed in *Section 7.6*, that the static P-δ effect is not particularly significant for this specific case study.

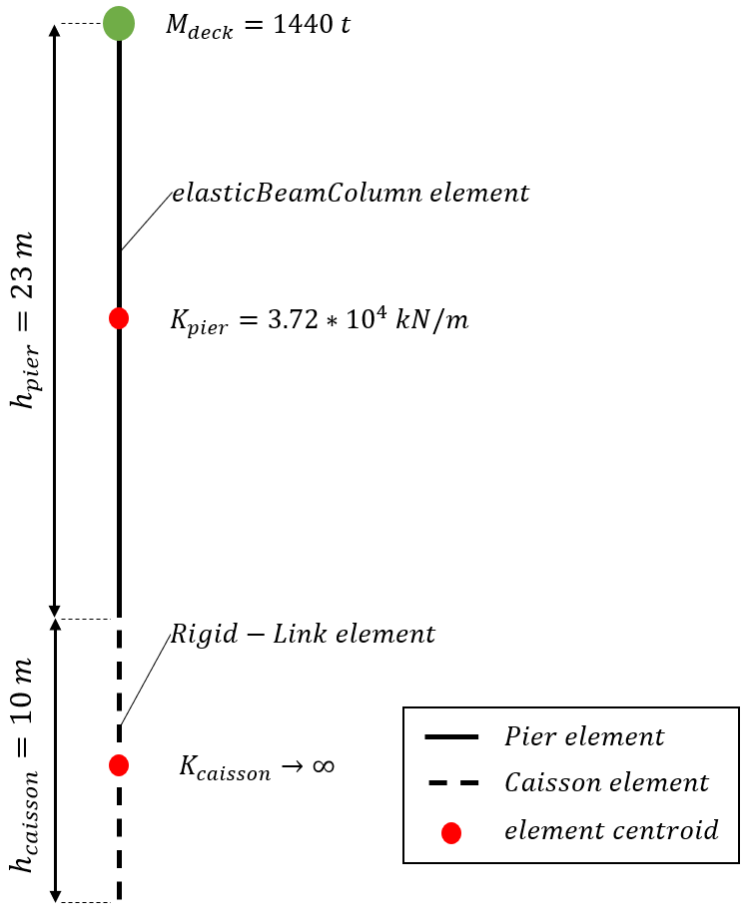

Figure 49. Caisson-Pier model

7.2. No Scoured Caisson Foundation Model – NS Model

Aiming at modeling a fully drain response of the soil, the soil unit weigh ($\gamma_{soil} = 22.0\ kN/m^3$) was changed by the soil buoyant unit weight ($\gamma'_{soil} = \gamma_{soil} - \gamma_w = 12.18\ kN/m^3$). This doesn't affect the behavior of the soil constitutive law (PDMY model) but just affect the stress-strain state into the soil model both during the consolidation and dynamic analyses.

The depth of the soil model was defined equal to 33.0 m and the horizontal soil model size (*x-y directions*) was set as $11 \times \phi_{caisson}$ (*88.0 m*), that is the boundaries are $5 \times \phi_{caisson}$ far from the caisson position, this was done to guarantee Free Field (FF) Conditions at the model boundaries (*Figure 50*).

The meshing was performed with the software Abacus (Dassault Sysèmes, 2023) using structured meshing with eight-nodes brick-elements, which into OpenSees has been defined as

SSPbrick elements (*Figure 28*). The same settings of the 3D Soil FEM (i.e., Rayleigh damping, dashpots, dynamic shaking forces and CFL condition), discussed on *Chapter 6*, has been imposed into this numerical model.

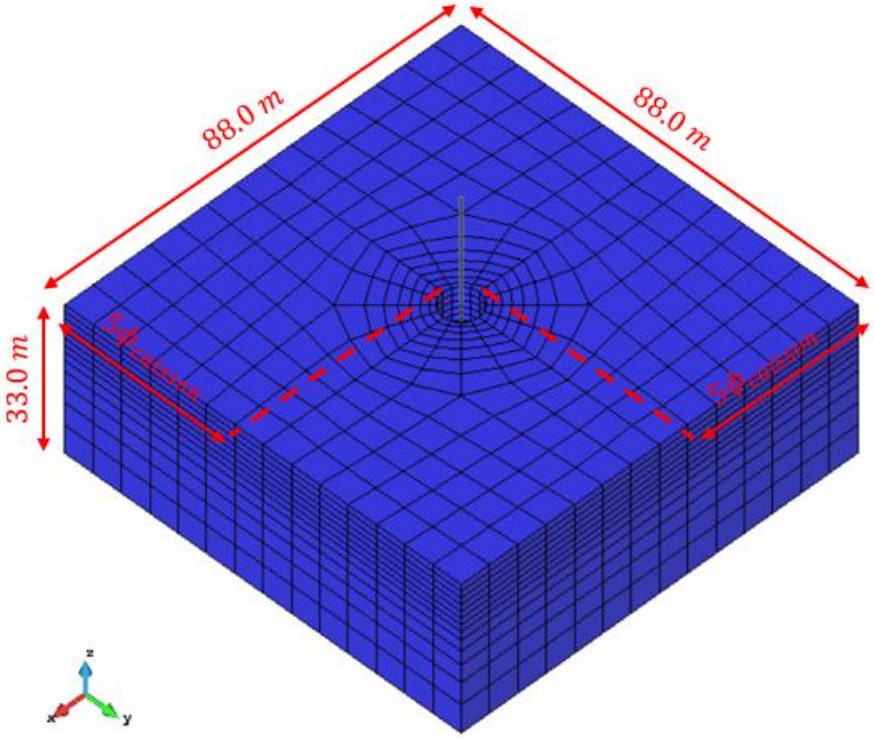

Figure 50. Unscoured Caisson Foundation - Pier - Deck Model

7.2.1. Soil-Structure Interface

The soil-structure interface was modeled using rigid-link elements that connect the caisson rigid-link elements with the soil brick elements through overlapped nodes which share equal translational DOFs with the soil nodes (*Figure 51*).

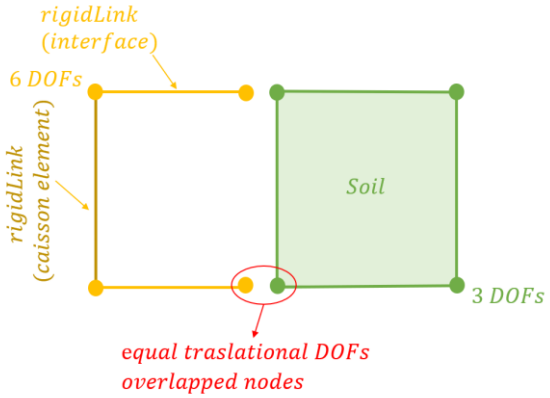

Figure 51. Schematization of soil-structure interface

The overlapped nodes are used because the rigid-links are beam-type, that means these types of elements constraint six degrees of freedom at the connected nodes (Mazzoni et al., 2006), and the soil brick-element nodes just have three translational DOFs, so the use of "fictitious" overlapped nodes with six DOFs is compulsory to connect the soil nodes with the rigid-links nodes by setting equalDOF at the three translational DOFs.

The use of a soil-thin interface layer (*Figure 52*), to describe the strain concentration occurring in the soil in close proximity to the structural elements and mimic the frictional behavior at soil-structure interface (Jeremić et al., 2009; Domenico, 2021), is not considered into the model because besides the advantages of using interface solid elements their effect is negligible on the dynamic response of the global system (Gorini, 2017).

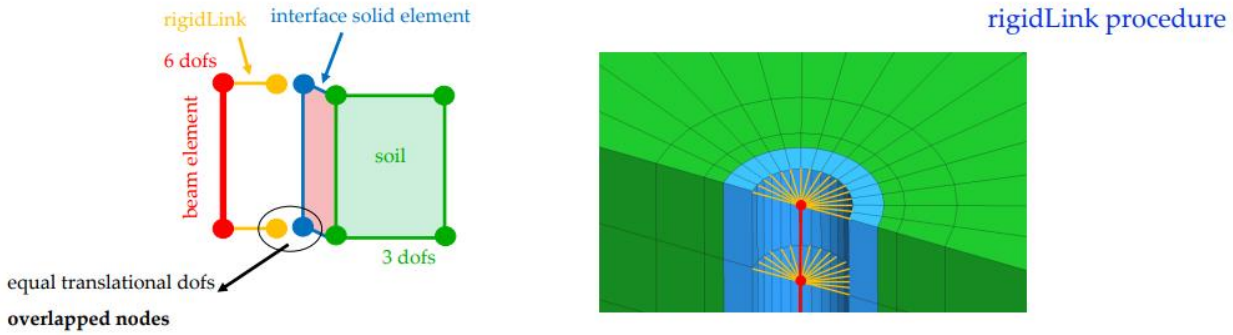

Figure 52. soil-structure interface using an interface solid element (taken from Gorini et al., 2021)*)*

The final configuration of the mesh, that is the soil brick elements (blue), pier elastic-beam-column elements (black), and caisson (green) and interface (magenta) rigidLink elements, is presented in *Figure 53*. Notice that the embedded depth of the caisson (D) is just $\frac{9}{10}h_{caisson}$.

Aiming at validating that the soil-structure interface works property, the soil constitutive law of the soil was changed by an EI model ($E = 3.38 \times 10^5\ kpa\ ;\ \nu = 0.3\ ;\ \rho = 2.243\ Mg/m^3$), and three pushover static tests in the two orthogonal and vertical directions were performed. The numerical results are in agreement with the Gazeta's analytical solution (*Table 1 & Table 2*). This comparison is presented below in *Table 13*.

Table 13. Comparison of Pushover results between Numerical Model and Gazetas Solution

Forces [kN]			***Displacements [m]***					
			Numerical Model			***Gazetas Solution***		
Fx	***Fy***	***Fz***	***u***	***v***	***w***	***u***	***v***	***w***
10000	*0*	*0*	*0.00126*	*≈ 0.0*	*≈ 0.0*	*0.00126*	*0.0*	*0.0*
-10000	*0*	*0*	*-0.00126*	*≈ 0.0*	*≈ 0.0*	*-0.00126*	*0.0*	*0.0*
0	*10000*	*0*	*≈ 0.0*	*0.00126*	*≈ 0.0*	*0.0*	*0.00126*	*0.0*
0	*-10000*	*0*	*≈ 0.0*	*-0.00126*	*≈ 0.0*	*0.0*	*-0.00126*	*0.0*
0	*0*	*-10000*	*≈ 0.0*	*≈ 0.0*	*-0.00128*	*0.0*	*0.0*	*-0.00128*

u, v & w : displacements in x , y & z directions respectively
Fx , Fy & Fz : Pushover static forces applied in x , y & z directions respectively

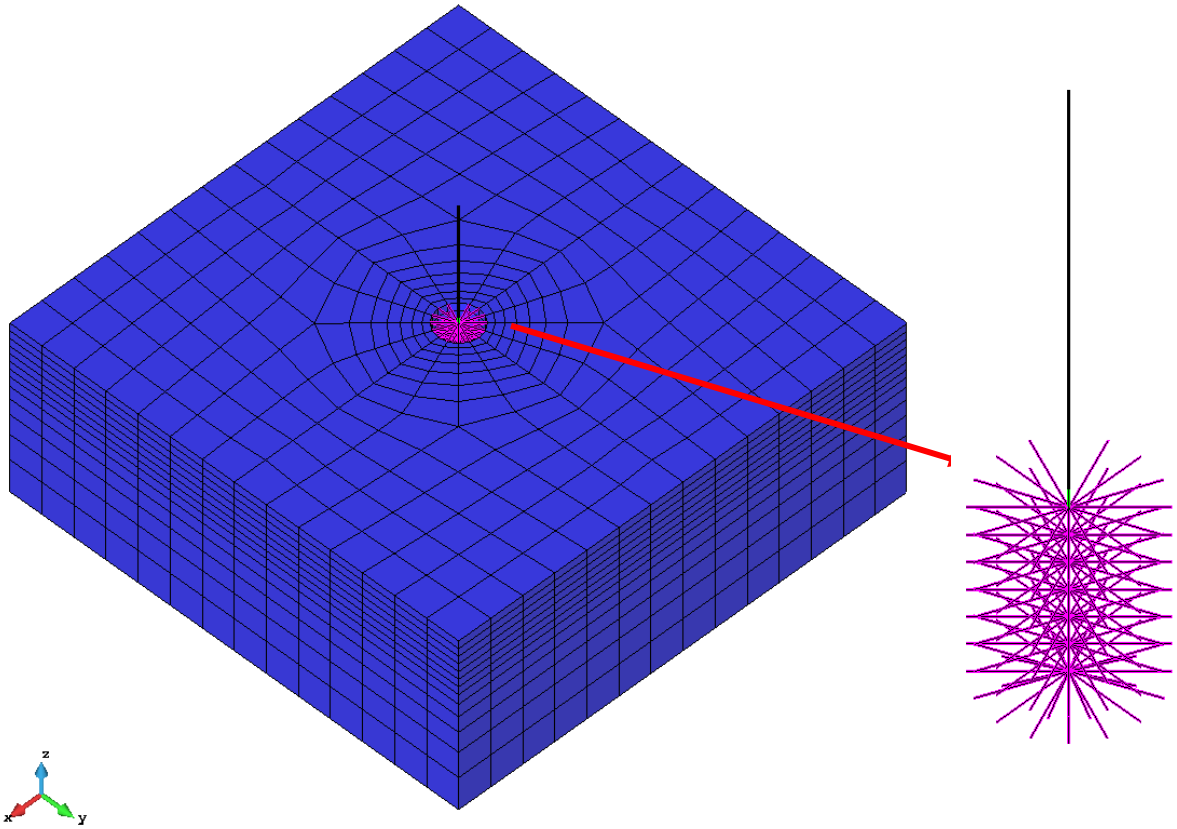

(a)

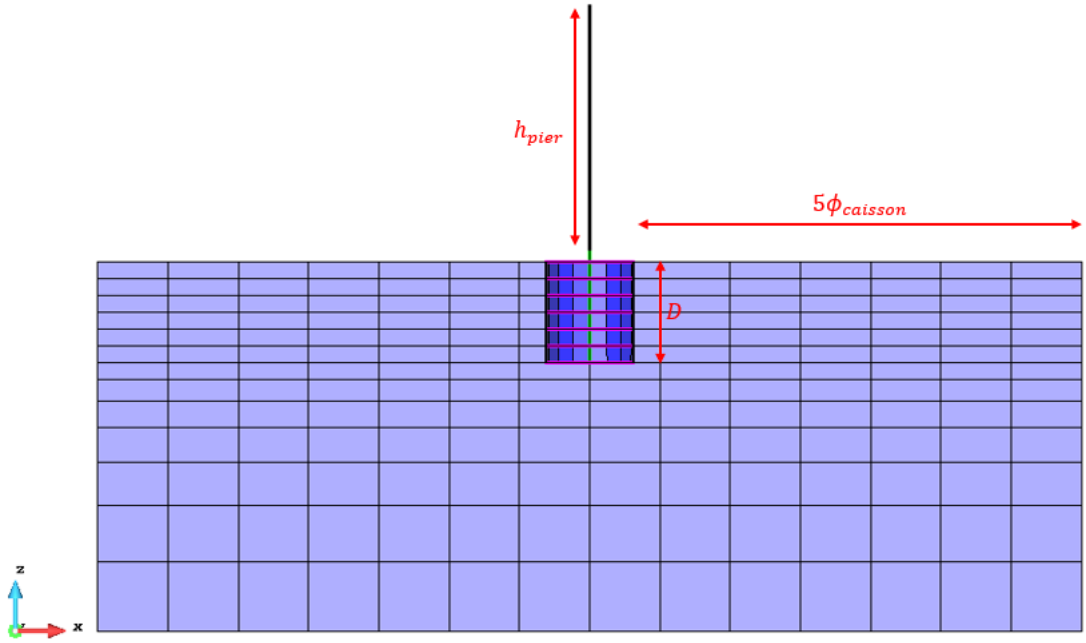

(b)

Figure 53. No scoured caisson foundation model mesh, black - Pier Elements, green - Caisson Elements, Magenta - rigidLinks. (a) 3D view ; (b) cross section

7.2.2. Base Dashpots and Input Dynamic Force

Following the approach of *Joyner & Chen, (1975) & Lysmer, (1978)*, the centroids of the base surface soil elements has been computed (*Figure 54*) and joined such a way to compute the areas associated to each base soil nodes (*Figure 55*), useful to compute both the input dynamic forces (*Eq. 10*) and the base dashpot coefficients (*Eq. 11*) to apply to each of the base soil nodes and guarantee the proportional impedance and dynamic loading (Joyner & Chen, 1975; Lysmer, 1978; C. McGann & Arduino, 2011). This procedure has been performed using MATLAB (MathWorks, 2023).

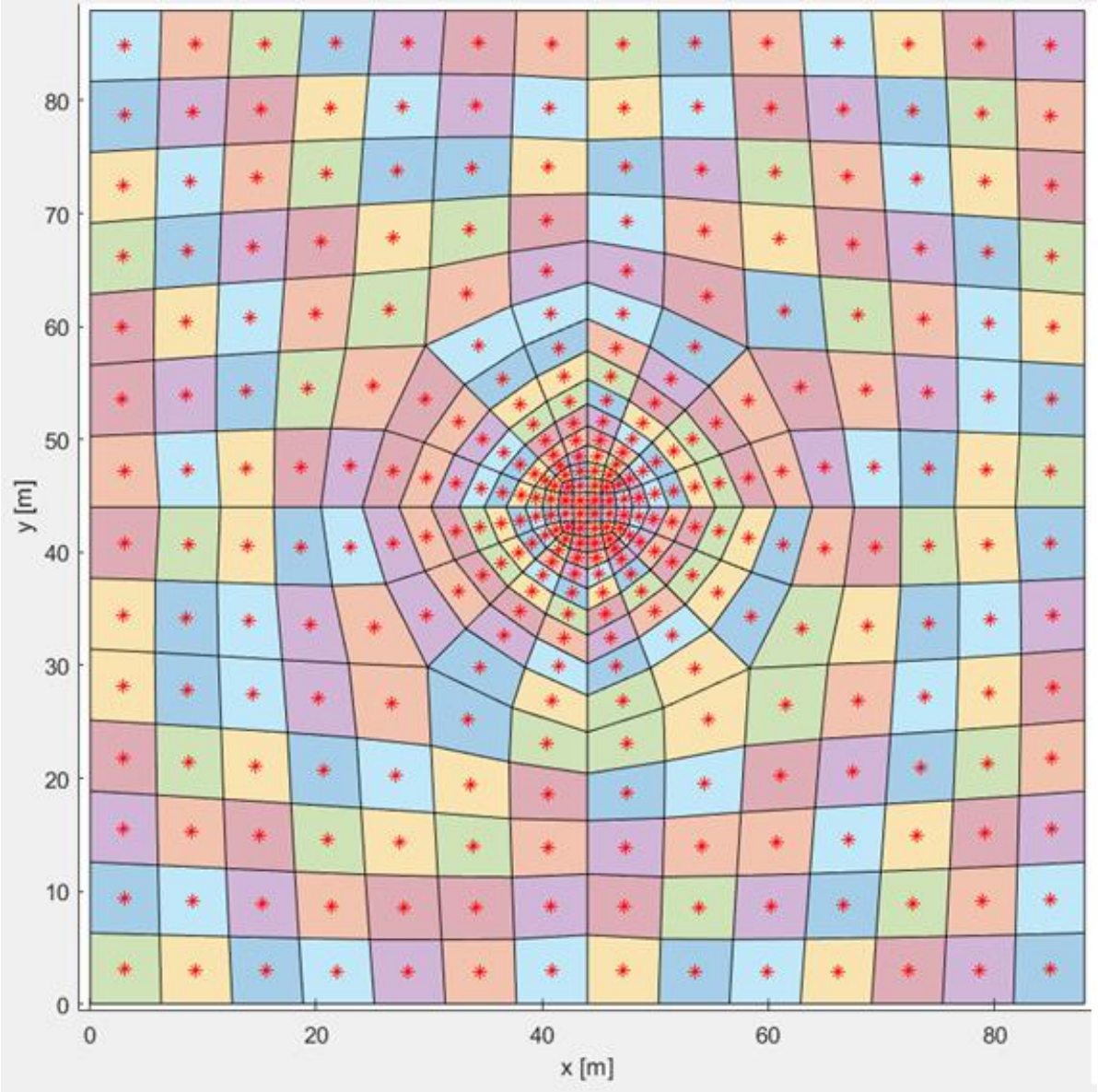

Figure 54. Centroid of the base surface soil elements

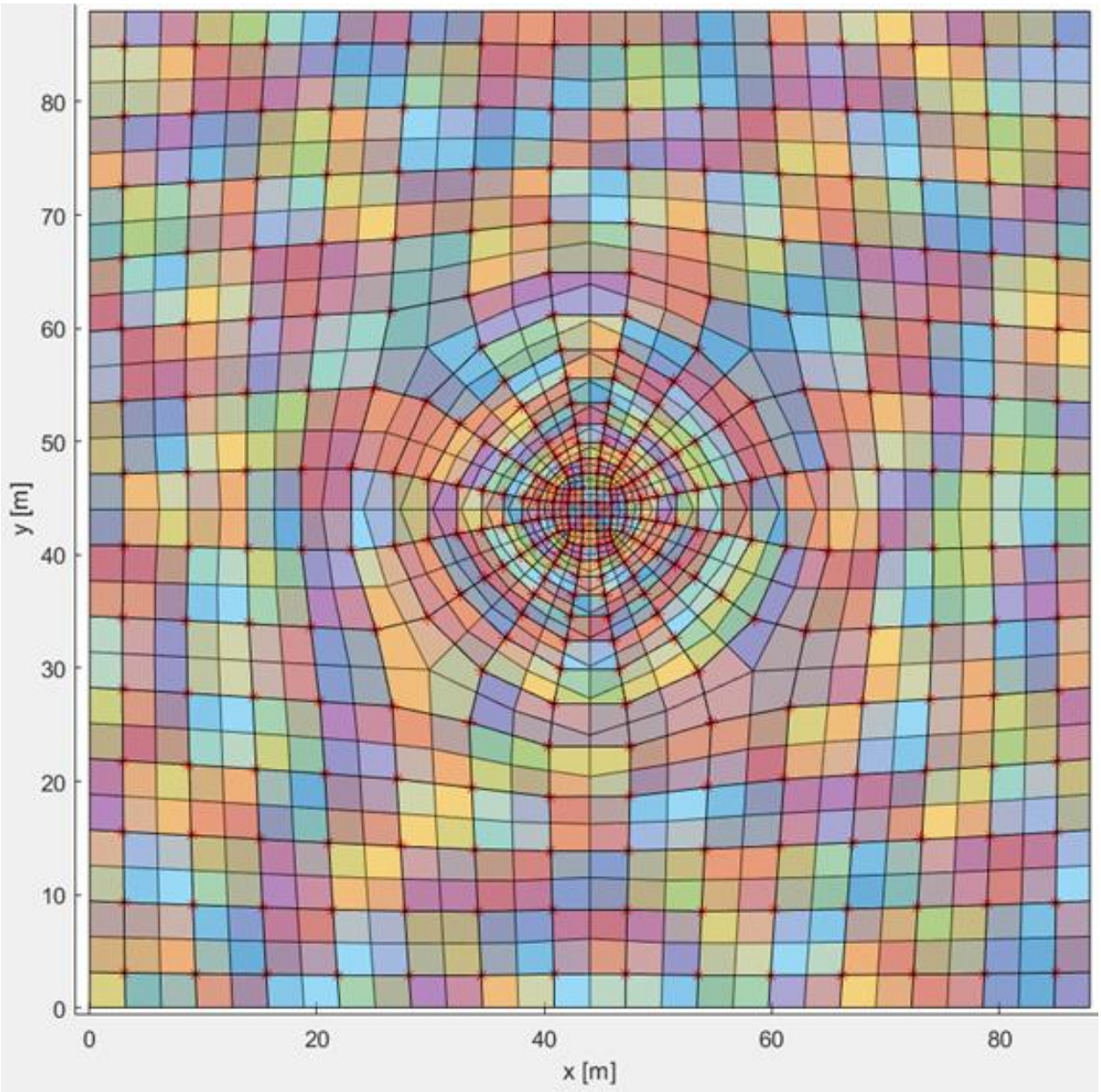

Figure 55. Base areas associated to each of the base soil nodes

7.3. General Scoured Caisson Foundation Model – GS Model

The General Scoured Caisson Foundation Model (GS Model) was created based on the No Scoured Caisson Foundation Model mesh (*Figure 53*) and settings, presented above (*section 7.2*), but taking out four meters depth of the soil to simulate the general scouring (*Figure 10a*), that is a half of the caisson depth is embedded ($D = \frac{1}{2} h_{caisson}$). The final soil mesh, structure and interface elements, are presented on *Figure 56*.

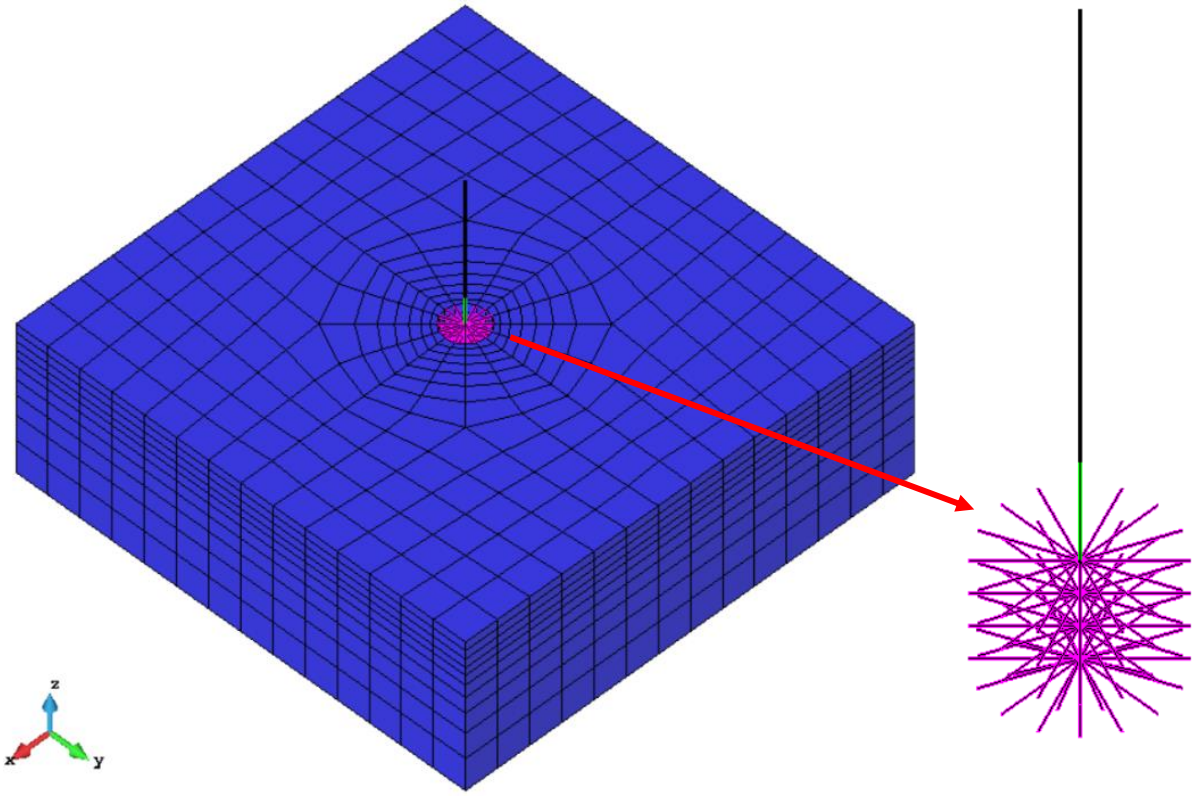

(a)

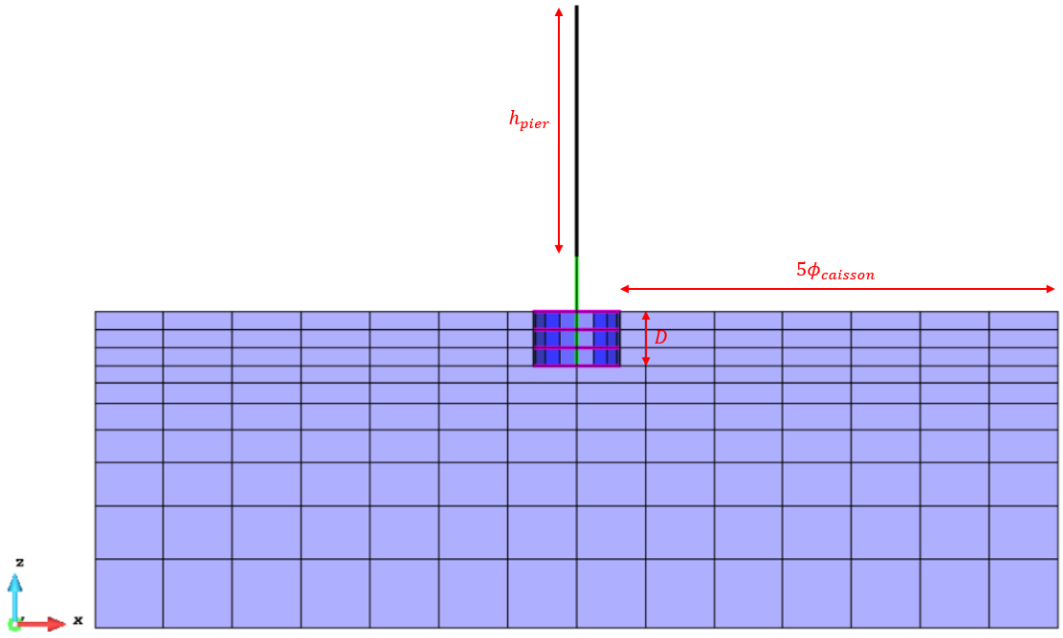

(b)

Figure 56. General scoured caisson foundation model mesh, black - Pier Elements, green - Caisson Elements, Magenta - rigidLinks. (a) 3D view ; (b) cross section

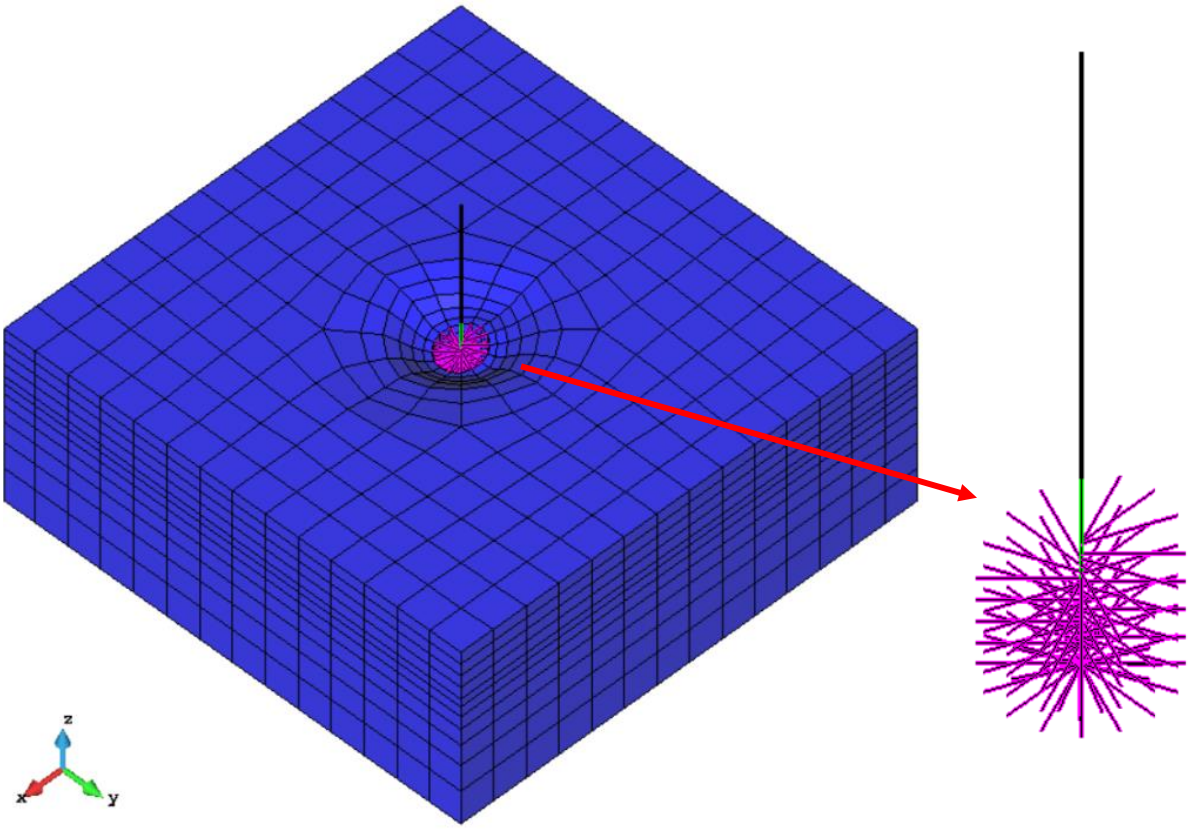

(a)

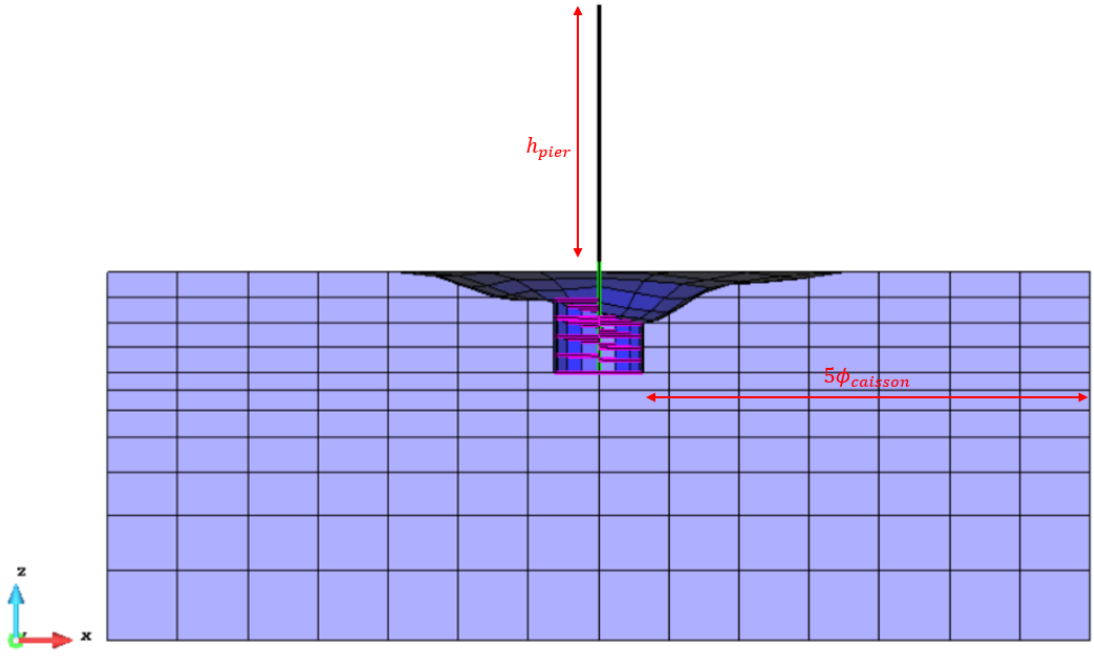

(b)

Figure 57. Local scoured caisson foundation model mesh, black - Pier Elements, green - Caisson Elements, Magenta - rigidLinks. (a) 3D view ; (b) cross section

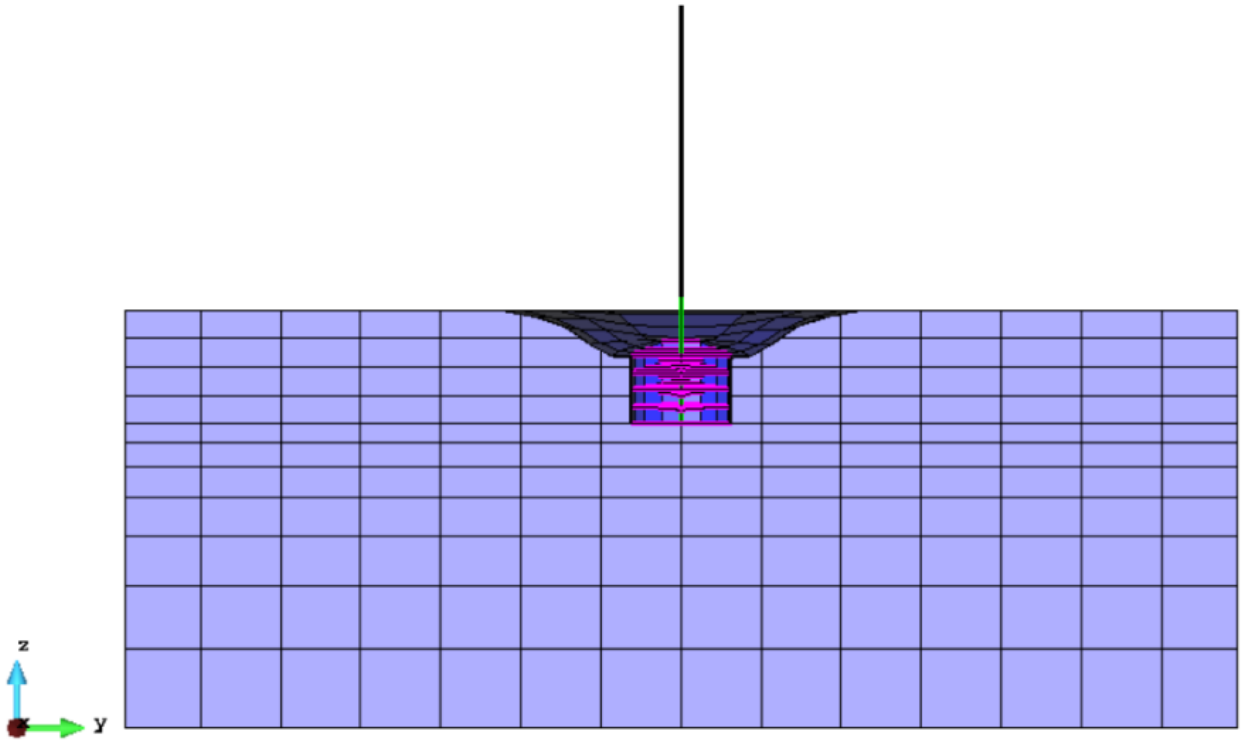

(a)

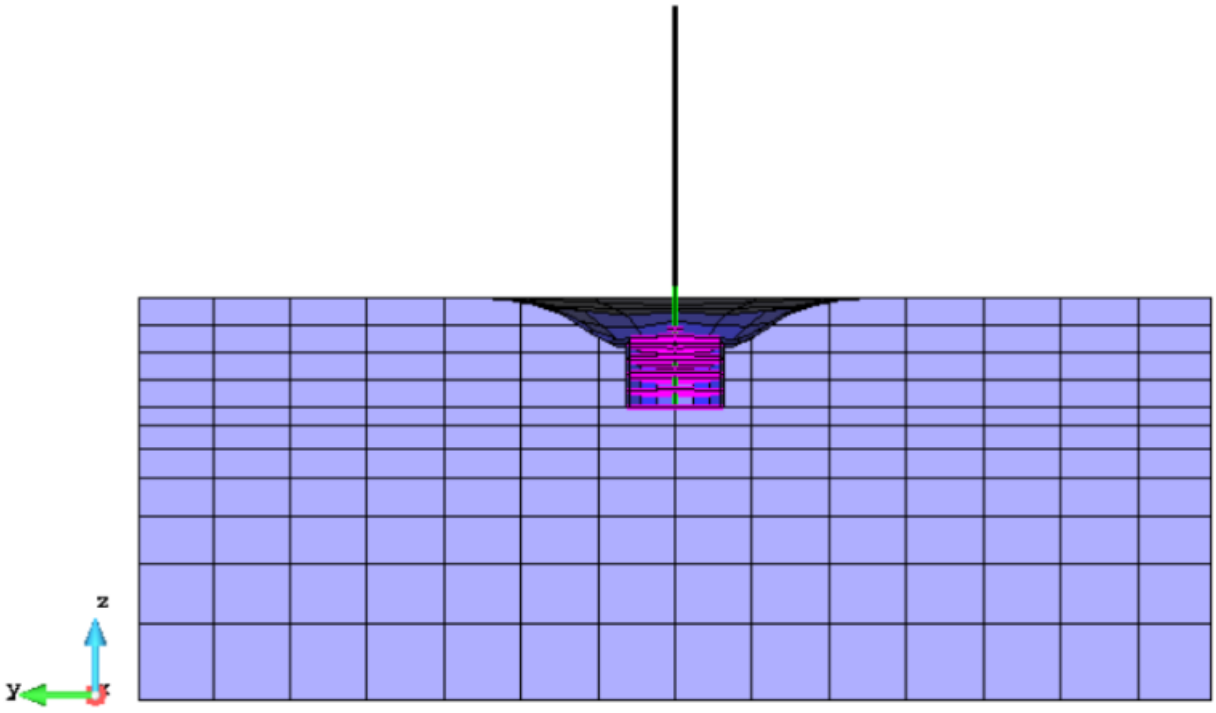

(b)

Figure 58. Cross Section of the Scoured Model; (a) z-y plane direction x+ ; (b) z-y plane direction x

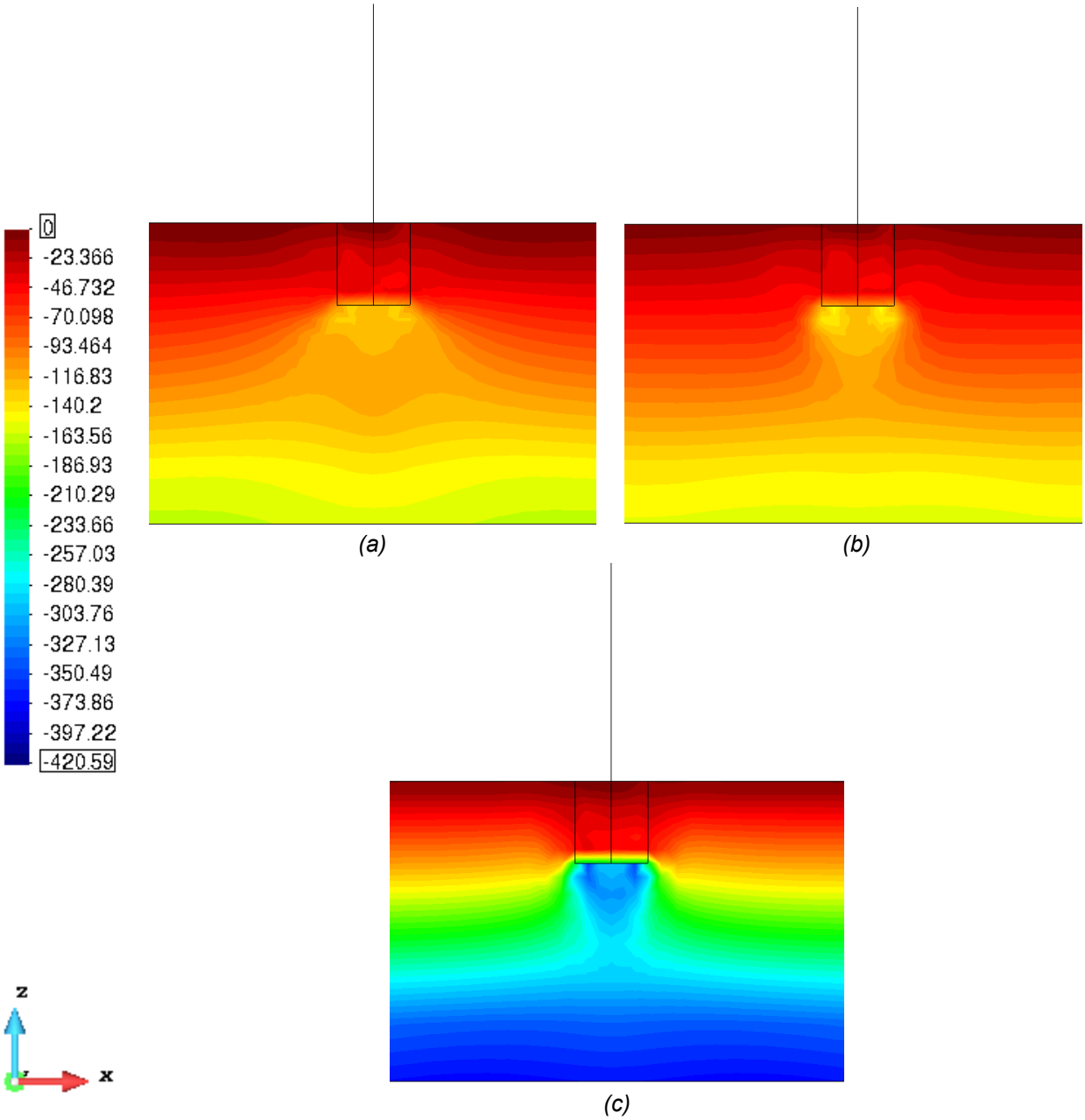

Figure 59. Initial stress state for NS model [kpa]; (a) σ_{xx} , (b) σ_{yy} and (c) σ_{zz}

7.4. Local Scoured Caisson Foundation Model – LS Model

Considering the experimental local scouring shape of the soil surrounding the caisson foundation found by Ciancimino et al., 2022a (*Figure 11*), the structured mesh of the soil was created using the software Abacus (Dassault Sysèmes, 2023) (*Figure 57*). Notice that on the most scoured part of the pile (right side) $D = \frac{1}{2} h_{caisson}$, equal to the general scoured case, and on the less scoured part (left side) $D = 0.65\, h_{caisson}$. Because the scouring morphology is symmetric to the *x-z plane*, *Figure 58* shows the scoured shape of the hole in the z-y planes in direction x+ and x-.

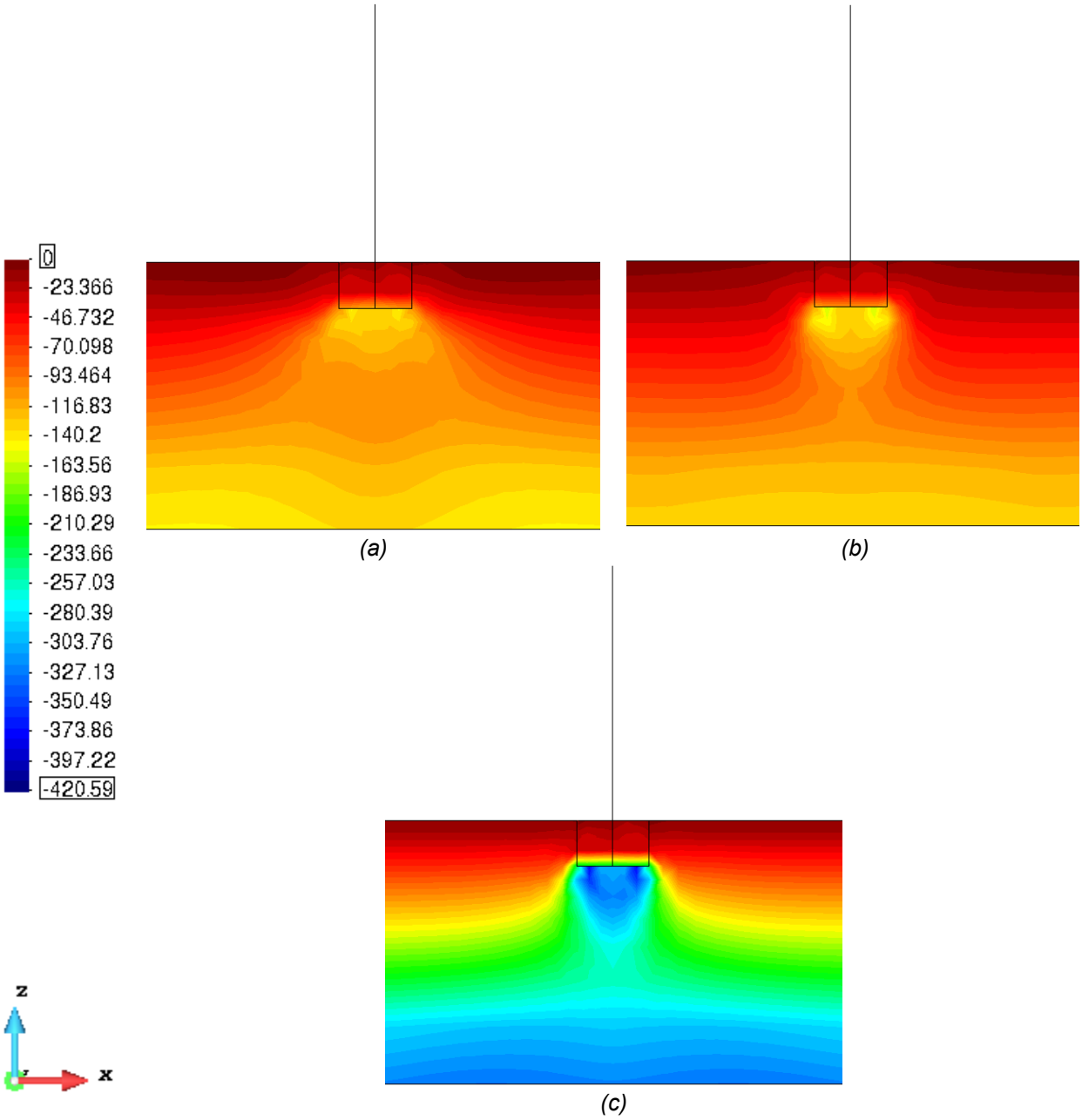

Figure 60. Initial stress state for GS model [kpa]; (a) σ_{xx} , (b) σ_{yy} and (c) σ_{zz}

7.5. Consolidation Stages

The initial stress-strain state into the soil model was assessed through two gravitational loading steps. The first one considering just the soil elements weight and the second one considering the self-weigh of the structure (caisson & pier) and the deck.

These first two consolidation stages are useful not just to assess the initial stress-strain state but also to compute the initial displacements that must be subtracted from the dynamic displacements results.

The computed initial stress-state for the three models, NS, GS & LS, are presented in *Figure 59, Figure 60 & Figure 61,* respectively. Notice that for comparison purposes the same color scale has been used.

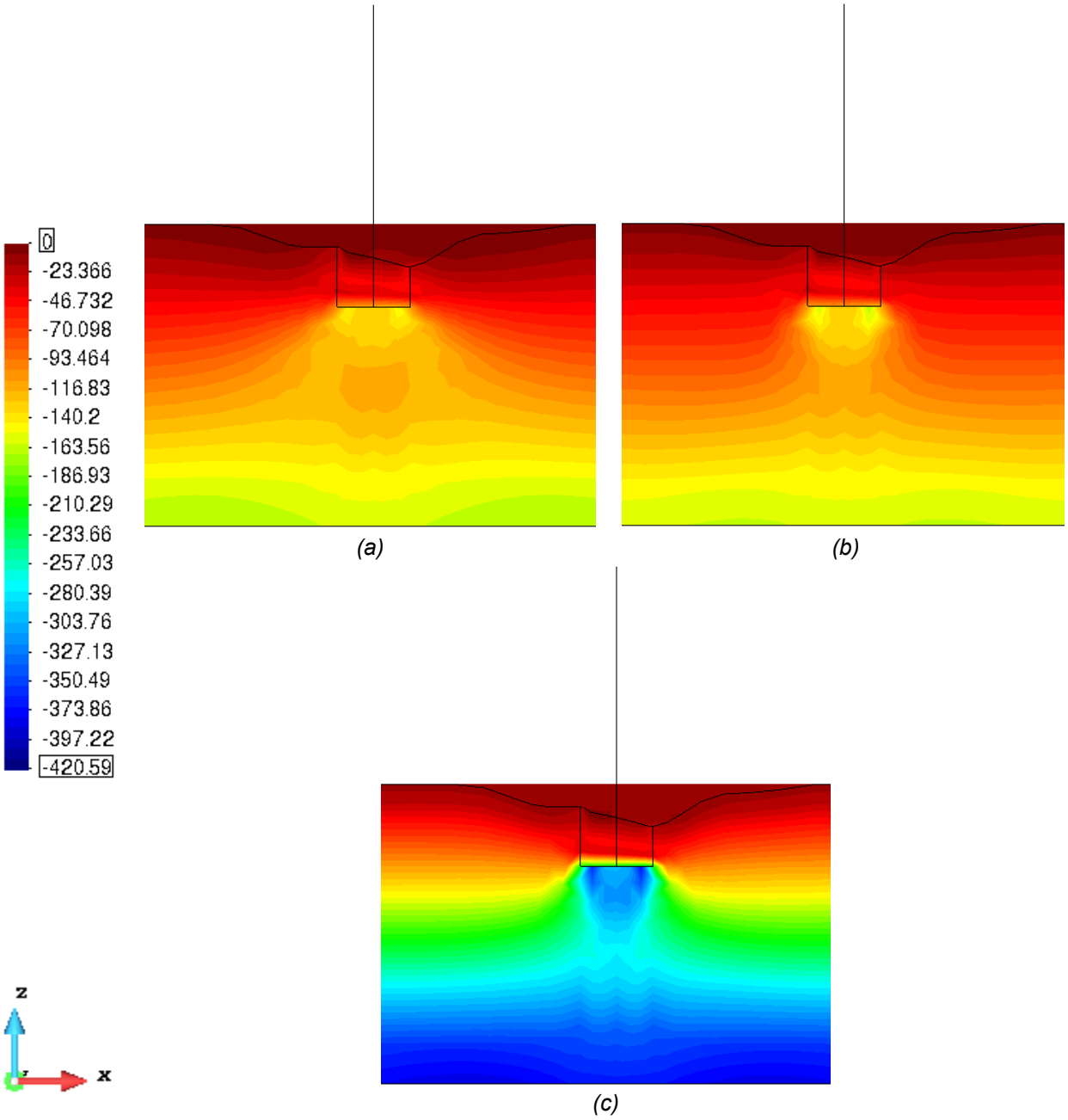

Figure 61. Initial stress state for LS model [kpa]; (a) σ_{xx} , (b) σ_{yy} and (c) σ_{zz}

7.6. Pushover analysis

Before diving into dynamic analyses, it is crucial to address the impact of P-δ second-order effects on the pier-caisson-soil system's overall response. This evaluation is pivotal for deciding

whether to integrate these effects into the numerical model and to study the influence of scour on the relevance of such effect. This assessment is conducted through pushover tests, which are detailed in this section.

The pushover test, also known as pushover analysis or nonlinear static analysis, is a structural analysis method employed to evaluate the seismic performance of a structure (FEMA, 2000), such as a bridge pier. The test involves applying a series of lateral forces or displacements to the structure, typically in a monotonically increasing manner, until a predefined performance or failure criteria are reached (Chopra, 2005). The purpose is to assess the structure's capacity and deformation characteristics under lateral loads, providing valuable insights for seismic design and retrofitting strategies (Priestley et al., 1996).

A displacement control analysis with an increment step of *0.01 m* is used to carry out the pushover tests. The controlled displacement (u) is applied at the deck in the *x[+]-direction (Figure 62)*. The results are presented in terms of the acting horizontal force at the deck (F_x), the external moment generated: $M_E = F_x * h_{pier}$, the caisson rotation (ϑ), and u.

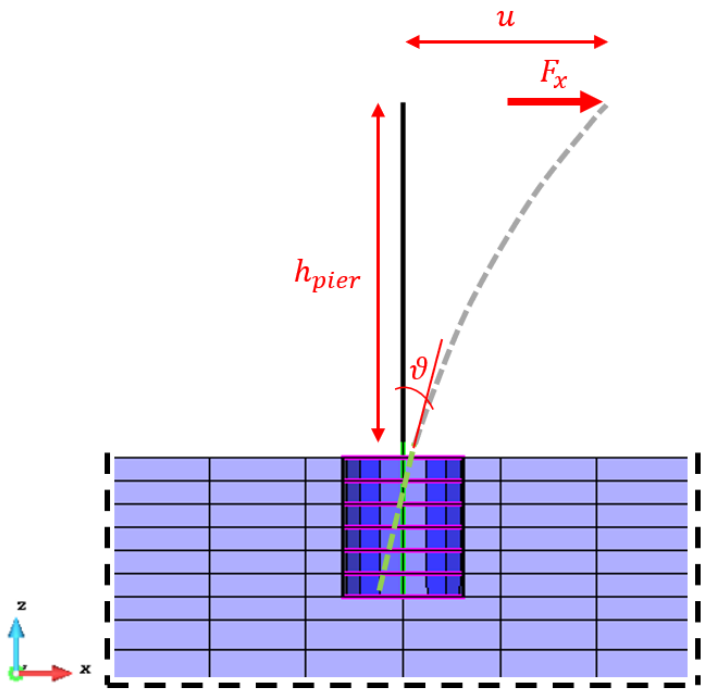

Figure 62. Pushover test using displacement control analysis

7.6.1. Influence of P-δ second order effects on the system response

Within the OpenSees framework, the consideration of P-δ effects is facilitated by assigning a P-δ Coordinate Transformation (PDeltaCrdTransf) object to the Elastic-Beam-Column-Element. Conversely, neglecting these effects is achieved by assigning a Linear Coordinate Transformation (LinearCrdTransf) object to the Elastic-Beam-Column-Element (Zhu, 2023).

For practical purposes, P-δ effects are exclusively examined and depicted solely for the NS case (*Figure 63*). In observing *Figure 63a* and *Figure 63b*, marginal changes in lateral and

rotational stiffness are evident as displacement and rotation increase. Results from the P-δ transformation display a slight reduction in lateral capacity and an increase in rotational capacity compared to those obtained from the Linear transformation. This aligns logically since the P-δ method accounts for the structure static self-weight loads in addition to M_E, whereas the Linear method only considers M_E. However, the differences between the outcomes of both transformations are negligible and due to the higher computational demand of the P-δ approach, the linear was chosen for the upcoming analysis.

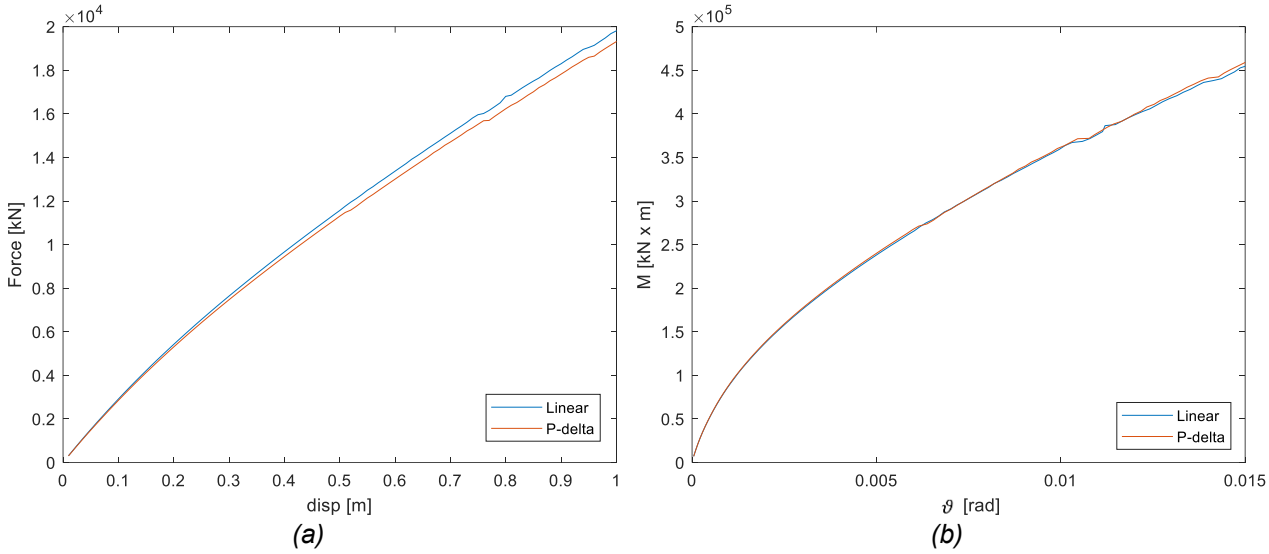

Figure 63. Comparison between Linear and P-δ coordinate transformation in the NS model; (a) F_x vs u, (b) M_E vs ϑ

7.6.2. Pier-Caisson-Soil system stiffness under scoured scenarios

Looking at evaluating the capacity of the system under the three scouring scenarios, the pushover test was carried out in the NS, GS and LS models. In the LS case, the pushover test was performed in both positive [+] and negative [-] *x-directions*, denoted as LS[+] & LS[-], respectively, to study the asymmetrical behavior of the system caused by the local scouring morphology (e.g., Ciancimino et al., 2022a). The response of the pier for each scenario is displayed in *Figure 64*. As it was expected, the horizontal and rotational stiffness of the system (*Figure 64a & Figure 64*b, respectively) are higher in the NS case, followed by LS[-], LS[+] and GS, with the GS being the most critical case.

The NS model's greater capacity compared to the GS model is attributed to the larger caisson embedment depth into the compliant soil in the NS scenario. However, the disparities between the LS[-] and LS[+] scenarios stem from the morphology of the scouring hole, because the system's lateral loading capacity is higher in the less scoured direction. This observed asymmetry in the LS case holds significance for the structure's dynamic behavior, as further elaborated in Chapter 8.

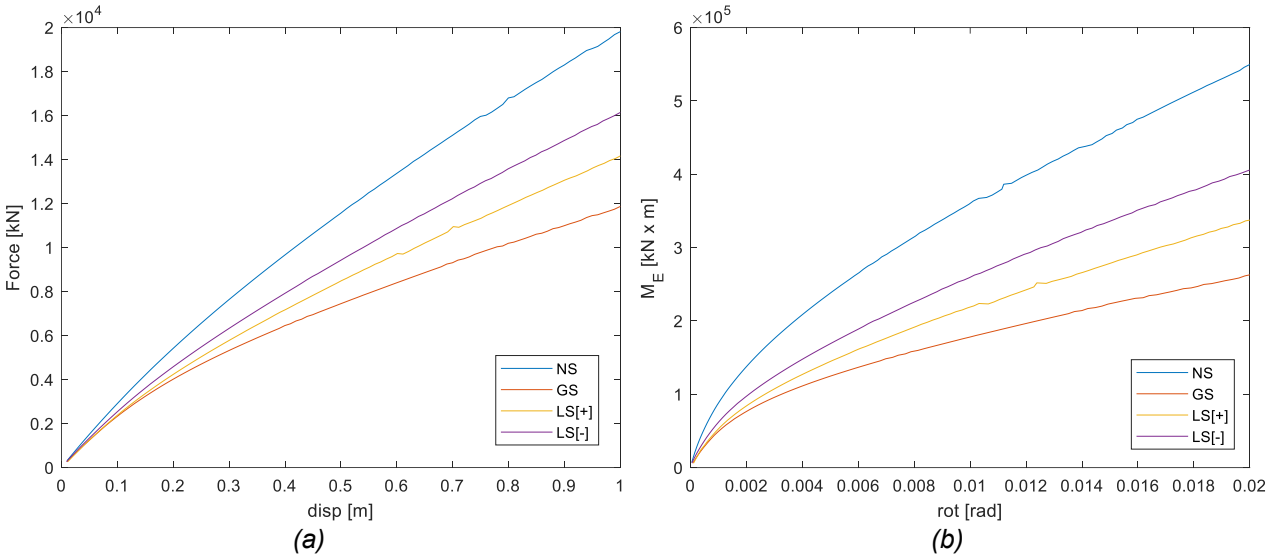

Figure 64. Results pushover test; (a) F_x vs u, (b) M_E vs ϑ

7.7. Free vibration analysis

In order to investigate pier-caisson-soil compliance in each scenario (i.e., NS, GS & LS) and to evaluate changes in the fundamental period of the system, a free vibration analysis was conducted as follows: a static force *(F_x)* was applied horizontally in the *x-direction* at the deck, as depicted in *Figure 65a*. The resulting deformation state of the system *(Figure 65b*) served as the initial conditions *(u_0)* for the subsequent transient dynamic analysis *(Figure 65c*). This process was repeated with two different values of F_x ($100\,kN$ & $1{,}000\,kN$) applied in both positive and negative *x-directions* to assess both the influence of F_x magnitude and direction in the system dynamic response, especially in the LS case. For practical purposes, only the schematic representation of the preceding pushover and subsequent free vibration test for the NS model is presented in *Figure 65*.

The dynamic response of the system is examined in terms of displacement time-history (*Figure 66*) and Fourier amplitude spectra (*Figure 67*), which are recorded at the deck. As expected, in the NS and GS models, the maximum (u_{max}) displacement at the deck increases proportionally with the magnitude of F_x. The response in both cases is symmetrical (as seen in *Figure 66a & Figure 66b,* respectively).

However, this symmetry does not hold for the LS model. As it was previously discussed in *Section 7.6.2*, in the LS scenario the response of the pier is influenced by the scour hole morphology. The asymmetry in the *x-z plane* of the scour hole renders the system more susceptible to deformation and the accumulation of displacements in the most scoured part of the foundation, that is in the *x[+]*-direction (as illustrated in figure *Figure 66c*).

When examining the Fourier Amplitude spectra (*Figure 67*), it is evident that the fundamental period of the soil-caisson-pier system undergoes changes based on the scouring conditions and the magnitude of F_x. In the NS case, the analysis reveals that the fundamental period of the caisson-pier-deck structure ($T_{0,pier} = 1.28\,s$) is shorter than the fundamental period within the

compliant soil ($T_{0,NS} = 1.37\ s$), as depicted in *Figure 67a*. Although the effect is almost negligible, this period increases slightly with the magnitude of F_x, as shown in *Figure 67b*.

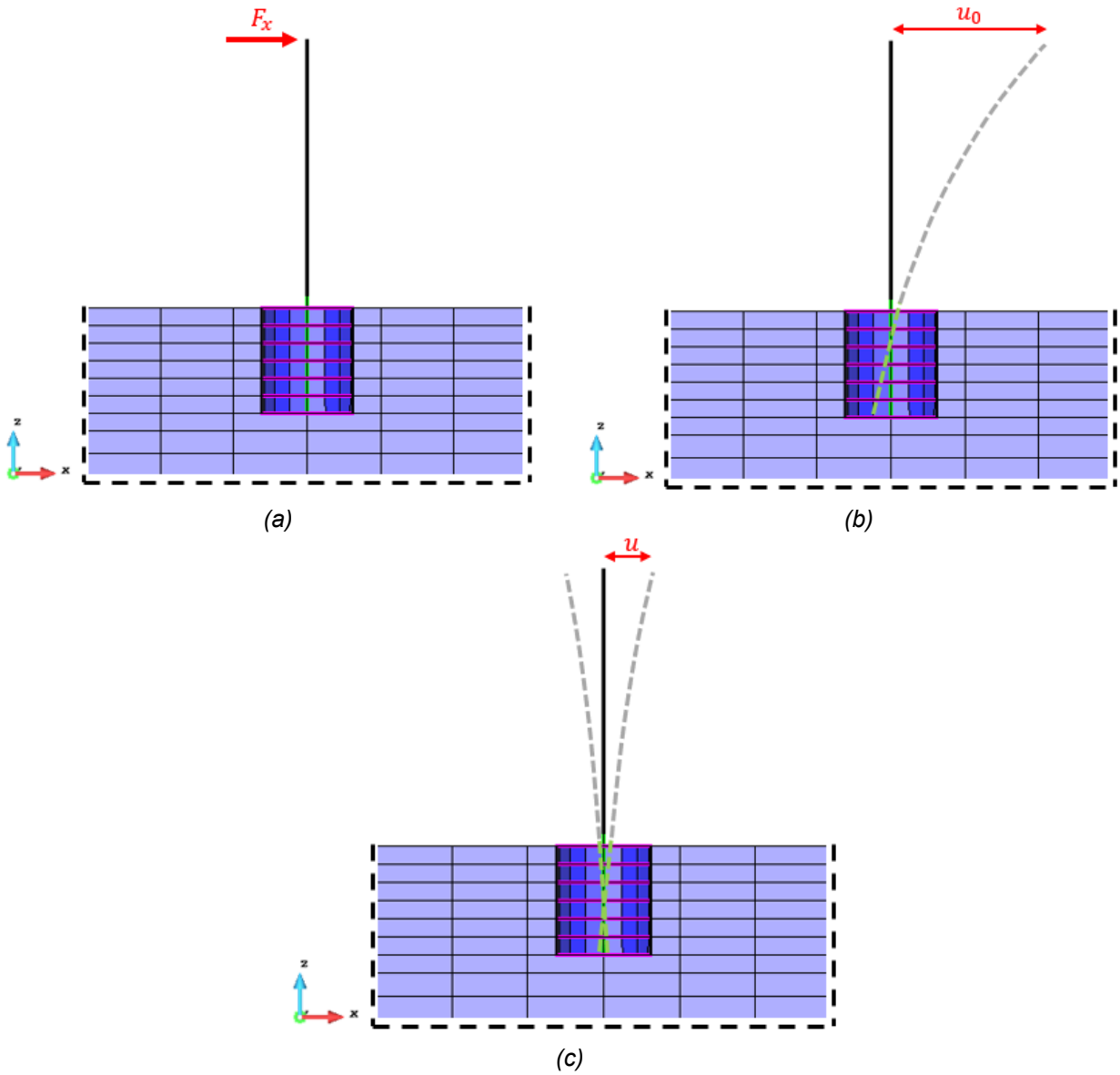

Figure 65. Pushover static force; (a) Applied initial force, (b) initial displacement, (c) system response

The increase in the fundamental period of the system ($T_{0,NS}$) compared to the structural one ($T_{0,pier}$) is attributed to soil-caisson-pier interaction, a phenomenon that has been previously documented in studies utilizing EI constitutive models for the soil (Veletsos, 1977). This effect is influenced by factors such as the slenderness ratio, relative masses, and stiffness of the structure and the soil, and it is particularly significant for stiff structures (Tsigginos et al., 2008).

Furthermore, the increase in $T_{0,NS}$ with F_x magnitude can be attributed to plastic strains and decrease in soil stiffness.

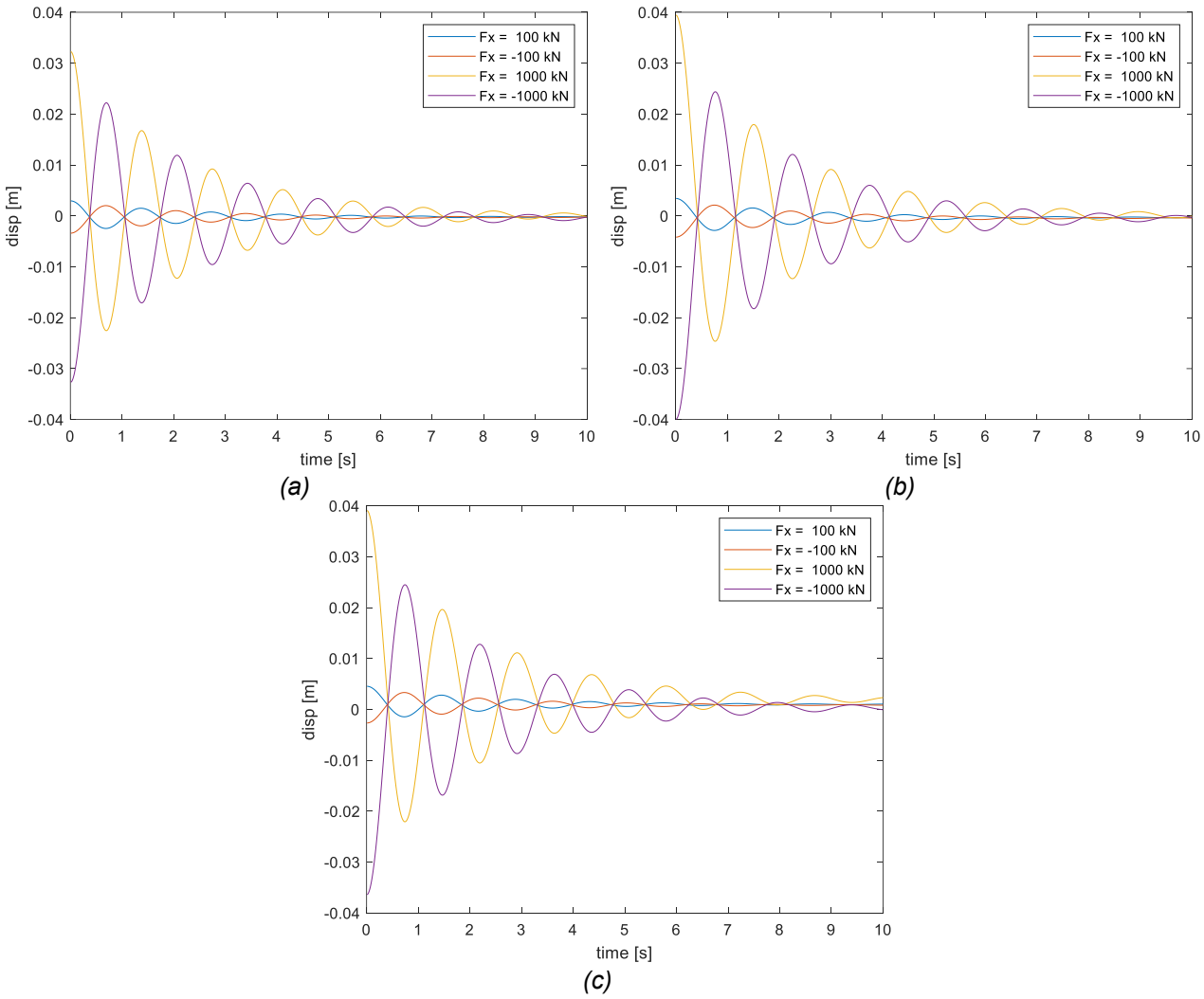

Figure 66. Free vibration after released the static force; (a) NS model; (b) GS model; (c) LS model

In the case of the GS and LS scenarios, the fundamental periods of the system, $T_{0,GS}$ and $T_{0,LS}$ respectively, are higher than $T_{0,NS}$. This increase of T_0 with the scouring depth has previously been reported in the literature, for instance, by Wang et al., (2014b). Notably, like in the NS case, $T_{0,GS}$ and $T_{0,LS}$ increase slightly with the magnitude of F_x.

While the alterations in $T_{0,NS}$, $T_{0,GS}$ & $T_{0,LS}$ appear to be minimal with the magnitude of F_x, the situation may diverge during seismic shaking. The intensity and duration of ground motion can generate notable shear strains within the soil, resulting in a more pronounced reduction in soil stiffness. Furthermore, considering the stiffness asymmetry in the LS case, and the influence of second-order effects in the structure. Consequently, the dynamic response of the structure undergoes changes during the ground motion, contingent on the on the characteristics of the latter.

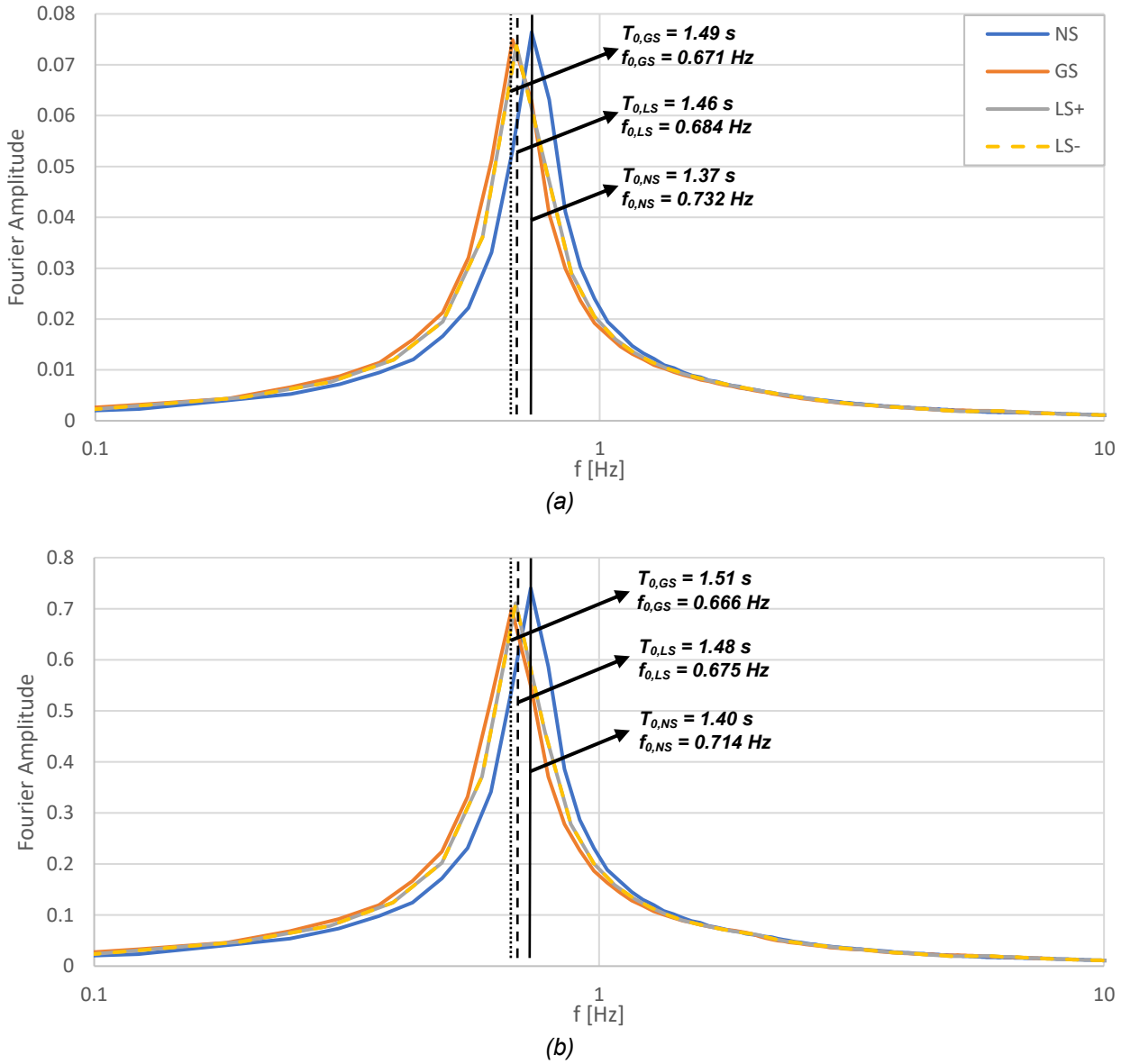

Figure 67. Fourier Amplitude for dynamic response of the system; (a) F_x = 100 kN ; (b) F_x = 1,000 kN

CHAPTER SEVEN

CHAPTER 8

SOIL-CAISSON-PIER DYNAMIC RESPONSE

Moving forward to study the effect of scouring on the seismic response of caisson foundations, the three numerical models-No Scoured (NS), General Scoured (GS) and Local Scoured (LS)-were subjected to dynamic loading using the three distinct input motions previously detailed in *Chapte*r 3. In order to capture the final deformation state and evaluate cumulative displacements, the transient analyses were extended by an additional five seconds. Furthermore, one of the input motions was magnified using a scale factor (SF) to preliminary assess the response of the structure to ground motions with increasing amplitude as well as the structural failure. The results are presented in the subsequent sections.

8.1. Dynamic response of the unscoured foundation

The response spectrum of each input motion is displayed and compared in *Figure 68* with the ground surface response spectrum (Free Field conditions), along with the spectrum obtained at the top of the caisson for the NS model. It should be observed that due to the soil-structure interaction, the caisson response spectrum, particularly at periods shorter than 1.5 s, register spectral acceleration (S_e) values lower than those of the Free Field spectrum. This discrepancy is attributed to the significantly higher density, inertia and stiffness of the foundation in comparison to the compliant soil (Tsigginos et al., 2008).

8.2. Dynamic response of the scoured foundation

For practical purposes, only a 3D snapshot of the deformed state of the system at *t=3.16 s*, which corresponds to the time step for the maximum deck displacement recorded using *Cosenza* input motion, is illustrated in *Figure 69*. To enhance visibility, displacements into the system have been magnified by a factor of *100.* It is apparent in this image that in the GS case (*Figure 69b*), the presence of the caisson affects a larger portion of the soil volume compared to the NS (*Figure 69a*) and LS (*Figure 69c*) cases.

To analyze the ultimate deformed state of the structure, corresponding to the conclusion of the seismic shaking, an additional five seconds were added to the transient dynamic analysis. This extension accommodated the free vibration response of the structure, ensuring that the final equilibrium state is achieved. The deformed state of the system using the same input motion and scaling factor is illustrated in *Figure 70*.

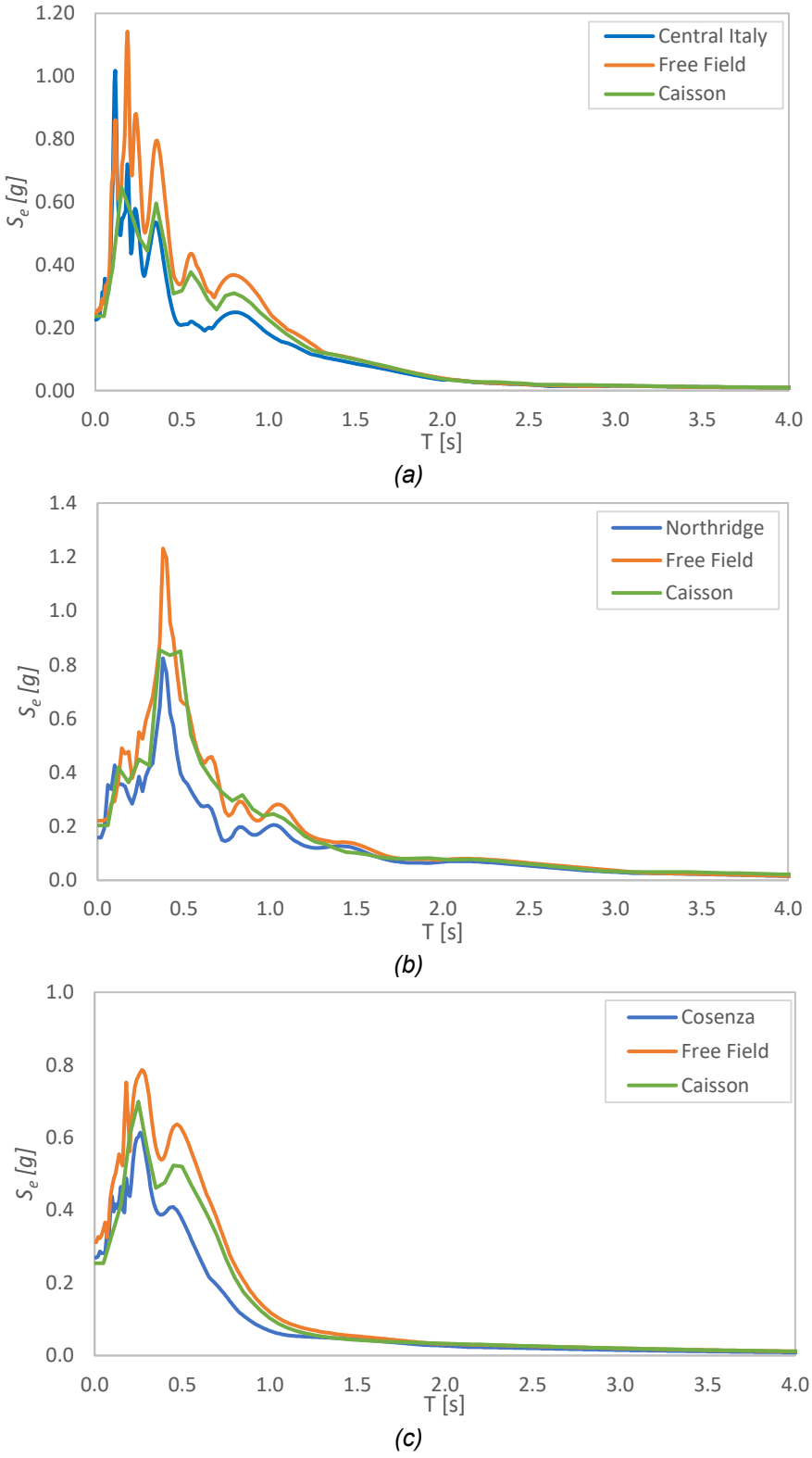

Figure 68. Response spectrums from Input motion, Free Field & Caisson; (a) Central Italy; (b) Northridge; (c) Cosenza

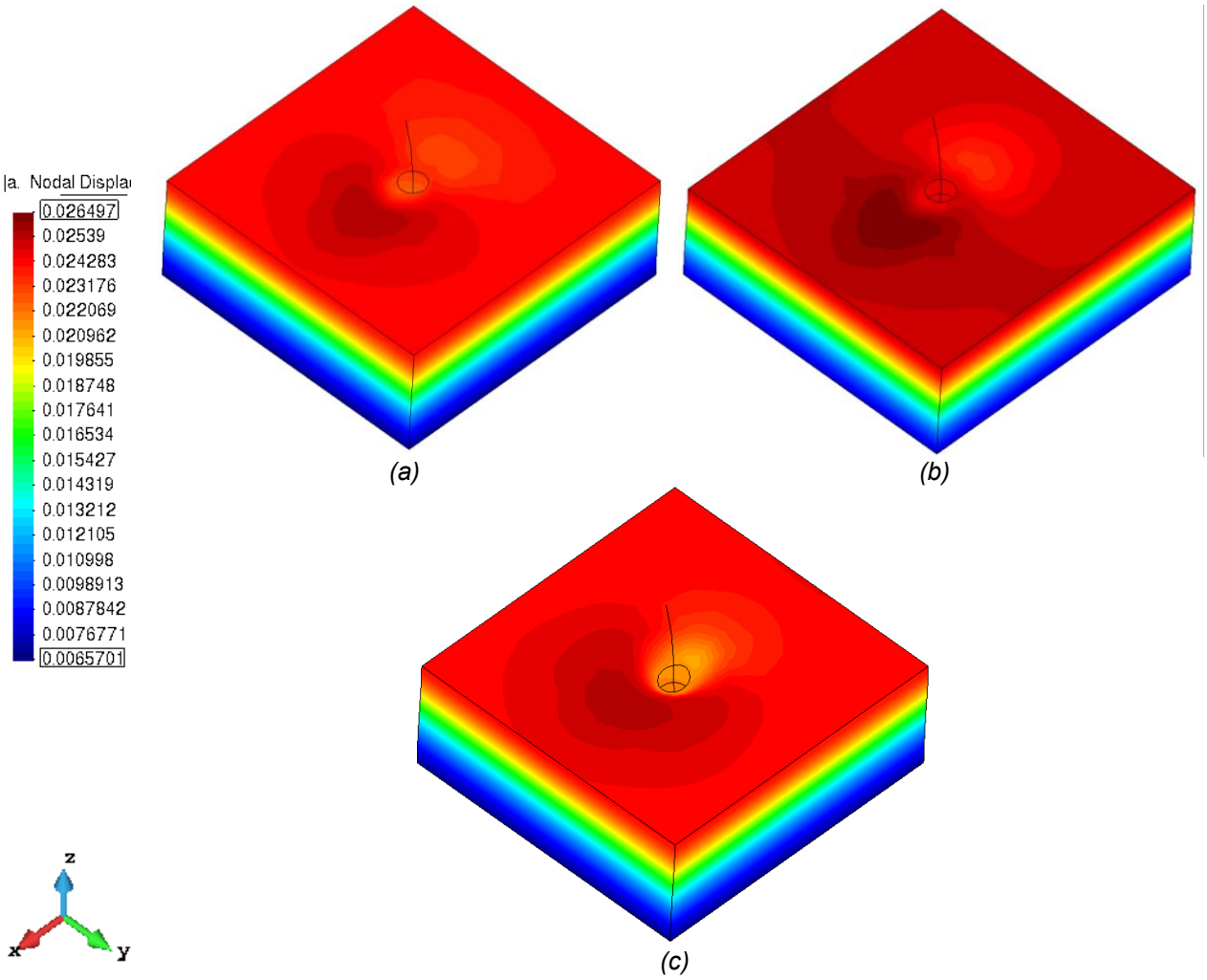

Figure 69. 3D view of Soil-Caisson-Pier system displacements at t=3.16 s [scaled x100] using Cosenza input motion; (a) NS model; (b) GS model; (c) LS model

Furthermore, to delve into the asymmetrical response within the LS scenario (discussed in earlier sections 7.6.2 and 7.7), the input motion direction was altered. This adjustment allowed the exploration of the LS[+] case response along with its counterparts, LS[-], which illustrate the dynamic response with the input motion direction switched.

The response spectra at the caisson and at the deck for each case (i.e., NS, GS & LS) derived from each input motion (i.e., Central Italy, Northridge & Cosenza) are presented in *Figure 71.* Upon closer examination of these results, it becomes evident that, for periods shorter than 0.7 s, general scouring induces higher S_e values at the caisson. However, for longer periods, the impact of general scouring on the response spectrum does not substantially differ from that of the NS and LS cases. Notably, there are no significant differences observed between the NS and LS cases in terms of the response spectrum at the caisson.

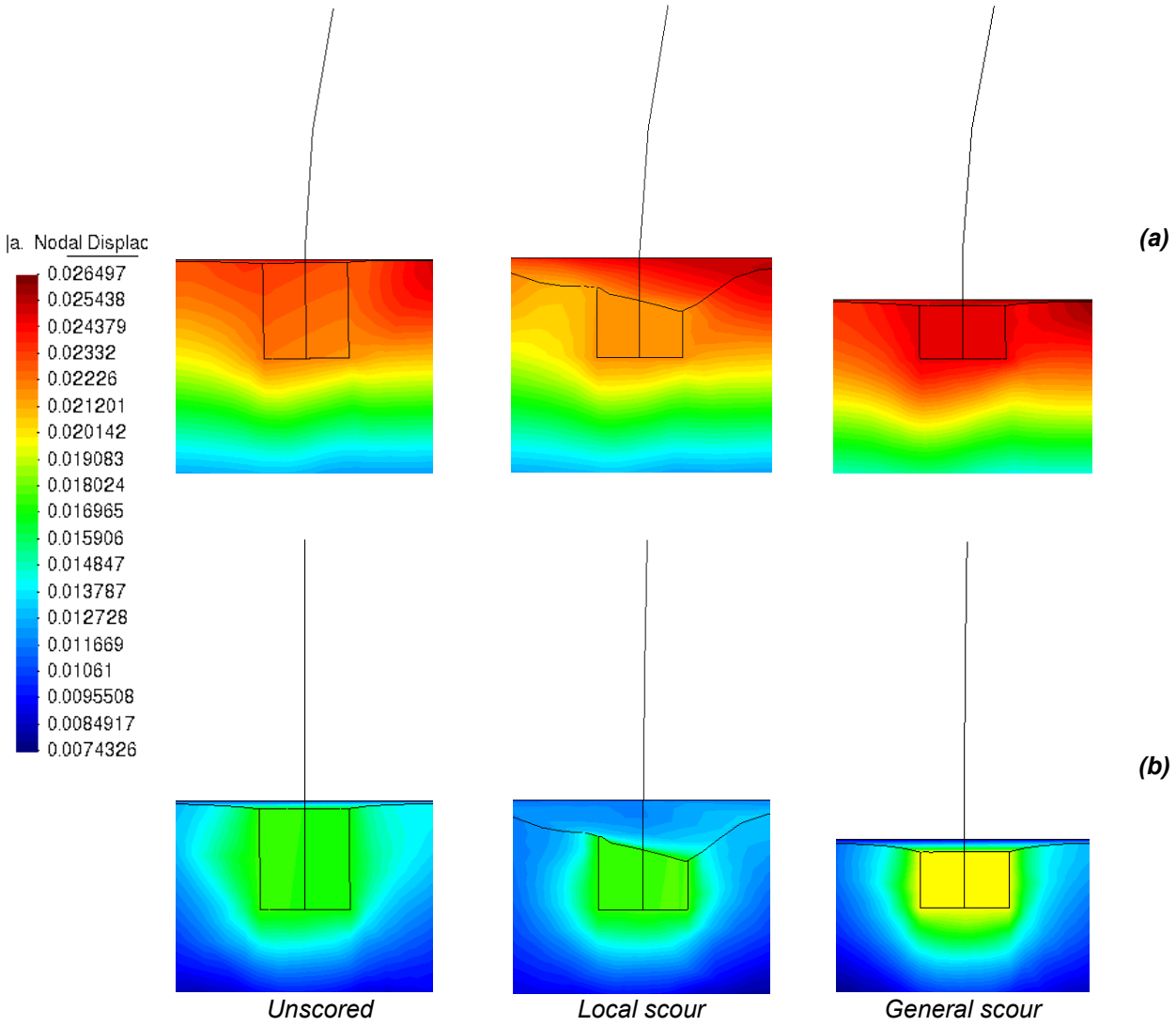

Figure 70. Cross section view of Soil-Caisson-Pier system for NS model, GS model & LS model [scaled x100] using Cosenza input motion; (a) max displacements (t = 3.16 s) ; (b) residual displacements (t = 27.96 s)

A different observation emerges when examining the response spectrum at the deck, particularly within the period range of 0.7 and 1.8 s, a range that encompasses the fundamental period of the system (*Figure 67*). During this interval, S_e is notably higher in the NS case, followed by the LS and finally, the GS case. This reduction in S_e within this period range suggests a higher dissipation of energy by the soil compared to the NS case, with the LS case lying in between. Research by Klinga & Alipour, (2015) & Wang et al., (2014b) has elucidated this phenomenon, indicating that scouring might induce an isolation effect, leading to a diminished transmission of seismic forces to the structure. This effect arises due to nonlinear soil–foundation–structure interaction (SFSI), wherein the compliant soil's inelastic response curtails the inertial forces impacting the superstructure but results in unwanted settlements (Anastasopoulos et al., 2012; Zafeirakos & Gerolymos, 2014).

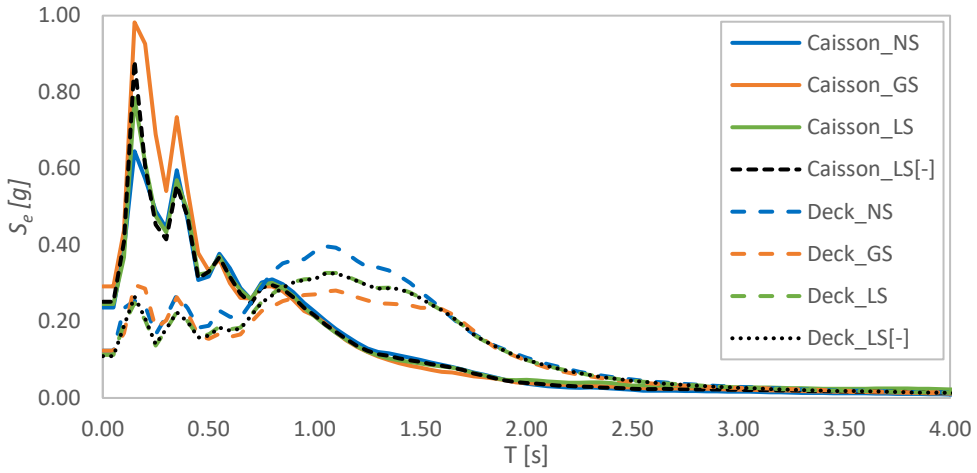

(a)

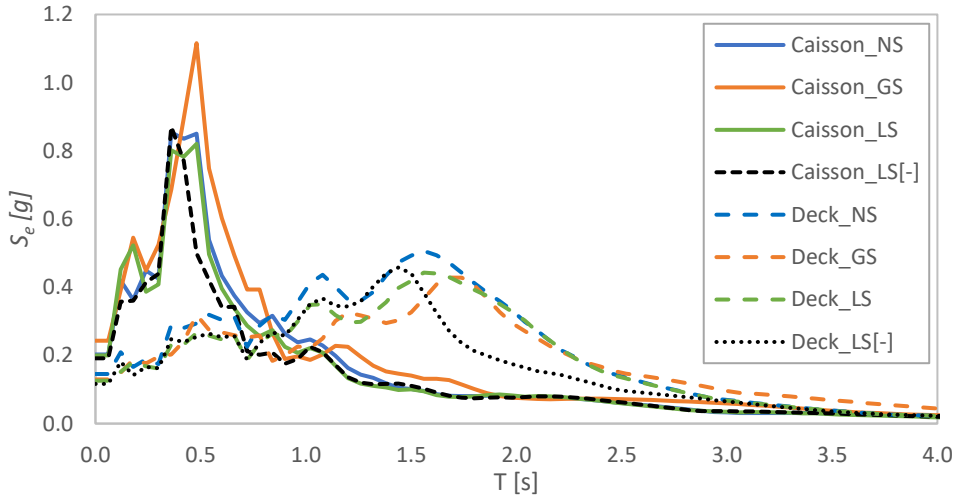

(b)

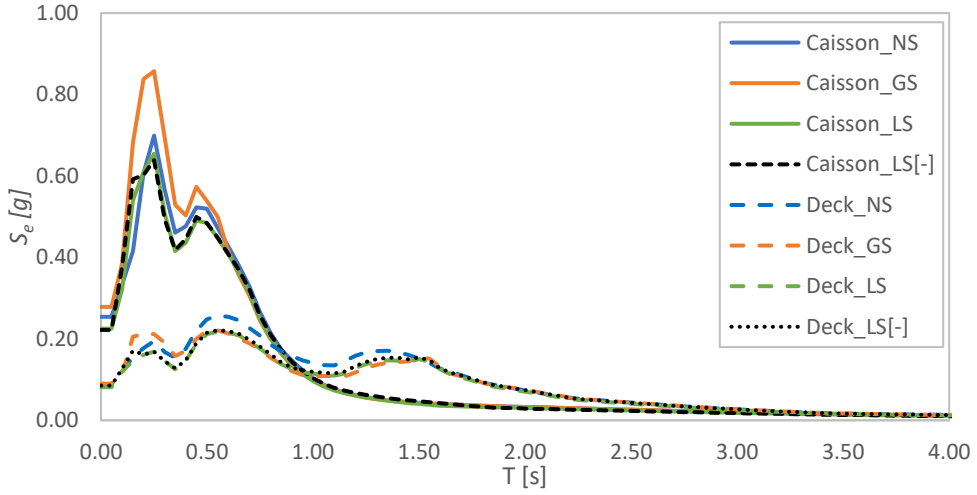

(c)

Figure 71. Response spectrums at the top caisson and deck for each model with the respective a_{max} at the deck; (a) Central Italy; (b) Northridge; (c) Cosenza

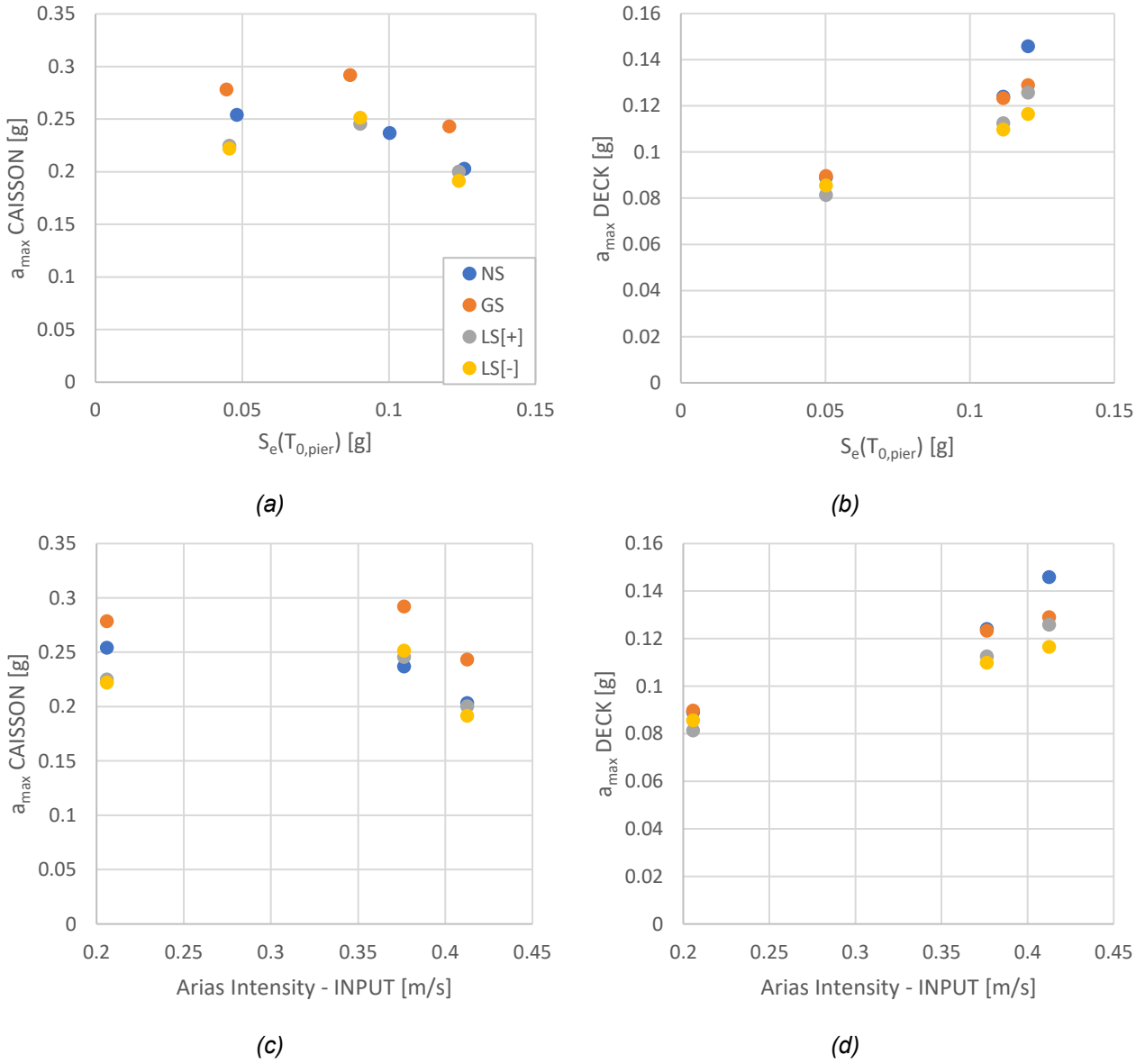

Figure 72. a_{max} at the caisson and at the deck vs $S_e(T_{0,pier})$ and arias intensity (AI); (a) a_{max} Caisson vs $S_e(T_{0,pier})$; (b) a_{max} Deck vs $S_e(T_{0,pier})$; (c) a_{max} Caisson vs AI Input; (d) a_{max} Deck vs AI Input

When examining the response spectrum of LS[+] and LS[-] (*Figure 71*) at the caisson, there are minimal differences, except for a slight variation at shorter periods (less than 0.7 s). However, notable distinctions emerge when analyzing the response at the deck. This can be observed contrasting *Figure 71a & Figure 71c* (Central Italy and Cosenza, respectively) where both LS response match perfectly, and *Figure 71b (Northridge*) where a significant discrepancy becomes evident upon closer examination.

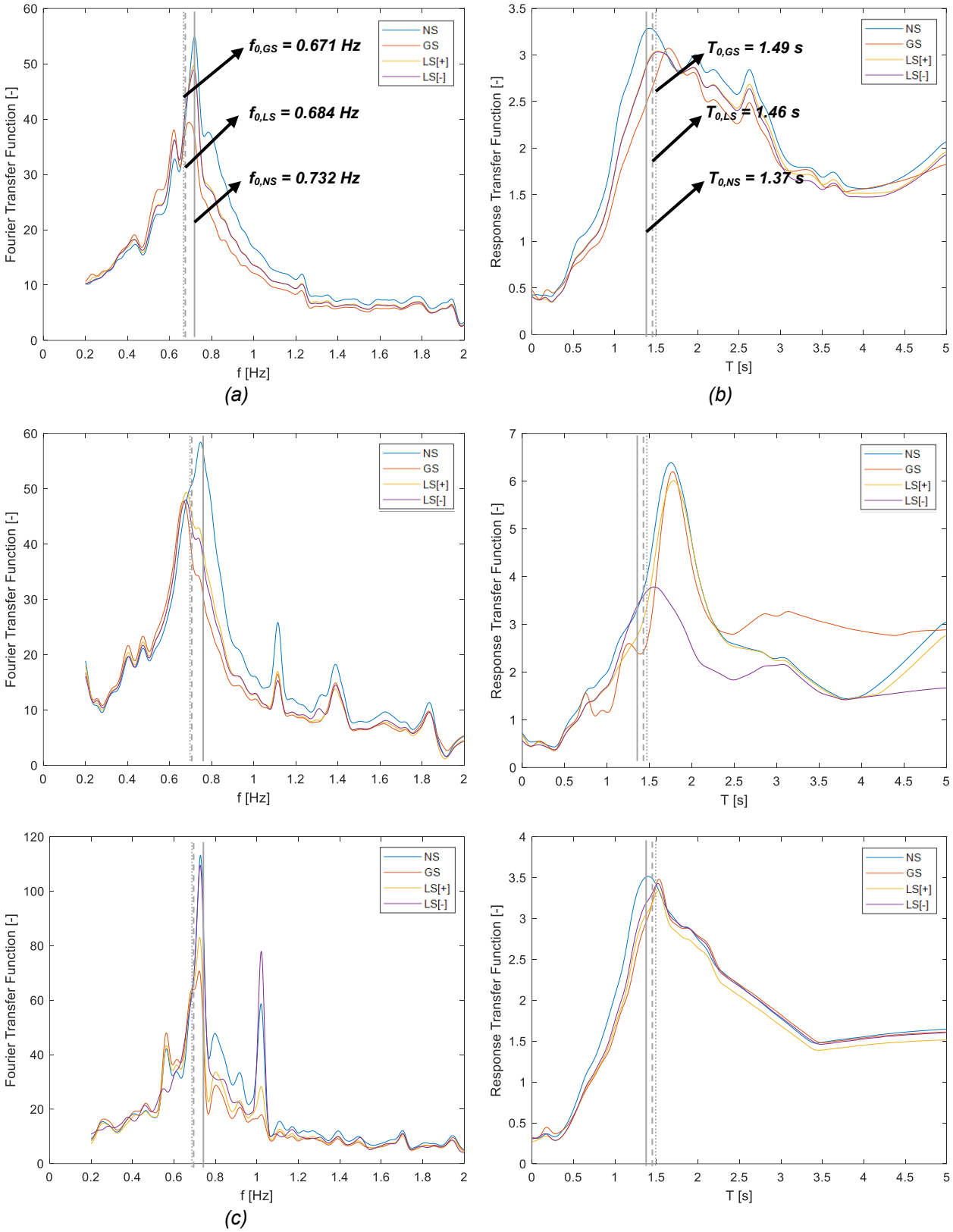

Figure 73. Fourier Amplitude Function; (a) Central Italy; (b) Northridge; (c) Cosenza

Additionally, a_{max} at both the caisson and the deck is graphically compared with the input spectral acceleration at the fundamental period of the pier, $S_e(T_{0,pier})$, in *Figure 72a & Figure 72b,* and input Arias intensity (AI) in *Figure 72c & Figure 72d,* respectively. The response a_{max} at the deck shows a notable increase with increasing $S_e(T_{0,pier})$ (*Figure 72b*) and AI (*Figure 72d*). Nevertheless, a_{max} at the deck is lower for both GS and LS cases compared with NS case. This aligns with the scouring seismic isolation effect discussed above.

The Fourier Transfer Function and Response Transfer Function at the deck is displayed in *Figure 73*. The Fourier Transfer Function denotes the ratio between the deck and input Fourier amplitude spectra, and the Response Transfer Function denotes the ratio between the deck and input response spectra.

Upon examining the Fourier Transfer Functions for each scenario and input motion employed, these reveal substantial amplifications at frequencies slight lower than the fundamental ones computed during the free vibration tests (i.e., $f_{0,NS}$, $f_{0,GS}$ & $f_{0,LS}$) (*Section 7.7*). Generally, amplification is more prominent in the NS case and comparatively smaller in the GS case. In the LS scenarios, the amplification fluctuates, sometimes LS[+] larger and other times smaller than LS[-], depending on the specific input motion utilized.

The above aligns with what is observed when looking at Response Transfer Functions. Notably, the maximum amplification for each scouring scenario occurs at periods larger than $T_{0,NS}$, $T_{0,GS}$ & $T_{0,LS}$, especially noticeable when utilizing the Northridge input motion (*Figure 73b*), which possesses the highest AI (*Table 3*). This suggests a direct correlation to the increase in the fundamental period of the system, attributed to the presence of plastic strains within the compliant soil during the shaking, which consequently reduce the stiffness of the soil-caisson-pier system and hence increases the fundamental period.

The caisson rotation time-histories are presented *in Figure 74* and the deck displacements time history in *Figure 75*, for each input motion and scour scenario. Observing the caisson rotation during the shaking (*Figure 74)*, it becomes evident that the magnitude of the rotation, particularly during the most intense part of the shaking, is greater in the GS compared to the NS case. However, a distinct trend emerges when the LS[+] & LS[-] cases are analyzed, this tend to rotate towards the most scoured direction. In contrast, the system in the NS and GS cases follows a similar rotation path but with varying amplitudes, generally higher in the GS case.

The above-mentioned pattern is similarly observed in the deck displacements (*Figure 75*). But unlike the caisson rotations, the deck displacements are generally higher in the NS case at the first seconds of the motion, and lower at the last seconds of the motion, an effect explained by the cumulative strains.

It is important to highlight that the discrepancy between caisson rotation amplitude and deck displacement amplitude can be an effect of how the pier responds to the input motion at the caisson in each scouring scenario because the fundamental period of the system is different in each scenario. Therefore, a different trend can be found with a pier with a different fundamental period (e.g., Gaudio & Rampello, 2021).

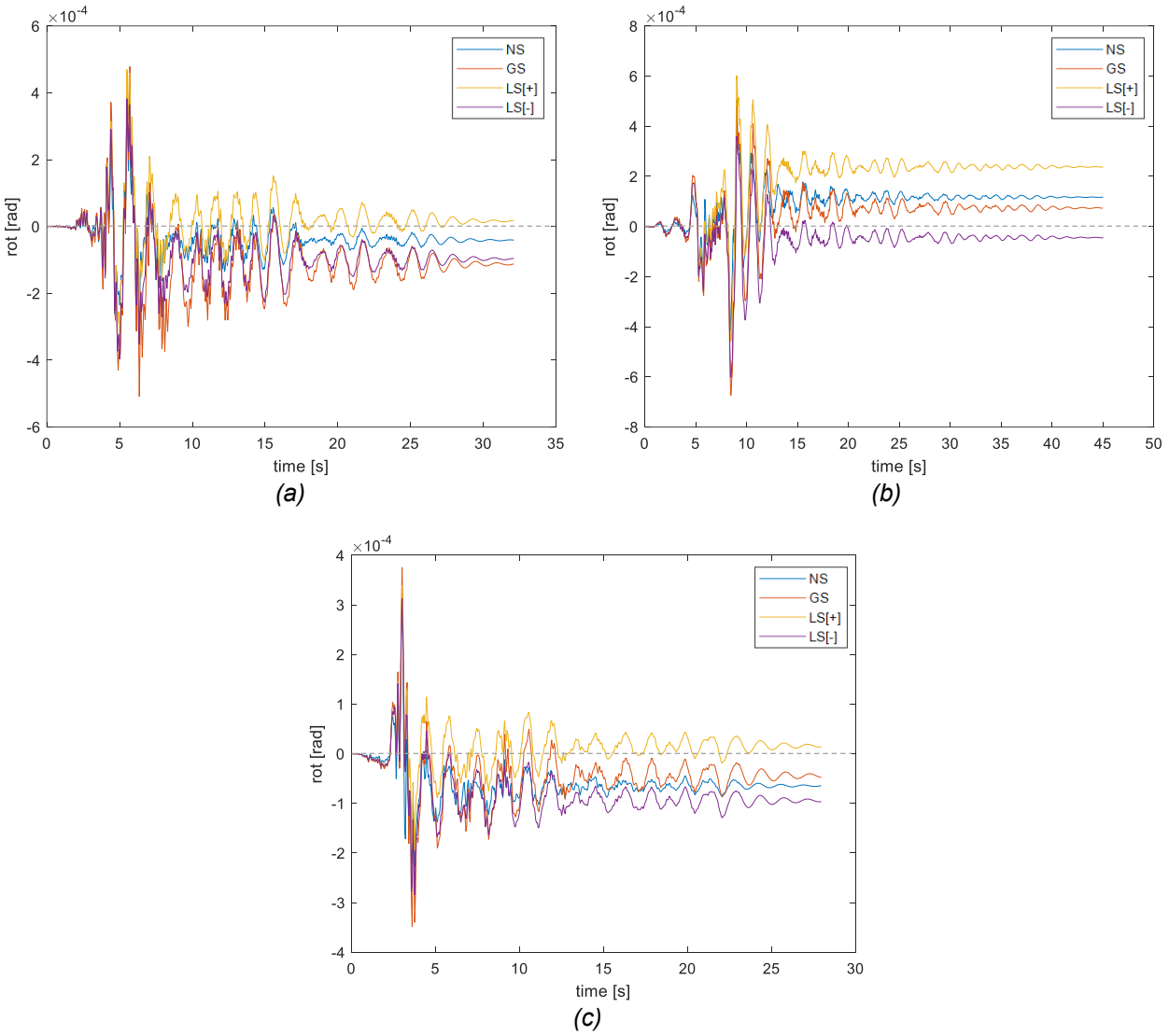

Figure 74. Caisson rotation time-history (a) Central Italy; (b) Northridge; (c) Cosenza

The pattern observed in the LS case is a consequence of the system's asymmetrical stiffness which is linked back to the morphology of the scour hole. Consequently, the absolute values of caisson rotation and deck displacements appear lower or higher depending whether LS[+] or LS[-] case is considered. This trend is further confirmed when analyzing both the residual caisson rotation and residual deck displacements. This means that in LS[+] and LS[-] cases the maximum and residual rotation and displacements at the deck are influenced by the direction of input a_{max}. In other words, whether the a_{max} direction is towards or against the direction where the scour depth is largest.

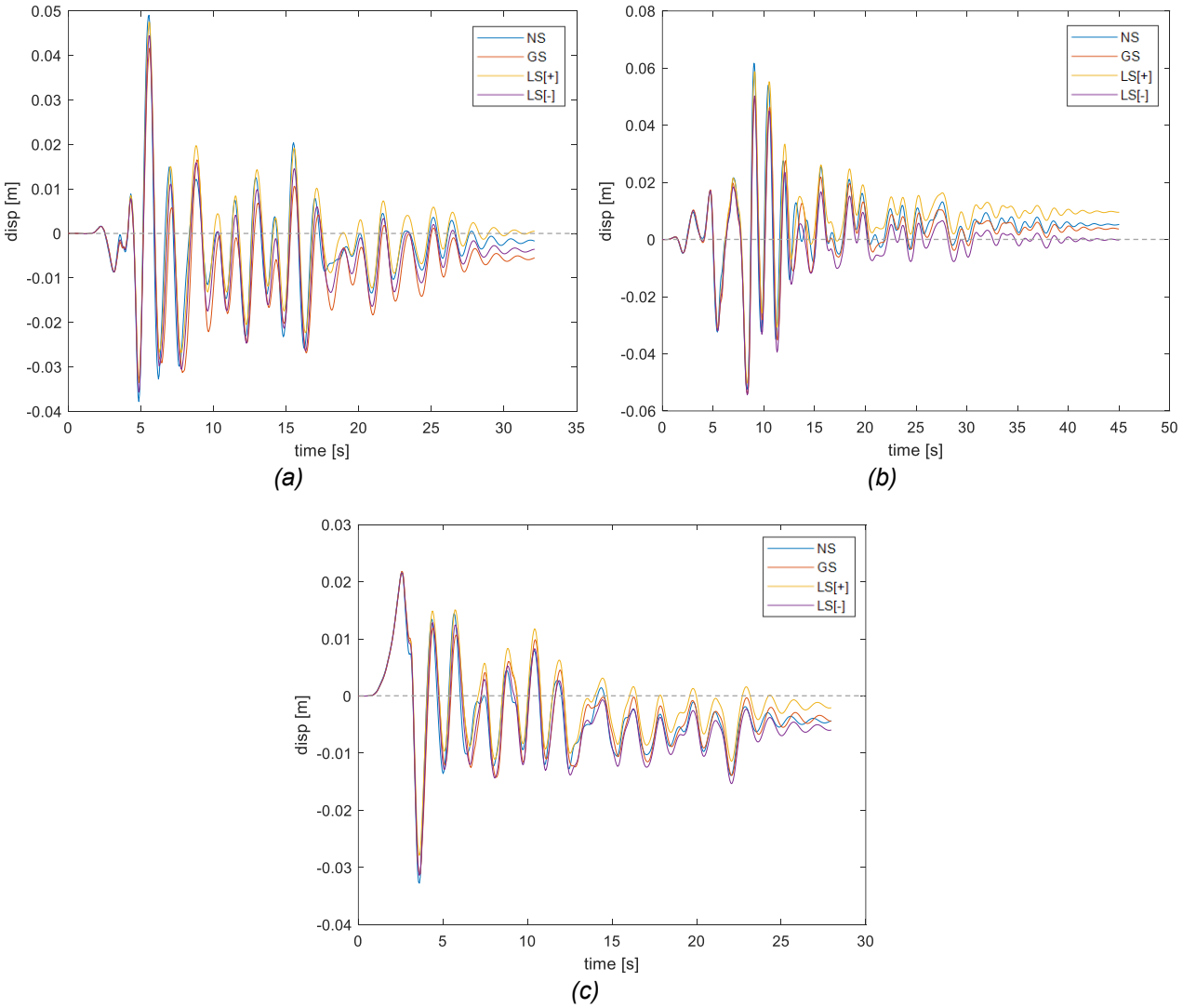

Figure 75. Deck horizontal displacement time-history; (a) Central Italy; (b) Northridge; (c) Cosenza

This finding is further substantiated when examining the residual shear strains within the compliant soil (*Figure 76, Figure 77 & Figure 78*), revealing higher residual shear strains in both scoured scenarios (GS and LS) compared to the NS scenario. However, a detailed analysis of the LS[+] and LS[-] cases highlights a clear asymmetric trend in the accumulation of shear strain. This asymmetry dictates that the LS scenario can accumulate varying degrees of shear strains, depending on the input motion characteristics and scour morphology, presenting a notable variability in its response.

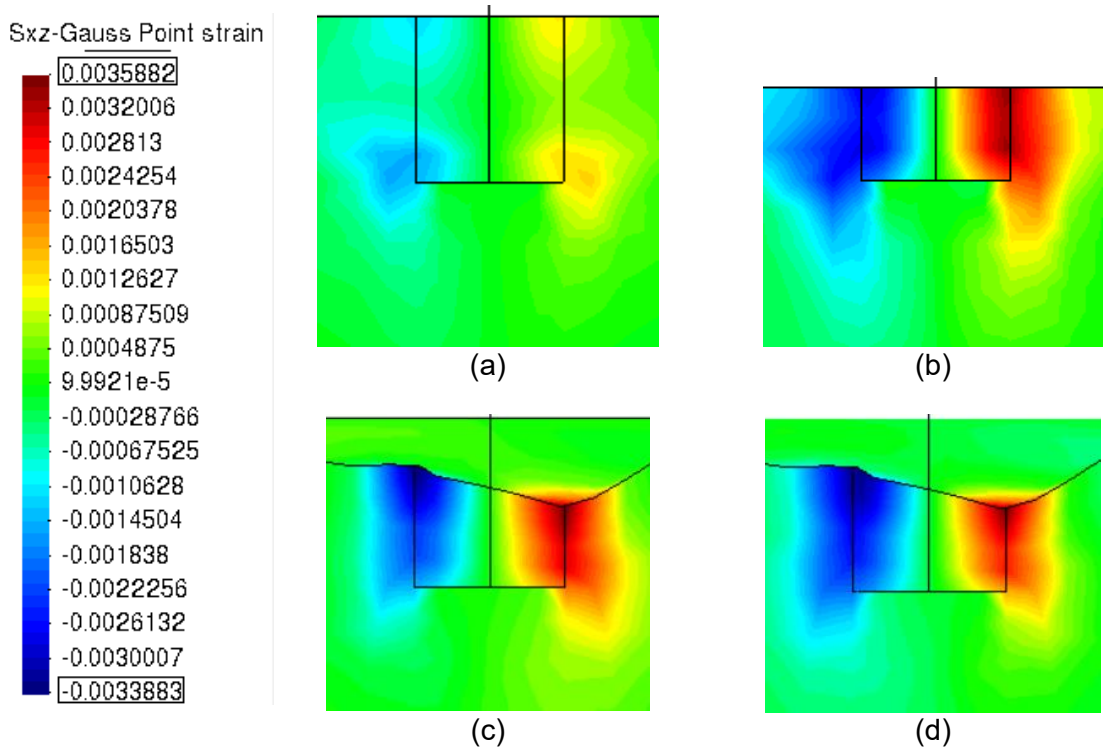

Figure 76. Residual strains - Central Italy; (a) NS, (b) GS, (c) LS[+], (d) LS[-]

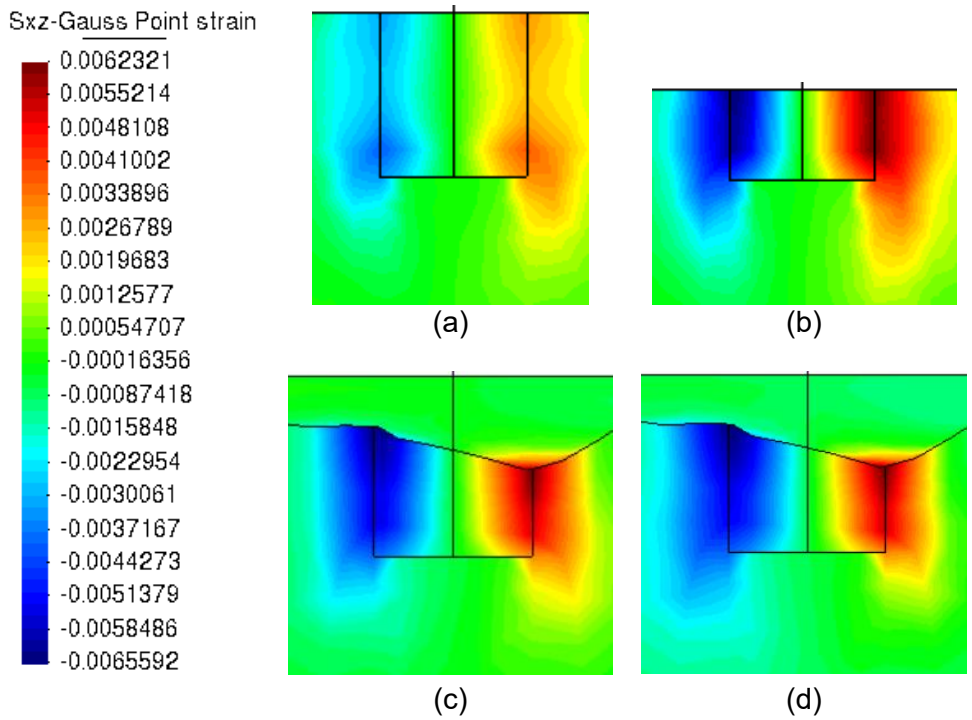

Figure 77. Residual strains - Northridge; (a) NS, (b) GS, (c) LS[+], (d) LS[-]

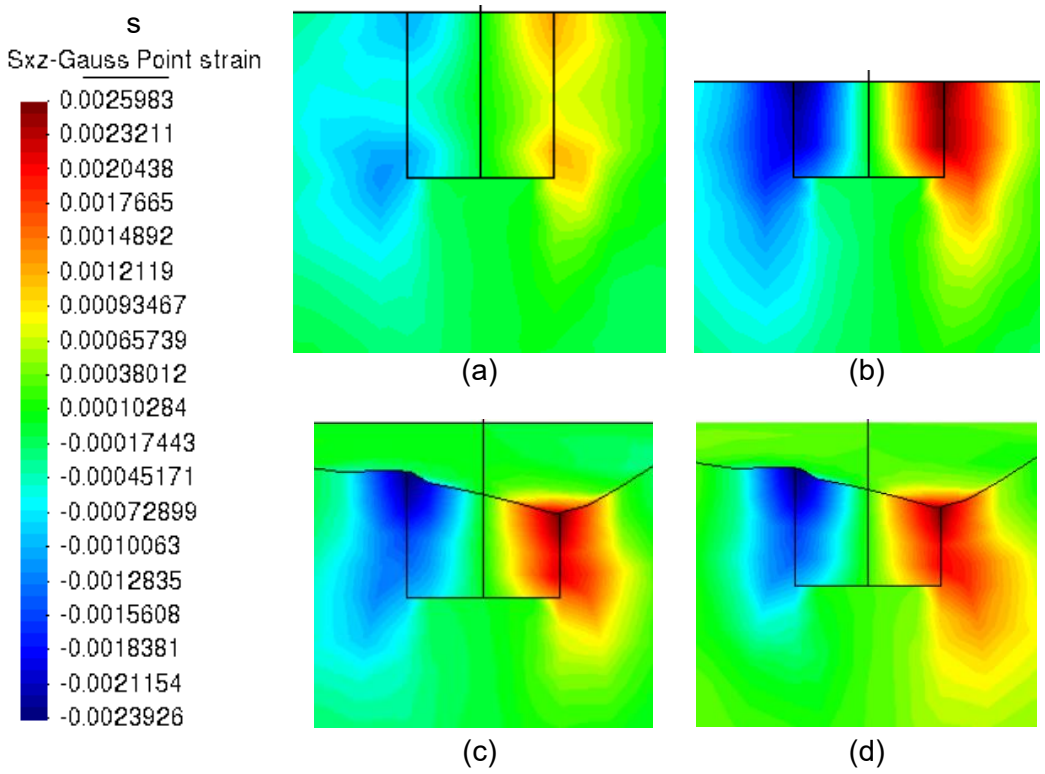

Figure 78. Residual strains - Cosenza; (a) NS, (b) GS, (c) LS[+], (d) LS[-]

Looking at the deck vertical displacement time history (*Figure 79*) (i.e., settlements during the shaking), these are always higher in the scoured cases (i.e., GS & LS) compared with the NS case. Nevertheless, the detrimental effect of scouring in the settlement accumulation is much larger in the GS case. The differences in terms of settlements between the NS and LS cases are practicably negligible. Ciancimino et al. (2022a) found something similar, they concluded that the detrimental effect of general scouring in the bearing capacity of a caisson foundation is higher compared with local scouring. Indeed, the effect of the latter was almost negligible in the bearing capacity but considerable in the sides' resistance mechanisms.

The detrimental effect of general scouring in the bearing capacity is explained by the lower overburden pressure present in the soil by the side of the caisson in the GS case (*Figure 60*) with respect to the NS (*Figure 59*) and LS (*Figure 61)* cases. According to the bearing capacity for embedded foundations and the logarithmic failure surface formulated by Terzaghi, a reduction in the overburden pressure reduces the soil bearing capacity.

Furthermore, upon reviewing the accumulated shear strain at the conclusion of the shaking (*Figure 76, Figure 77 & Figure 78*), it is evident that the accumulated shear strain in the GS case exhibits notably higher accumulated shear strain in contrast to the NS and LS cases. This heightened accumulated displacement, alongside the related reduction in soil stiffness, accounts for the increased settlement observed in the GS case.

However, the settlement during dynamic seismic loading is primarily a consequence of soil densification due to shaking. This can be observed in the first five seconds of the settlement

time history, where no difference between no scoured foundation (NS case) and scoured foundation (GS and LS cases) can be noticed. The above reveals the interplay effect of scouring conditions and shaking-induced soil densification in foundation settlement dynamics.

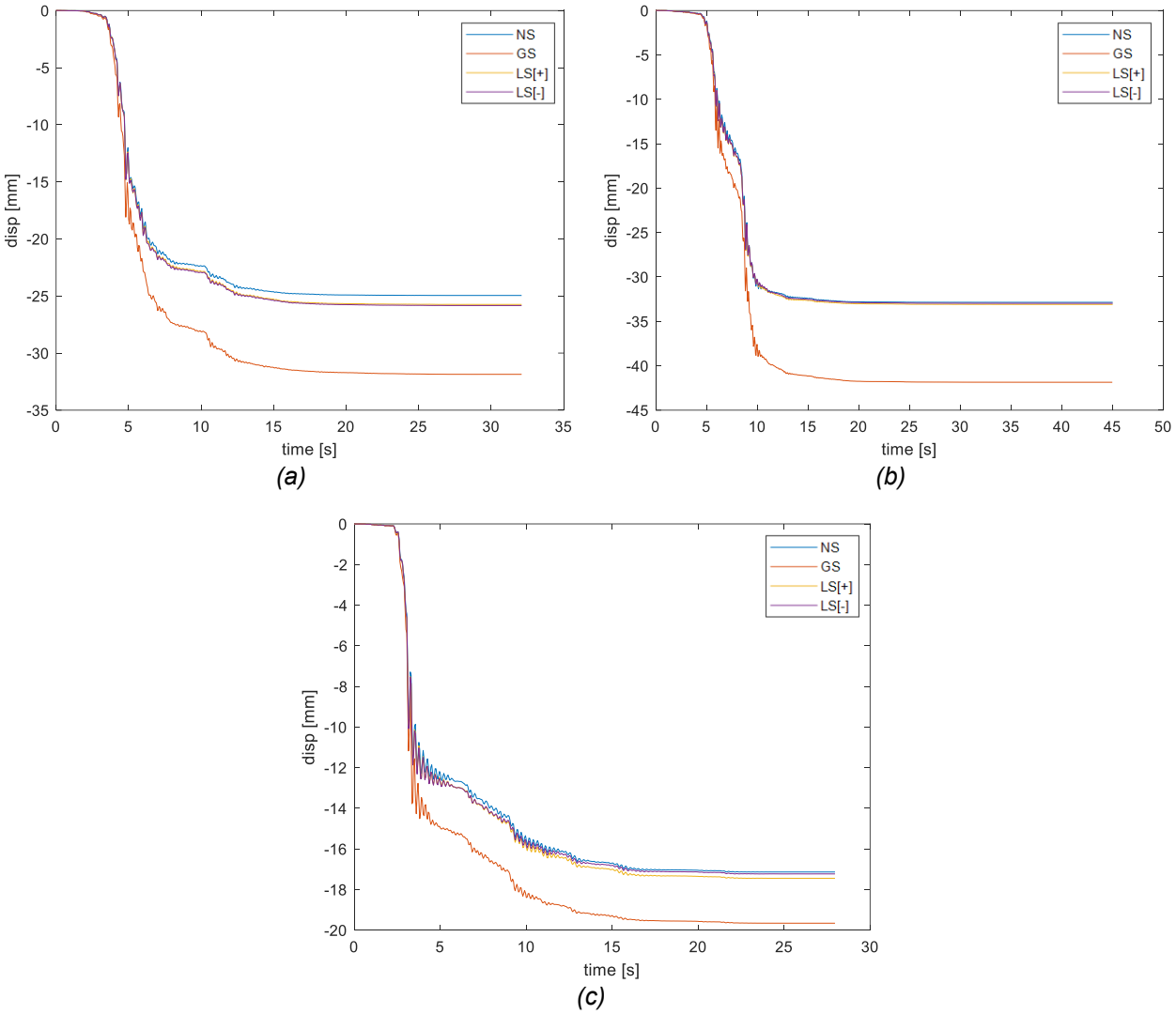

Figure 79. Deck vertical displacement time-history; (a) Central Italy; (b) Northridge; (c) Cosenza

8.3. Response to strong ground motion

Aiming at examining the response of the system to strong ground motion, the Northridge input motion was chosen as a reference and magnified to increase its intensity according to a linear scaling factor (SF) applied to the acceleration time history. The SF used were *x2.0, x4.0 & x6.0*.

Examining the caisson rotation (*Figure 80*) and deck horizontal displacement (*Figure 81*) time histories for each of the scaling factors used, it can be noticed, that the same behavior

described in the previous section is still present. However, the amplitudes of the residual values of rotation and displacement are higher.

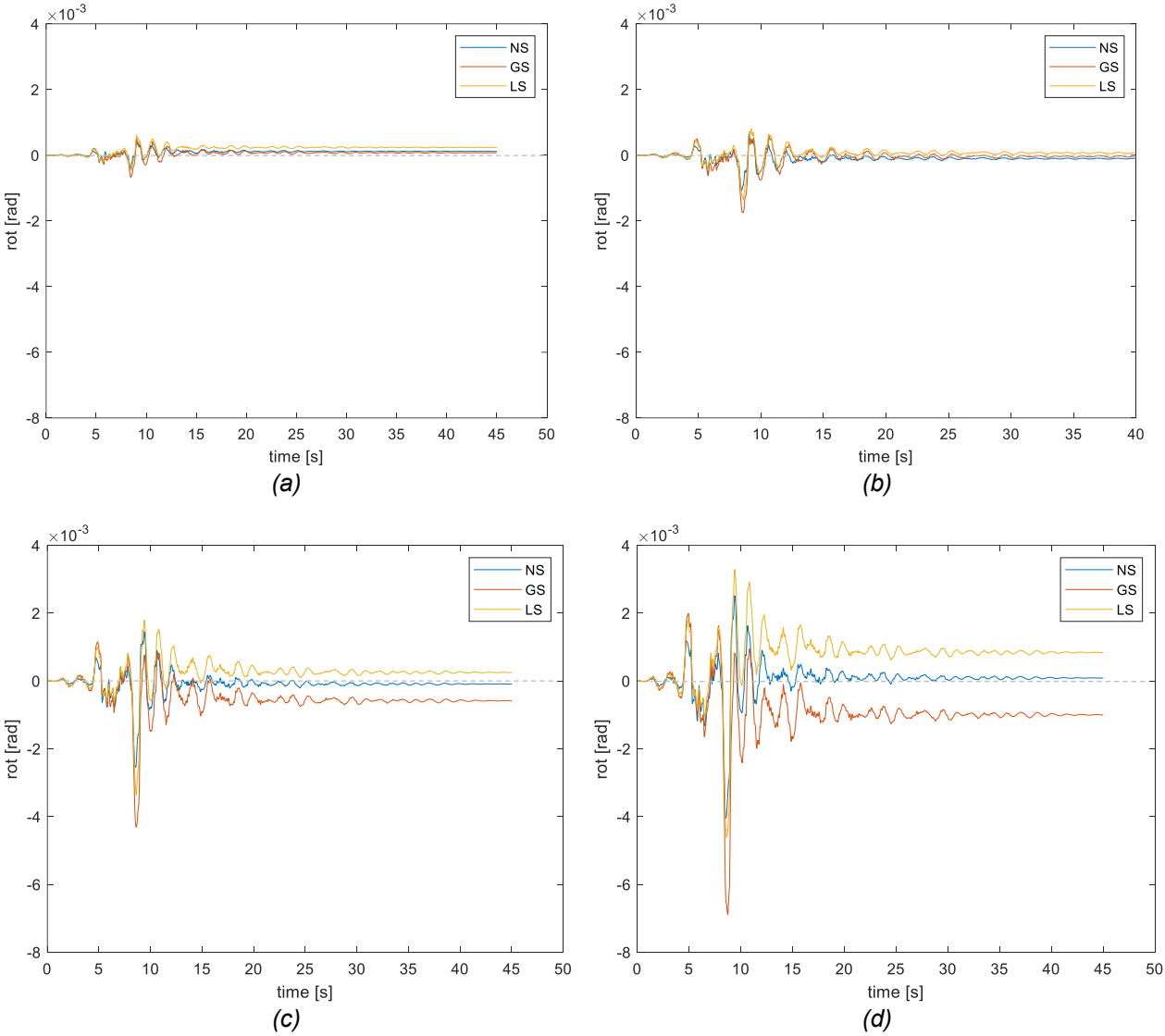

Figure 80. Caisson rotation [rad] time-history for magnified Northridge input motion; (a) SF = 1.0; (b) SF = 2.0; (c) SF = 4.0; (d) SF = 6.0

Looking at a_{max} at the deck vs magnified Northridge $S_e(T_{0,pier})$, it is evident that a_{max} at the deck increases with $S_e(T_{0,pier})$ for all cases (*Figure 82*). Nevertheless, the NS case shows a linear trend between a_{max} and $S_e(T_{0,pier})$, but a different trend is present in the GS and LS case, where the increasing effect of $S_e(T_{0,pier})$ in a_{max} decreases for higher values of $S_e(T_{0,pier})$. This observation suggests a strengthening of the isolation effect attributed to scouring and soil non-linearity as a_{max} increases.

The strengthening of the isolation effect can be detailed better by examining the response spectra, computed at the deck, for each scoured scenario and SF employed *(Figure 83*). This effect, as discussed in the previous section, remain stronger for the GS scenario.

However, these findings are preliminary as they only involve a single input motion magnified with various scale factors (SF), neglecting the influence of the input motion's frequency content.

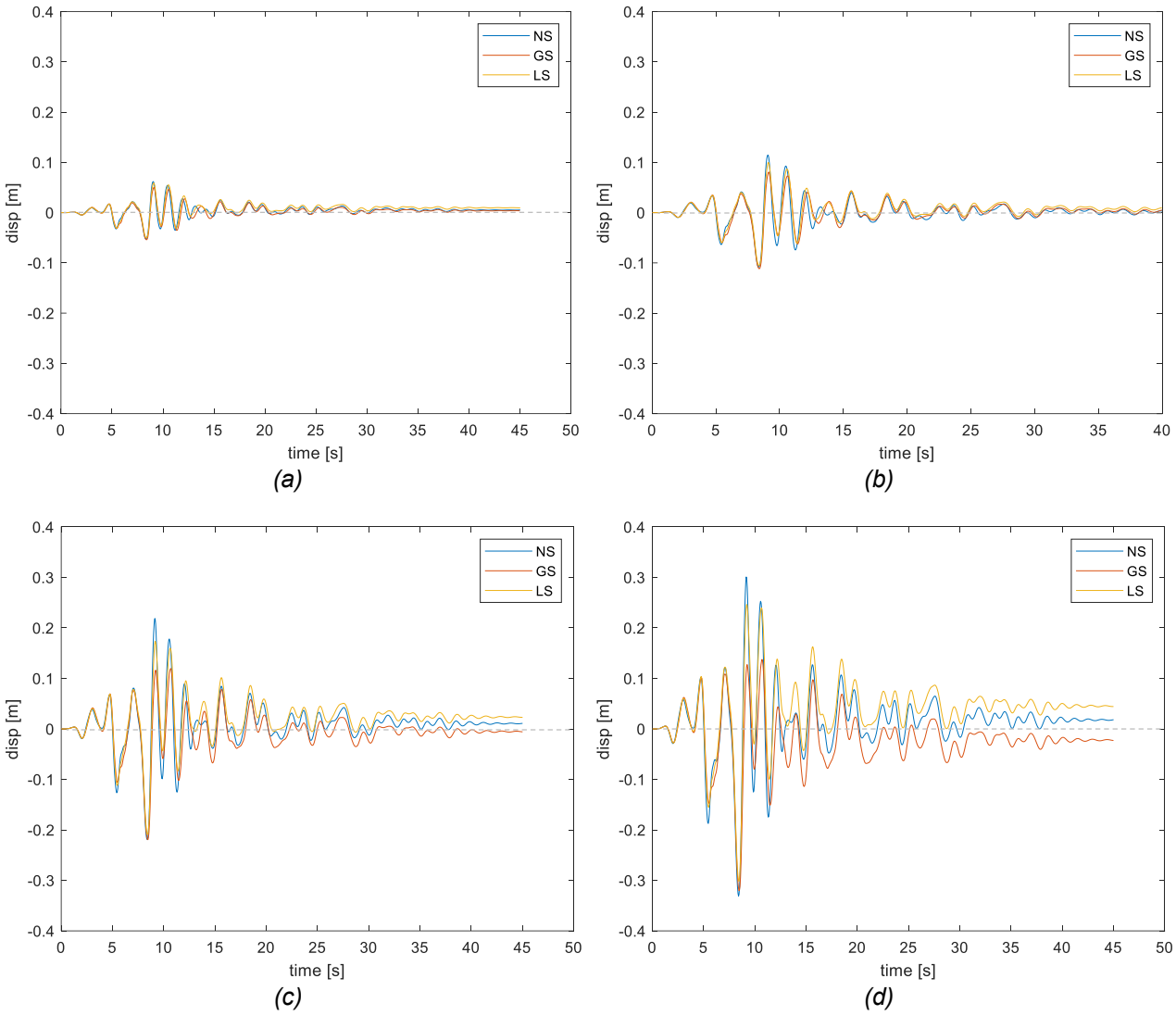

Figure 81. Deck horizontal displacement [m] time-history for magnified Northridge input motion; (a) SF = 1.0; (b) SF = 2.0; (c) SF = 4.0; (d) SF = 6.0

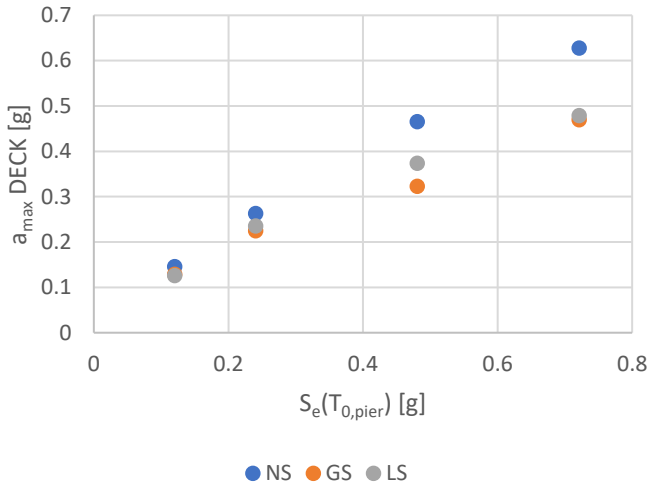

Figure 82. a_{max} at the caisson and at the deck vs $S_e(T_{0,pier})$ for magnified Northridge input motion; (a) SF = 1.0; (b) SF = 2.0; (c) SF = 4.0; (d) SF = 6.0

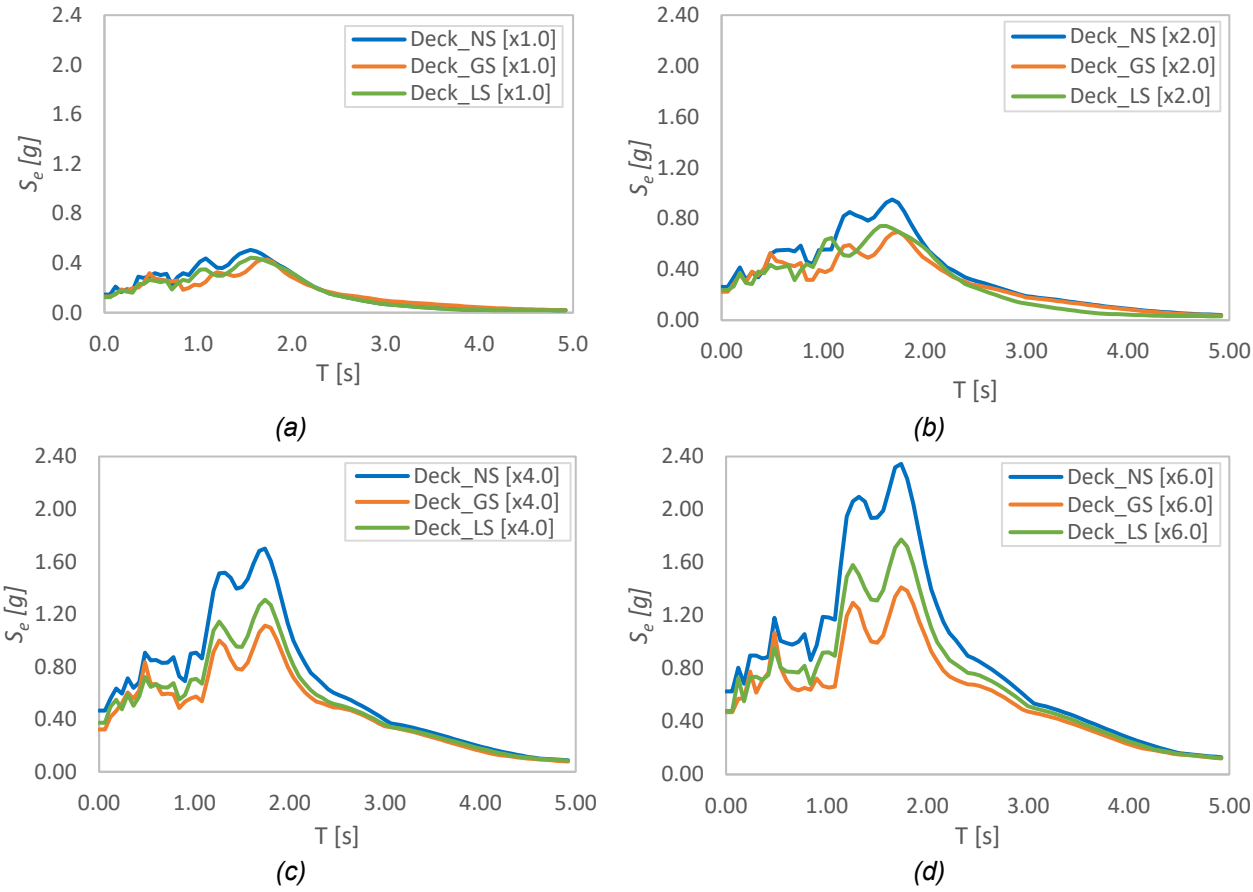

Figure 83. Response spectrums at the deck for magnified Northridge input motion; (a) SF = 1.0; (b) SF = 2.0; (c) SF = 4.0; (d) SF = 6.0

It is important to highlight that a SF greater than 6.0 was required to induce structural failure. This suggests an overdesign of the studied caisson foundation from a geotechnical point of view. Notably, an SF of 8.0 was necessary for failure in the LS case, while the NS and GS cases did not fail, although convergence issues, likely due to extensive strains within the soil, were observed in the NS model by the end of the shaking (*Figure 84*). Moreover, the failure in the LS case occurred as the deck and caisson rotated towards the most scoured direction. This discovery underscores that while scouring may reduce seismic actions—an effect more pronounced in a general scoured scenario—it could yield either beneficial or detrimental effects in a local scoured scenario.

However, the no failure of the foundation does not mean the superstructure remains operative after the conclusion of the shaking. A collapse of the deck and or failure of the pier can happen due to the high displacements recorded or also issues due to residual displacements/rotations may need replacement of bearings (*Figure 84*).

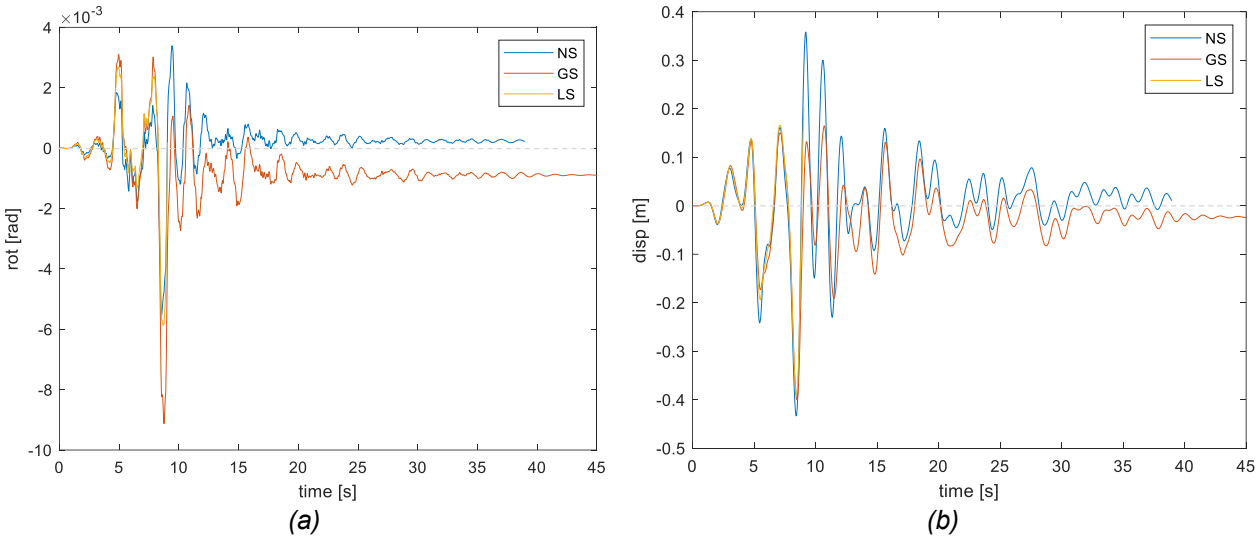

Figure 84. Caisson rotation [rad] (a) and Deck horizontal displacement [m] (b) time-histories for magnified Northridge input motion using an SF=8.0

CHAPTER EIGHT

CHAPTER 9

CONCLUSIONS

Caisson foundations play a pivotal role in supporting long-span bridges. With the increasing frequency and intensity of flood events driven by climate change, it becomes imperative to assess the impact of flood-induced scouring on the seismic behavior of soil-caisson-pier systems. This evaluation is critical for determining the necessity of retrofit measures to safeguard structures against potential damage or collapse during subsequent seismic events.

This study dealt with the intricate interplay between bridge pier caissons, scouring processes, and seismic forces through advanced numerical modeling (specifically Finite Element Method - FEM). The investigation focused on a specific case study, under drained conditions, encompassing three distinct scouring scenarios: No Scoured (NS), General Scoured (GS), and Local Scoured (LS). The findings corroborate previous research by highlighting the distinctly different effects of local and general scouring on the seismic behavior of structures, manifesting in terms of deformation, spectral acceleration, and cumulative displacements.

To comprehensively evaluate the response of the soil-caisson-pier system, it was conducted lateral pushover analyses and free vibration studies were conducted. These analyses unveiled the substantial impact of scouring conditions on the horizontal stiffness and the fundamental period of the system.

Notably, the NS and GS cases exhibited a symmetrical response, while the LS case displayed an asymmetric behavior. This trend aligns with the findings of other researchers, who have noted that the fundamental period of soil-foundation-pier systems tends to increase with scour depth, detrimentally affecting lateral stiffness.

These preliminary analyses provided a basis foundation for comprehending the system's dynamic response during transient analyses using input motions. They revealed higher cumulative displacements in the scoured cases, along with a noticeable trend in the LS case of the deck and caisson moving and rotating, respectively, in the most scoured direction. This behavior is primarily attributed to plastic strains in the compliant soil and the accumulation of displacements, which are notably higher in the scoured scenarios.

The above was verified during the seismic shaking. Moreover, although the NS case showed higher displacements at the deck at the beginning of the input motion, the permanent accumulated displacements for the GS and LS cases were higher by the end of the motion, the latter exhibiting a significant rotation and displacement in the most scoured direction.

The accelerations experienced at the deck in the NS case were generally higher than those in the GS and LS cases, particularly pronounced under strong ground motion. This trend is consistent with the widely documented isolation effect of scouring, which is prominently highlighted in this study. Furthermore, it's worth noting that the asymmetrical behavior in the LS

cases significantly influences the maximum acceleration experienced at the deck, depending on the directionality of the motion.

It is interesting to note that the lower deck acceleration observed in scoured cases, seem to suggest that structures supported on non-scoured foundations face a heightened risk of structural failure due to amplified seismic forces. However, the higher cumulative displacements and rotations observed in scoured scenarios may notably compromise structural serviceability. This paradox highlights a dichotomy: while scouring may avert immediate failure, it significantly impacts serviceability under seismic loads. On the other hand, non-scoured foundations pose apparently a greater risk of structural failure but potentially have a lesser impact on serviceability. As a consequence, it appears to be of primary importance to study the actual scouring scenario in terms of shape and depth of the scour hole as it is not possible to a priori define the most critical configuration.

Settlement accumulation during dynamic seismic loading seems primarily driven by soil densification, particularly in the initial phases of movement. Nevertheless, the GS case exhibited higher settlements, attributed to the lower overburden pressure within the compliant soil, which, in the case of embedded foundations, directly impacts bearing capacity.

The intricate interplay of various factors, including scouring conditions, ground motion characteristics, and soil behavior, results in complex and occasionally counterintuitive effects on the seismic response of piers supported by caisson foundations. This underscores the need for a comprehensive approach in the design and assessment of bridge pier caisson-soil systems. It is essential to continue research in this area, particularly under both non-scoured and scoured conditions, using a wider range of scour morphologies and an increased number of input motions varying in intensity and frequency content. This ongoing study will contribute to the development of more robust engineering practices and design considerations for critical infrastructure.

BIBLIOGRAPHY

Aimar, M. (2018). *STOCHASTIC ANALYSIS OF SEISMIC GROUND RESPONSE FOR VERIFICATION OF STANDARD SIMPLIFIED APPROACHES*. Polytechnic University of Turin.

Alampalli, S., & Ettouney, M. (2008a). *Multihazard applications in bridge management. Paper presented at the 10th International Conference on Bridge and Structure Management*. Transportation Research Board. https://doi.org/10.17226/17628

Alampalli, S., & Ettouney, M. (2008b, October 20). Multihazard applications in bridge management. *Paper Presented at the Tenth International Conference on Bridge and Structure Management*.

Anastasopoulos, I., Kourkoulis, R., Gelagoti, F., & Papadopoulos, E. (2012). Rocking response of SDOF systems on shallow improved sand: An experimental study. *Soil Dynamics and Earthquake Engineering*, *40*, 15–33. https://doi.org/10.1016/j.soildyn.2012.04.006

Andersen, L. (2004). *Elastodynamics and finite element analysis in wave propagation problems. Course notes*. Department of Civil Engineering. Aalborg University.

Andersson, L. (2021). *REDUCED ORDER MODELING IN STRUCTURAL DYNAMICS Consideration of local nonlinearities*. Lund University.

Arduino, P. (2023). *Geotechnical Elements and Models in Soil-Structure Interaction in OpenSees*. University of Washington .

Assimaki, D. (1998). *Static and Dynamic Analysis of Caissons Subjected to Lateral and Static Loading* [Diploma Thesis]. National Technical University of Athens.

Brancaleoni, F., Diana, G., Faccioli, E., Fiammenghi, G., Firth, I. P. T., Gimsing, N. J., Jamiolkowski, M., Sluszka, P., Solari, G., Valensise, G., & Vullo, E. (2010). *The Messina Strait Bridge. A challenge and a dream*. CRC Press.

Callisto, L. (2020). *MARTA - equivalent linear site response analysis of layered soil deposits* (v. 1.2.3). La Sapienza University of Rome. https://sites.google.com/a/uniroma1.it/luigicallisto/

Chang, K.-C., Sung, Y.-C., Liu, K.-Y., Wang, P.-H., Lee, Z.-K., Lee, L.-S., & Witarto. (2014). Seismic performance of an existing bridge with scoured caisson foundation. *Earthquake Engineering and Engineering Vibration*, *13*(S1), 151–165. https://doi.org/10.1007/s11803-014-0245-x

Charney, F. A., & Asce, F. (n.d.). *Unintended Consequences of Modeling Damping in Structures*. https://doi.org/10.1061/ASCE0733-94452008134:4581

Chatzigiannelis, I. (1999). *Lateral Static and Dynamic Analysis of Caissons in Non Homogeneous-Halfspace*. National Technical University of Athens.

Chen, W. F., & Mizuno, E. (1990). *Nonlinear analysis in soil mechanics, theory and implementation*. Elsevier.

BIBLIOGRAPHY

Chiew, Y. (1992). Scour Protection at Bridge Piers. *Journal of Hydraulic Engineering*, *118*(9), 1260–1269. https://doi.org/10.1061/(ASCE)0733-9429(1992)118:9(1260)

Chopra, A. K. (2005). *Dynamics of Structures: Theory and Applications to Earthquake Engineering*. Pearson Education.

Chopra, A. K. (2007). *Dynamics of Structures* (Third Edition). Pearson Prentice Hall.

Chortis, G., Askarinejad, A., Prendergast, L. J., Li, Q., & Gavin, K. (2020). Influence of scour depth and type on p–y curves for monopiles in sand under monotonic lateral loading in a geotechnical centrifuge. *Ocean Engineering*, *197*, 106838. https://doi.org/10.1016/j.oceaneng.2019.106838

Ciancimino, A. (2021). *Performance of caisson foundations subjected to flood-induced scour*. Polytechnic University of Turin .

Ciancimino, A., Anastasopoulos, I., Foti, S., & Gajo, A. (2022). Numerical modelling of the effects of foundation scour on the response of a bridge pier. *Acta Geotechnica*, *17*(9), 3697–3717. https://doi.org/10.1007/s11440-022-01591-9

Ciancimino, A., Jones, L., Sakellariadis, L., Anastasopoulos, I., & Foti, S. (2022). Experimental assessment of the performance of a bridge pier subjected to flood-induced foundation scour. *Géotechnique*, *72*(11), 998–1015. https://doi.org/10.1680/jgeot.20.P.230

Conti, R., & Di Laora, R. (2022). Substructure Method Revisited for Analyzing the Dynamic Interaction of Structures with Embedded Massive Foundations. *Journal of Geotechnical and Geoenvironmental Engineering*, *148*(6). https://doi.org/10.1061/(ASCE)GT.1943-5606.0002787

Crova, R., Jamiolkowski, M., Lancellotta, R., & Lo Presti, D. C. F. (1993). Geotechnical characterization of gravelly soils at Messina site. *Predictive Soil Mechanics (Proc., Wroth Memorial Symp.)*, 199–218.

Dassault Sysèmes. (2023). *ABAQUS FINITE ELEMENT ANALYSIS FOR MECHANICAL ENGINEERING AND CIVIL ENGINEERING*.

de Klerk, D., Rixen, D. J., & Voormeeren, S. N. (2008). General Framework for Dynamic Substructuring: History, Review and Classification of Techniques. *AIAA Journal*, *46*(5), 1169–1181. https://doi.org/10.2514/1.33274

Domenico, G. (2021). *Soil-structure interaction for the seismic design of integral abutment bridges: from advance numerical modelling to simplified procedures*. SAPIENZA University of Rome.

Duncan, J. M., & Chang, C.-Y. (1970). Nonlinear Analysis of Stress and Strain in Soils. *Journal of the Soil Mechanics and Foundations Division*, *96*(5), 1629–1653. https://doi.org/10.1061/JSFEAQ.0001458

El Hoseny, M., Ma, J., Dawoud, W., & Forcellini, D. (2023). The role of soil structure interaction (SSI) on seismic response of tall buildings with variable embedded depths by experimental and numerical approaches. *Soil Dynamics and Earthquake Engineering*, *164*, 107583. https://doi.org/10.1016/j.soildyn.2022.107583

BIBLIOGRAPHY

FEMA. (2000). *Prestandard and Commentary for the Seismic Rehabilitation of Buildings* (Vol. 356). Federal Emergency Management Agency.

Fioravante, V., Giretti, D., Jamiolkowski, M., & Rocchi, G. F. (2012). Triaxial tests on undisturbed samples of gravelly soils from the Sicilian shore of Messina strait. *Bulletin of Earthquake Engineering*, *10*, 1717–1744.

Foti, S., & Sabia, D. (2011). Influence of Foundation Scour on the Dynamic Response of an Existing Bridge. *Journal of Bridge Engineering*, *16*(2), 295–304. https://doi.org/10.1061/(ASCE)BE.1943-5592.0000146

Gaudio, D., & Rampello, S. (2016). Dynamic Soil-structure Interaction of Bridge-pier Caisson Foundations. *Procedia Engineering*, *158*, 146–151. https://doi.org/10.1016/j.proeng.2016.08.420

Gaudio, D., & Rampello, S. (2019). The influence of soil plasticity on the seismic performance of bridge piers on caisson foundations. *Soil Dynamics and Earthquake Engineering*, *118*, 120–133. https://doi.org/10.1016/j.soildyn.2018.12.007

Gaudio, D., & Rampello, S. (2020). Equivalent seismic coefficients for caisson foundations supporting bridge piers. *Soil Dynamics and Earthquake Engineering*, *129*, 105955. https://doi.org/10.1016/j.soildyn.2019.105955

Gaudio, D., & Rampello, S. (2021). On the assessment of seismic performance of bridge piers on caisson foundations subjected to strong ground motions. *Earthquake Engineering & Structural Dynamics*, *50*(5), 1429–1450. https://doi.org/10.1002/eqe.3407

Gazetas, G. (1991a). Formulas and Charts for Impedances of Surface and Embedded Foundations. *Journal of Geotechnical Engineering*, *117*(9), 1363–1381. https://doi.org/10.1061/(ASCE)0733-9410(1991)117:9(1363)

Gazetas, G. (1991b). Foundation Vibrations. In *Foundation Engineering Handbook* (2nd ed., pp. 553–593). Van Nostrand Reinhold.

Gazetas, G., & Tassoulas, J. L. (1987a). Horizontal Damping of Arbitrarily Shaped Embedded Foundations. *Journal of Geotechnical Engineering*, *113*(5), 458–475. https://doi.org/10.1061/(ASCE)0733-9410(1987)113:5(458)

Gazetas, G., & Tassoulas, J. L. (1987b). Horizontal Stiffness of Arbitrarily Shaped Embedded Foundations. *Journal of Geotechnical Engineering*, *113*(5), 440–457. https://doi.org/10.1061/(ASCE)0733-9410(1987)113:5(440)

Gerolymos, N., & Gazetas, G. (2006). Winkler model for lateral response of rigid caisson foundations in linear soil. *Soil Dynamics and Earthquake Engineering*, *26*(5), 347–361. https://doi.org/10.1016/j.soildyn.2005.12.003

González, F., Padrón, L. A., Carbonari, S., Morici, M., Aznárez, J. J., Dezi, F., & Leoni, G. (2019). Seismic response of bridge piers on pile groups for different soil damping models and lumped parameter representations of the foundation. *Earthquake Engineering & Structural Dynamics*, *48*(3), 306–327. https://doi.org/10.1002/eqe.3137

BIBLIOGRAPHY

Gorini, D. (2017). *Soil-structure interaction for bridge abutments: two complementary macro-elements*.

Gorini, D., & Callisto, L. (2019). Seismic performance and design approach for friction dissipative foundations. *Soil Dynamics and Earthquake Engineering*, *123*, 513–519. https://doi.org/10.1016/j.soildyn.2019.05.006

Gorini, D. N., Callisto, L., Franchin, P., & Fierro, T. (2021). *Soil-structure interaction in OpenSees strategies, applications and perspectives*.

Ishihara, K., Tatsuoka, F., & Yasuda, S. (1975). Undrained Deformation and Liquefaction of Sand Under Cyclic Stresses. *Soils and Foundations*, *15*(1), 29–44. https://doi.org/10.3208/sandf1972.15.29

Jamiolkowski, M., & Lo Presti, D. C. F. (2002). Geotechnical characterization of Holocene and Pleistocene Messina sand and gravel deposits. *Charact. and Engng. Properties of Natural Soils*, *2*, 1087–11120.

Jeremić, B., Jie, G., Preisig, M., & Tafazzoli, N. (2009). Time domain simulation of soil–foundation–structure interaction in non-uniform soils. *Earthquake Engineering & Structural Dynamics*, *38*(5), 699–718. https://doi.org/10.1002/eqe.896

Joyner, W. B., & Chen, A. T. F. (1975). Calculation of nonlinear ground response in earthquakes. *Bulletin of the Seismological Society of America*, *65*(5), 1315–1336.

Kamath, P., & Jiang, L. (2015). *A beginner's Guide to Development in OpenSees*.

Kausel, E. (2010). Early history of soil–structure interaction. *Soil Dynamics and Earthquake Engineering*, *30*(9), 822–832. https://doi.org/10.1016/j.soildyn.2009.11.001

Klinga, J. V., & Alipour, A. (2015). Assessment of structural integrity of bridges under extreme scour conditions. *Engineering Structures*, *82*, 55–71. https://doi.org/10.1016/j.engstruct.2014.07.021

Kondner, R. L. (1963). Hyperbolic stress-strain responses: Cohesive soils. *Journal of the Soil Mechanics and Foundations Division*, *89*(1), 115–143.

Kotronis, P., Tamagnini, C., & Grange, S. (2013). *ALERT Doctoral School 2013 - Soil-Structure Interaction*. The Alliance of Laboratories in Europe for Research and Technology.

Kottke, A. R., & Rathje, E. M. (2009). *Technical Manual for Strata*. Pacific Earthquake Engineering Research Center (PEER).

Kramer, S. L. (1996). *Geotechnical Earthquake Engineering*. Prentice Hall.

Lesgidis, N., Kwon, O., & Sextos, A. (2015). A time-domain seismic SSI analysis method for inelastic bridge structures through the use of a frequency-dependent lumped parameter model. *Earthquake Engineering & Structural Dynamics*, *44*(13), 2137–2156. https://doi.org/10.1002/eqe.2573

Lesgidis, N., Sextos, A., & Kwon, O. (2018). A frequency-dependent and intensity-dependent macroelement for reduced order seismic analysis of soil-structure interacting systems.

Earthquake Engineering & Structural Dynamics, *47*(11), 2172–2194. https://doi.org/10.1002/eqe.3063

LeVeque, R. J. (2007). *Finite Difference Methods for Ordinary and Partial Differential Equations*. Society for Industrial and Applied Mathematics.

Li, X.-S., Dafalias, Y. F., & Wang, Z.-L. (1999). *State-dependent dilatancy in critical-state constitutive modelling of sand*.

Lin, S.-S., Hsu, S. Y., Liao, J. C., & Lin, J. G. (2012). Effects of Scouring on Performance of Caisson Foundation. *GeoCongress 2012*, 693–700. https://doi.org/10.1061/9780784412121.072

Lou, M., Wang, H., Chen, X., & Zhai, Y. (2011). Structure–soil–structure interaction: Literature review. *Soil Dynamics and Earthquake Engineering*, *31*(12), 1724–1731. https://doi.org/10.1016/j.soildyn.2011.07.008

Lysmer, J. (1978). Analytical procedures in soil dynamics. In *Report No. UCB/EERC-78/29*. Earthquake Engineering Research Center - University of California at Berkeley.

Lysmer, J., & Kuhlemeyer, R. L. (1969). Finite Dynamic Model for Infinite Media. *Journal of the Engineering Mechanics Division*, *95*(4), 859–877. https://doi.org/10.1061/JMCEA3.0001144

MathWorks. (2023). *MATLAB*. Cleve Moler.

Mazzoni, S., McKenna, F., Fenves, G. L., & PEER. (2010). *GettingStarted Manual (OpenSees)*. https://opensees.berkeley.edu/wiki/index.php/Getting_Started

Mazzoni, S., Mckenna, F., Scott, M. H., & Fenves, G. L. (2006). *OpenSees Command Language Manual*.

McGann, C., & Arduino, P. (2011, March 24). *Site Response Analysis of a Layered Soil Column (Total Stress Analysis)*. University of Washington . https://opensees.berkeley.edu/wiki/index.php/Site_Response_Analysis_of_a_Layered_Soil_Column_(Total_Stress_Analysis)

McGann, C., Arduino, P., & Mackenzie-Helnwein, P. (2011). *SSPbrick Element*. University of Washington.

McGann, C. R., Arduino, P., & Mackenzie-Helnwein, P. (2012). Stabilized single-point 4-node quadrilateral element for dynamic analysis of fluid saturated porous media. *Acta Geotechnica*, *7*(4), 297–311. https://doi.org/10.1007/s11440-012-0168-5

McKenna, F. (1997). *Object-oriented finite element programming: Frameworks for analysis, algorithms and parallel computing* [University of California]. https://opensees.berkeley.edu/OpenSees/doc/fmkdiss.pdf

Mckenna, F., & Fenves, G. L. (2008). Using the OpenSees Interpreter on Parallel Computers. In *Program of the National Science Foundation under Award Number CMS*. http://opensees.berkeley.edu

BIBLIOGRAPHY

Mckenna, F., Scott, M. H., & Fenves, G. L. (2010). Nonlinear Finite-Element Analysis Software Architecture Using Object Composition. *Journal of Computing in Civil Engineering*, *24*(1), 95–107. https://doi.org/ournal of Computing in Civil Engineering

Mylonakis, G., Nikolaou, A., & Gazetas, G. (1997). Soil-pile-bridge seismic interaction : Kinematic and inertial effects. Part I: Soft soil. *Earthquake Engineering & Structural Dynamics*, *26*(3), 337–359. https://doi.org/10.1002/(SICI)1096-9845(199703)26:3<337::AID-EQE646>3.0.CO;2-D

Mylonakis, G., Nikolaou, S., & Gazetas, G. (2006). Footings under seismic loading: Analysis and design issues with emphasis on bridge foundations. *Soil Dynamics and Earthquake Engineering*, *26*(9), 824–853. https://doi.org/10.1016/j.soildyn.2005.12.005

Newmark, N. M. (1959). A Method of Computation for Structural Dynamics. *ASCE Journal of Engineering Mechanics Division*, *85*, 67–94.

Nova, R., & Montrasio, L. (1991). Settlements of shallow foundations on sand. *Géotechnique*, *41*(2), 243–256. https://doi.org/10.1680/geot.1991.41.2.243

Occelli, P. (2004). *Influence of pile scouring in the dynamic behaviour of bridges"Influenza dello scalzamento delle pile sul comporta mento dinamico dei ponti (in Italian)"* [M.S. thesis]. Politecnico di Torino.

Petrini, L., Maggi, C., Priestley, M. J. N., & Calvi, G. M. (2008). Experimental verification of viscous damping modeling for inelastic time history analyzes. *Journal of Earthquake Engineering*, *12*(SUPPL. 1), 125–145. https://doi.org/10.1080/13632460801925822

Prevost, J. H. (1985). *A simple plasticity theory for frictional cohesionless soils*.

Priestley, M. J. N., Seible, F., & Calvi, G. M. (1996). *Seismic design and retrofit of bridges*. John Wiley & Sons.

Qi, W. G., Gao, F. P., Randolph, M. F., & Lehane, B. M. (2016). Scour effects on *p–y* curves for shallowly embedded piles in sand. *Géotechnique*, *66*(8), 648–660. https://doi.org/10.1680/jgeot.15.P.157

Sextos, A. G., Pitilakis, K. D., & Kappos, A. J. (2003). Inelastic dynamic analysis of RC bridges accounting for spatial variability of ground motion, site effects and soil-structure interaction phenomena. Part 1: Methodology and analytical tools. *Earthquake Engineering & Structural Dynamics*, *32*(4), 607–627. https://doi.org/10.1002/eqe.241

Sieber, M., Klar, S., Vassiliou, M. F., & Anastasopoulos, I. (2020). Robustness of simplified analysis methods for rocking structures on compliant soil. *Earthquake Engineering & Structural Dynamics*, *49*(14), 1388–1405. https://doi.org/10.1002/eqe.3294

Tariq, M., Khan, A., & Khan, M. (2022). Experimental Study of Scour Hole Depth around Bridge Pile Using Efficient Cross-Section. *Applied Sciences*, *12*(10), 5205. https://doi.org/10.3390/app12105205

Tsigginos, C., Gerolymos, N., Assimaki, D., & Gazetas, G. (2008). Seismic response of bridge pier on rigid caisson foundation in soil stratum. *Earthquake Engineering and Engineering Vibration*, *7*(1), 33–43. https://doi.org/10.1007/s11803-008-0825-8

BIBLIOGRAPHY

Varun, V. (2010). *A non linear dynamic macroelement for soil structure interaction analyses of piles in liquefiable sites*. Georgia Tech.

Veletsos, A. (1977). Dynamics of Structure Foundation Systems. *Structural and Geotechnical Mechanics. N.M. Newmark Honoring Volume*, 333–361.

Verrucci, L., Pagliaroli, A., Lanzo, G., Di Buccio, F., Biasco, A. P., & Cucci, C. (2022). Damping formulations for finite difference linear dynamic analyses: Performance and practical recommendations. *Computers and Geotechnics*, *142*. https://doi.org/10.1016/j.compgeo.2021.104568

Wang, Z., Dueñas-Osorio, L., & Padgett, J. E. (2014a). Influence of scour effects on the seismic response of reinforced concrete bridges. *Engineering Structures*, *76*, 202–214. https://doi.org/10.1016/j.engstruct.2014.06.026

Wang, Z., Dueñas-Osorio, L., & Padgett, J. E. (2014b). Influence of scour effects on the seismic response of reinforced concrete bridges. *Engineering Structures*, *76*, 202–214. https://doi.org/10.1016/j.engstruct.2014.06.026

Wei, K., Qiu, F., & Qin, S. (2022). Experimental and numerical investigation into effect of skirted caisson on local scour around the large-scale bridge foundation. *Ocean Engineering*, *250*, 111052. https://doi.org/10.1016/j.oceaneng.2022.111052

Yang, Z., Elgamal, A., & Parra, E. (2003). Computational Model for Cyclic Mobility and Associated Shear Deformation. *Journal of Geotechnical and Geoenvironmental Engineering*, *129*(12), 1119–1127. https://doi.org/10.1061/(ASCE)1090-0241(2003)129:12(1119)

Yang, Z., Lu, J., & Elgamal, A. (2008). *OpenSees Soil Models and Solid-Fluid Fully Coupled Elements User's Manual 2008 ver 1.0*. http://cyclic.ucsd.edu/opensees

Yu, H.-S. (2007). *Plasticity & Geotechnics*.

Zafeirakos, A., & Gerolymos, N. (2013). On the seismic response of under-designed caisson foundations. *Bulletin of Earthquake Engineering*, *11*(5), 1337–1372. https://doi.org/10.1007/s10518-013-9465-0

Zafeirakos, A., & Gerolymos, N. (2014). Towards a seismic capacity design of caisson foundations supporting bridge piers. *Soil Dynamics and Earthquake Engineering*, *67*, 179–197. https://doi.org/10.1016/j.soildyn.2014.09.002

Zhu, M. (2023). *OpenSeesPy Documentation Release 3.5.1.3*.

Zhu, M., McKenna, F., & Scott, M. H. (2018). OpenSeesPy: Python library for the OpenSees finite element framework. *SoftwareX*, *7*, 6–11. https://doi.org/10.1016/j.softx.2017.10.009